Rijksuniversiteit Groningen

Master Thesis

Tracers of the outer Milky Way stellar halo

Author:
J.G.E. Straat

Supervisor:
Prof Dr E. Starkenburg
M. Bayer, MSc

Abstract

In this thesis, we aimed to learn more about stellar streams by looking at different tracers in the Halo. To achieve this, we used Blue Horizontal Branch stars, RR Lyraes and Red Giant Branch stars from Gaia, Pristine and Pan-STARRS1 to study the metallicity distribution and stellar ratios of the Sagittarius stream, Jhelum and GD-1. We developed a method to select these streams based on position and proper motion to avoid biasing towards a specific survey while selecting the streams.

Using these samples, we found that the metallicities in Sgr from the RGBs were well traced by the RRL metallicities. The distribution of the RRL was shifted down by 0.5 dex lower compared to the RGB metallicities. This is likely because RRLs are biased to metal-poor stars.

The relation between the stellar ratio and metallicity was researched for Jhelum, GD-1, and Sgr Leading and Trailing arm. We found the strongest correlation between stellar ratio and metallicity for RRL/BHB, with an average Pearson correlation coefficient of 0.87. The other stellar ratios, RGB/RRL and RGB/BHB, also had good correlations but were slightly worse due to the large uncertainties caused by lower numbers of statistics.

Contents

Chapter 1

Introduction

To understand the current state of the Milky Way and its history, it is important to map it properly. Over the past two decades, a lot of progress has been made in mapping the outer Milky Way stellar halo using bright stars for which reasonably accurate distance estimates can be made. A notable example of these stars in the old halo are blue horizontal branch stars, which serve as standard candles. Other important tracers of the old Galactic stellar halo include RR Lyrae variables, red giant stars and standard candles. Studies typically use the 3D spatial information of these tracers, and when available, full 6D phase space data, to investigate substructures like stellar streams in the Milky Way's halo. A substantial and expanding body of research has examined these substructures to deduce the properties of the progenitor systems that created them, contributing to our understanding of the growth of the Galactic halo.

However, limited published data compares the presence or absence of these tracers across different substructures in the Milky Way's halo. Such comparisons would be valuable as they could provide crucial insights into the stellar populations and possible ages of the progenitor systems of streams in the Halo. Such observations are informative because blue horizontal branch stars, RR Lyrae stars, and Red Giant Branch stars represent different phases of stellar evolution. Therefore, identifying the ratio between these types in a given substructure could help constrain which evolutionary phases the progenitor system's stars had reached by the time they were accreted into the Milky Way. Additionally, suppose these techniques can be further developed and calibrated inside the well-studied Galaxy, they can also be applied to external galaxies. This allows us to map their populations, where detailed spectroscopy for example is too costly. This thesis will explore how these tracers of the galactic stellar halo can be combined to address the questions outlined above. I aim to investigate the extent to which metallicity information for these tracers can be incorporated to create a more complete picture of the stellar populations in the progenitor systems of these streams.

1.1 The Milky Way

The Milky Way is our host galaxy. It is an intermediate-sized, barred spiral galaxy and part of the Local Group. In the Local Group, the Milky Way and Andromeda are the most massive galaxies and are accompanied by many dwarf galaxies. Andromeda and the Milky Way are on a collision course and predicted to merge in around 6 Gyr (Sparke & Gallagher, 2000). The Milky Way is also undergoing merging events with smaller structures, namely the Small and Large Magellanic Cloud (SMC and LMC, respectively) and the Sagittarius (Sgr) dwarf galaxy. These structures are being disrupted by tidal stripping.

The Milky Way provides a unique opportunity to observe the structure of a galaxy and how it interacts with other objects in extraordinary detail. We can divide the Galaxy into the Galactic Bulge, the thin disc, the thick disc and the halo (Figure 1.1).

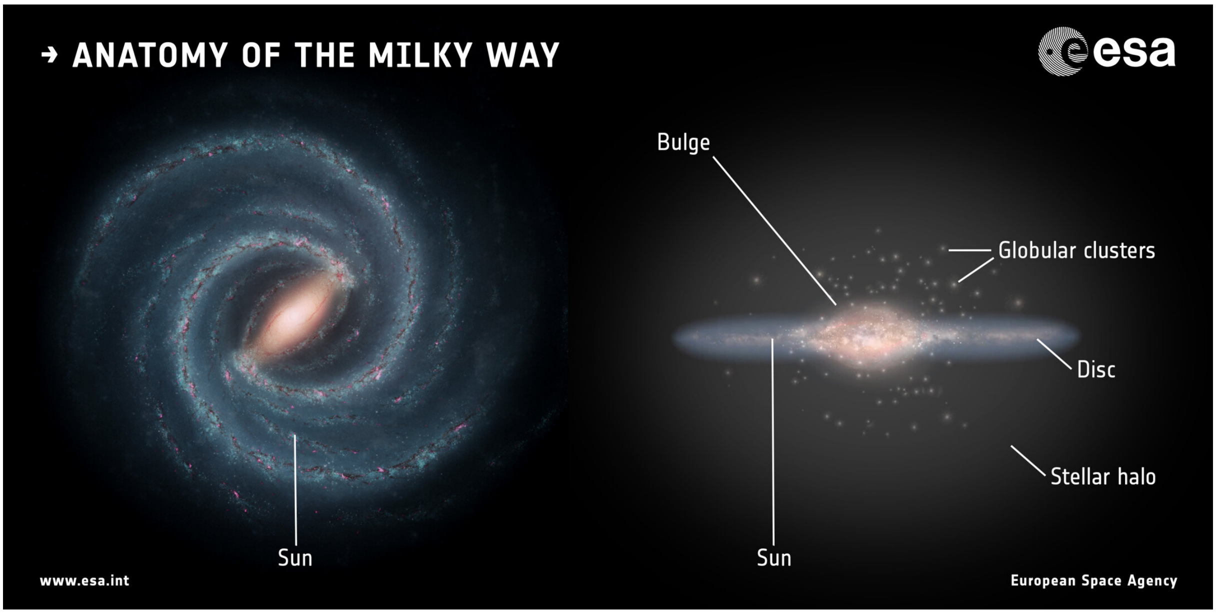

Figure 1.1: Credit: Left: NASA/JPL-Caltech; right: ESA; layout: ESA/ATG medialab

The bulge is one of the densest regions in the Galaxy and is mainly populated by older stars. Due to its crowdedness and high extinction, studying it has been hard. Nevertheless, we know that the bulge is shaped like a boxy peanut with a triaxial rotating bar in the centre. It mainly hosts old stars spanning a wide range of metallicities (Barbuy et al., 2018). The bar influences the dynamics of the inner Galaxy a lot, by introducing time-dependent effects on stellar orbits (Barbuy et al., 2018). The presence of the bar also makes our models for the MW a bit more complicated, as an axisymmetric galaxy is not a realistic assumption any more. It is hypothesised that the bar formed through disk instabilities, however, the influence of mergers and the exact mechanism governing the bar are still debated (Athanassoula, 2002).

Then there is the stellar disc, which can be split into the thin and thick disc (Bland-Hawthorn & Gerhard, 2016). The thin disc contains 95% of the disc stars and has ongoing star formation, with a star formation rate around $1.5 M_{\odot}/yr^{-1}$ (Sparke & Gallagher, 2000; Licquia & Newman, 2015). Hence, this part of the MW has a young population of stars. It is also rotationally supported, and the stars move on roughly circular orbits (Helmi & White, 1999). The thick disc has an older population of stars and is hypothesised to have a different origin than the thin disk due to their differing chemical sequences (Fuhrmann, 2011). It has not been easy to differentiate between the two, but the stars considered to be part of the thick disc are chemically different from the stars in the thin disc (Bensby et al., 2014). Thick disc stars are [Fe/α] and [C/N] enriched and seem to follow different tracks in [Fe/H] vs. [Fe/α] space (Fuhrmann, 2011; Masseron & Gilmore, 2015). This could be a result of a shorter and more intense period of star formation for the thick disk (Haywood et al., 2018).

Lastly, there is the Halo, a very extended and diffuse part of the Galaxy. In this Halo, we can find structures such as streams and Globular Clusters. A more in-depth overview of the properties of the Halo will be given in Section 1.3.

People are trying to discover the components' formation channels and how to simulate their kinematics and chemistry. Although there is no perfect model yet, simulations have returned results that agree with observations. These simulations can be roughly divided into two main categories; constrained models that describe components of the MW and cosmological simulations that try to understand the history of these components in a cosmological framework. An example of the first type is the model published by Vasiliev et al. (2021) (hereafter referred to as V21), where they aim to model the Sagittarius stream in a fixed gravitational potential of the MW. Later, they also introduce a moving potential for the LMC. They put these potentials in a restricted N-body simulation, where they allow for dynamical friction. From these simulations, V21 explored a wider range of potential parameters using MCMC methods. High-likelihood parameters were put into a live N-body system that was computationally more expensive but returned a more realistic representation of the stream. This simulation was able to reproduce the proper motion, line of sight velocity and spatial distribution of Sgr quite well, and will also be used in this thesis (see Section 3.1).

Cosmological simulations on the other hand, such as Auriga (Grand et al., 2017), try to simulate the formation of galaxies through cosmic time as predicted by the currently accepted ΛCDM model. This means that galaxies form through the merging of smaller structures, where these small structures form first in the Universe, followed by the first stars, which in turn grow through accretion and merging events to the galaxies we see today. This theory is supported by structures found in the halo, such as Sgr, LMC and SMC, smaller streams like GD-1 and Jhelum and high redshift observations.

1.2 Galactic Archaeology

Galactic Archaeology tries to figure out how the Milky Way formed and evolved. This field is relatively new, with work starting around 1950 in which Roman's work showed a correlation between the chemistry of stars and kinematics was very influential. The discovery of the Sagittarius stream by Ibata et al. (1994) and streams near the Sun in Hipparcos by Helmi et al. (1999) was direct evidence for merger events in the Milky Way, and spurred the further development of the field.

Archaeology looks at the oldest artefacts to discover more about the culture and society in which they were made. Similarly, Galactic Archaeology looks at the oldest stars and structures in the Milky Way to learn more about its past. In doing this, the idea is used that stars retain a "memory" of the environment they were made in. So low-mass stars, which have a potential lifetime longer than the age of the Universe, essentially probe what the early Universe looked like, as some of these stars will have formed early and are still around.

One of the things we can learn from these low-mass stars is the chemical abundance of their formation environment. Stellar atmospheres save a record of their parent molecular cloud (de Zeeuw & Norris, 1999). This record is especially accurate if the stars have not evolved from the Main Sequence. A molecular cloud will have some chemical abundance pattern, that will be transferred to the stars that form in this cloud. Hence, a group of stars with similar chemical abundance patterns are more likely to have a common origin. These different abundance patterns are a result of various elements forming in distinct environments and on different timescales (McWilliam, 1997).

If you are interested in looking at old structures, metal-poor stars are the best stars to look at. At the beginning of the Universe, there was almost exclusively hydrogen and helium. Hence, the first stars were made of only these elements. These first stars then started producing heavier elements through fusion or when they went Supernova. These heavier elements are then released into their environment when these stars die. This process enriched the environment in which new stars were born. Naturally, these stars had a higher metallicity than the stars before them and enriched the environment when they died. Hence, every subsequent generation of stars became a bit more metal-rich. While this is true for a closed environment, it does not hold up for environments, like the MW, that interact with intergalactic clouds and galaxies in their vicinity. These interactions can also influence the metallicity, abundance ratios of different elements and star formation rate. Nevertheless, metal-poor stars allow for researching stars from older generations, formed when the Universe was younger.

Next to chemical abundances, stars also retain the dynamical properties of the structure they originate from. When a galaxy merges with another, the stars from this system will keep some of their initial movement and move along orbits similar to the one they followed in the progenitor system (Johnston, 1998; Helmi, 2020). When the stars are tidally stripped away from the progenitor system, they will form streams in the galaxy that they merged with. When the progenitor system is small or the merging event happened recently, it forms a long and narrow stream across the sky. However, if a galaxy merges with a bigger system, the stars will have a broader population of orbits, which results in a wider stream. Over time, these streams also phase-mix with the rest of the Galaxy. By researching these streams, it is possible to learn about the progenitor systems they came from and the merging history of the Milky Way. Streams that populate the inner halo get dispersed quicker than stars in the outer halo due to stronger tidal forces and shorter orbital timescales (Helmi & White, 1999). So streams in the outer halo help distinguish ancient merging events and peer even further back in the history of the Galaxy.

Lastly, one can also look at the ages of structures. This is often done by fitting model isochrones. Isochrones are influenced by many factors besides the age of a star, and will therefore not always give the most precise age estimate. Isochrone fitting is often an oversimplification when applied to more complex structures such as galaxies (Tolstoy et al., 2009). However, new ways are being developed to increase the reliability of the age estimates. One of those promising methods is astroseismology, which looks at the internal structure of a star to estimate its distance. This is done with a time series of high-quality photometry. Unfortunately, these measurements are only available for a limited number of nearby stars. It is important to have reliable ages on the stars, as they allow for creating a timeline of the events that shaped the streams and thus the Milky Way.

1.3 The Galactic Halo

Most streams can be found in the outermost region of the MW, called the Galactic Halo. This is the sparsest part of the MW, only containing about 1% of its stellar mass (Bland-Hawthorn & Gerhard, 2016). It is mainly composed of stars and Globular Clusters that appear to have no organised motion around the centre of the MW (Sparke & Gallagher, 2000). This lack of organised motion is a result of how the Halo was formed. The components mentioned in Section 1.1 are mainly composed of what we call in-situ stars (Naidu et al., 2020). This means that the stars are formed within the MW and generally adhere to the organised motion seen in these components. On the other hand, the Halo is mostly made of ex-situ, or accreted, stars. These stars can retain the kinematics of the progenitor system for some time due to the Halo's long dynamical timescales, which means it takes a long time before the accreted systems are fully disrupted (Bland-Hawthorn & Gerhard, 2016). These effects leave the Halo clumpy and full of structures, that we can more easily spot due to its sparsity.

The inner halo, as a galactic component, is older than the outer halo. The outer halo is freshly accreted, while the inner halo is a mixture of structures accreted a long time ago and disc stars kicked up due to merging events Bland-Hawthorn & Gerhard (2016); Li et al. (2022). The outer halo is also more metal-poor on average than the inner halo (Morrison et al., 2009; Bonaca et al., 2017; Li et al., 2022). As the structures in the inner halo have been accreted a longer time ago, they are also more disrupted and harder to find as there are more in-situ stars there.

Multiple surveys have been employed to help with this search. One of these surveys is the Sloan Digital Sky Survey (SDSS). SDSS is a photometric survey and has 5 broadband filters (u, g, r, i and z). Through these filters, it has been able to map a large portion of the sky. It helped to characterise substructures in the Halo, such as tidal tales of globular clusters and dwarf galaxies (Newberg, 2005).

Another survey that aims to map the substructures in the Halo is the Pristine Survey, which will be used for several of the samples used in this thesis. This is a narrowband photometric survey, centred around the $CaHK$ line, which is metallicity sensitive. This narrowband filter allows for accurate metallicity determination, even if the stars are further out in the MW. The best way to determine the metallicity of a star is obviously through spectroscopy. Unfortunately, that method does not allow for observing big patches in the sky and is better suited for individual follow-up rather than mapping stars. Pristine can get the $CaHK$ line for big patches in the sky because it uses photometry instead of spectroscopy. It focuses on high galactic latitudes and areas of the sky with many streams.

Unfortunately, these two surveys have only observed specific parts of the sky, and thus do not provide an all-sky picture of the Halo. This is one aspect where Gaia truly shines. Figure 1.2 shows the subset in the Gaia DR3 dataset. This all-sky astrometric survey aims to create the largest 3D map of the MW to date and collects the proper motions and parallaxes of over a billion stars. Additionally, it has three broadband filters: G (green), G_{BP} (blue), and G_{RP} (red). These parameters are good for nearby stars, but when you start looking at stars farther than 10 kpc and with G<18 mag, the uncertainties on the parallax become rather large. Gaia also returns an estimate for the metallicity, but only for very bright stars. This metallicity estimate is based on the Gaia XP spectra, available for 470 million stars. This instrument of Gaia takes low-resolution spectroscopic measurements of stars, most of which are brighter than 17.65 dex and are taken over the BP and RP colour ranges (Montegriffo et al., 2023). The XP spectra do not provide a very detailed image of the composition of the stars. However, the sheer number of stars for which these spectra are available is valuable for understanding the metallicity distribution of structures in the MW. It can also be used to derive other stellar parameters, for which a metallicity estimate is required.

These missions and surveys have greatly aided in the further discovery of the Halo and new streams. In the next sections, I will describe the stellar streams which will be treated in the rest of this thesis.

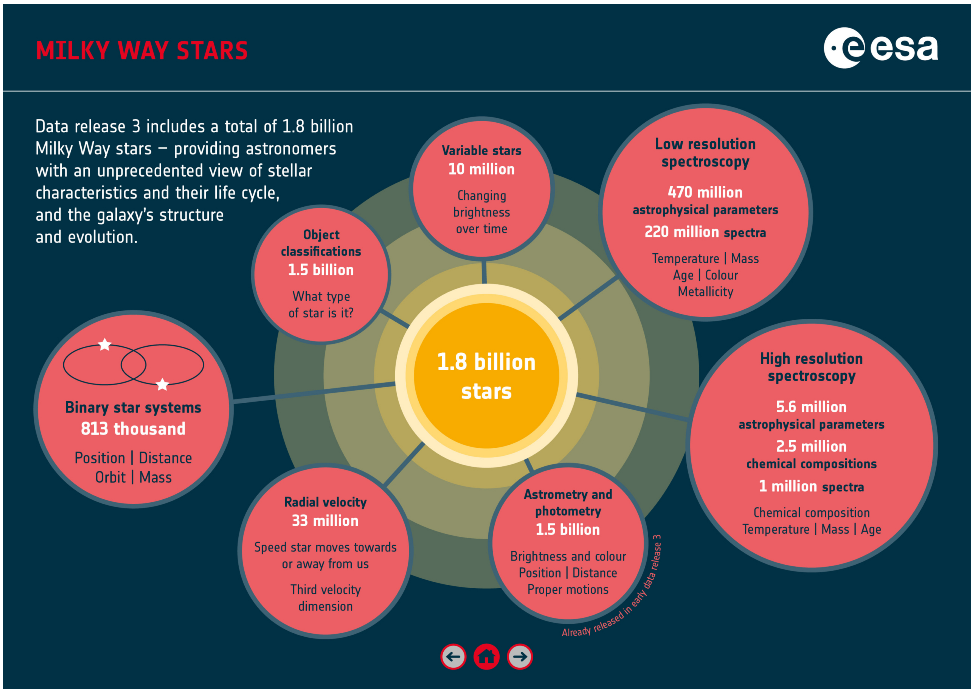

Figure 1.2: The image shows the subsets of data in Gaia DR3. Credit: ESA

1.3.1 Sagittarius Stream

The Sagittarius stream (Sgr) was discovered by Ibata et al. (1994) as a big co-moving group of stars and has since then been an invaluable structure in the MW halo to learn about the history and current structure of the MW. The progenitor system is thought to have had a baryonic mass of around $6 \times 10^8 M_\odot$ (Niederste-Ostholt et al., 2012), making it the largest semi-preserved structure in the halo (Cunningham et al., 2024). It is currently being disrupted by the MW and the LMC, leading to its most prominent features: the leading and the trailing arm (Vasiliev et al., 2021). These two arms meet at the remnant of the dwarf galaxy progenitor and have at least 3 radial turning points (see Figure 1.3), which indicates that it has been tidally interacting with the MW for a long time (Fardal et al., 2019). The arms are thought to have started to unravel around 6 Gyr ago and now have more than fully wrapped around the MW, extending in both the northern and southern hemispheres (Laporte et al., 2018).

The kinematics of the arms have been crucial in learning about the shape of the dark matter halo of the MW. The velocities in the arms favoured differently shaped halos. The velocities found in the leading arm would suggest a prolate halo, while the trailing arm indicated an oblate halo (Helmi, 2004; Johnston et al., 2005). These two theories were combined by Law & Majewski (2010), who suggested a slightly triaxial halo which was able to most accurately replicate the stream properties known at that time. More recent work by Vera-Ciro & Helmi (2013) prefers an oblate halo with $q_z = 0.9$ for $r \leq 10$ kpc, where they note the importance of taking the LMC into account when modelling the Sagittarius stream.

Another interesting feature of the Sgr stream is a primary bright track and a fainter track that is misaligned from the bright track (Law & Majewski, 2010; Vasiliev et al., 2021). This is referred to as the bifurcation of Sgr and is present in both the leading and trailing arm (Belokurov et al., 2006; Koposov et al., 2012; Ramos et al., 2022). The origin of this bifurcation is not completely clear yet. Possible explanations could be that it originates from different stripping epochs, where the faint track was stripped first and the bright track at a later time (Fellhauer et al., 2006).

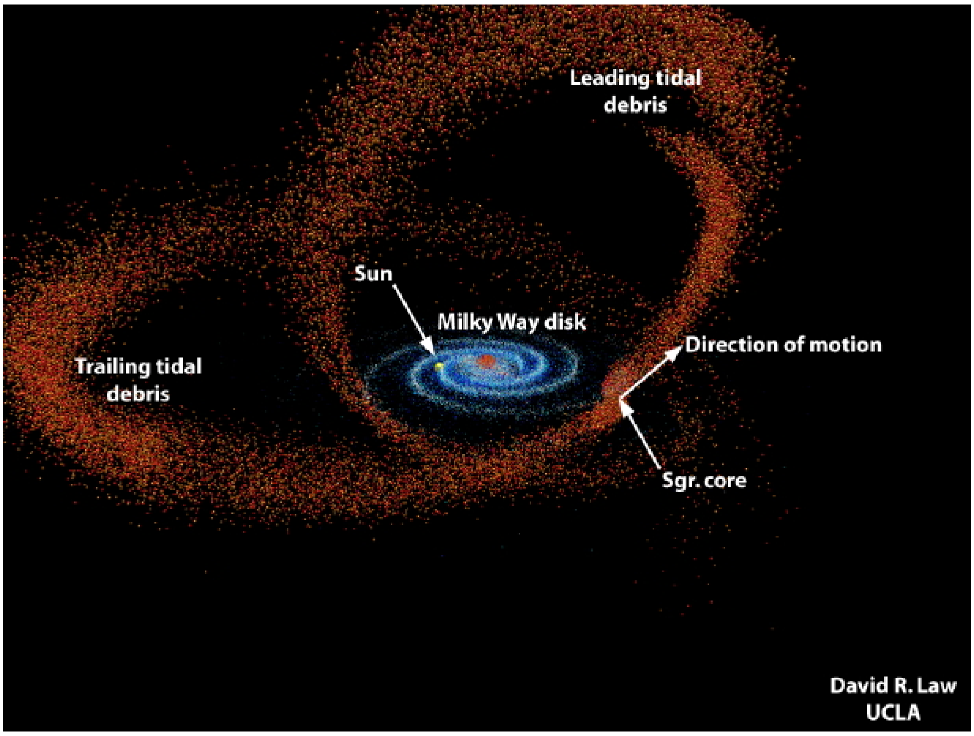

Figure 1.3: This image shows how the Sgr stream wraps around the Milky Way, illustrating the location of the core, leading and trailing arm. Credit: D. R. Law (UCLA)

Vasiliev et al. (2021) proposed an alternate explanation that the bifurcation could be due to a superposition of rotating and non-rotating components in the progenitor system.

The leading and trailing arms also display other differences. The kinematic differences can be largely attributed to the different parts of the progenitor system from which they were stripped. The leading arm is ahead of the Sgr core in its orbit and thus also slightly closer to the MW. This closer orbit results in a dynamically tighter structure with higher energy (Vasiliev et al., 2021). The trailing arm lags behind the Sgr core and is further away from the MW. This part is a bit more diffuse than the leading arm. As a result, the trailing arm has lower proper motions and energy (Vasiliev et al., 2021). The leading and trailing arms also show a discrepancy in metallicity, where the leading arm is found to be slightly more metal-poor than the trailing arm (Ramos et al., 2022; Limberg et al., 2023).

The Sgr stream remains an active research field due to its complexity, size and crucial role in understanding the formation and evolutions of the MW and the gravitational interaction that the MW has with its environment. Additionally, mapping the stellar populations in its arms allows us to reconstruct the original Sgr galaxy, and thus provides another well-studied dwarf galaxy to test theories of galaxy formation.

1.3.2 Jhelum

Jhelum is one of the several streams discovered by Shipp et al. (2018) using the Dark Energy Survey (DES) and has been followed up by Gaia and SDSS data. The stream is characterised by its relatively narrow and dense morphology, making it easily recognisable in surveys.

Shipp et al. (2018) identified two components in Jhelum, one narrow, dense component and a diffuse, broader component. These components could be spatially identified as well as in proper motion (Awad et al., 2024). The formation of these two components could be explained by interactions with subhalos, the LMC, or an antisymmetric potential of the MW, which could disperse stars of a narrow stream into broader structures (Bonaca et al., 2014; Ngan et al., 2016; Pearson et al., 2017). It has also been suggested by Woudenberg et al. (2023) that Jhelum could have been perturbed by the orbit of the Sgr stream.

There has been some dispute about the origin of Jhelum. People have argued that the progenitor should be either a dwarf galaxy or a globular cluster. Recent studies have favoured a dwarf galaxy as the progenitor (Ji et al., 2020; Bonaca et al., 2021; Li et al., 2022). However, a compelling case for a globular cluster progenitor has been made by Awad et al. (2024). She found that the narrow component has a relatively small velocity and metallicity dispersion of 4.84 km s^{-1} and 0.15 km s^{-1}, respectively, and a width of 28.13 pc. The broader component, on the other hand, had larger dispersions of 19.49 km s^{-1} and 0.34 km s^{-1}, and a width of 84.09 pc. The smaller dispersions in the narrow component would favour a globular cluster progenitor, whereas the larger dispersion in the broader component argues for a dwarf galaxy progenitor. Awad et al. (2024) reconciles this by suggesting that Jhelum is the result of the accretion of a dwarf galaxy with a globular cluster, explaining the broad and narrow part of the stream, respectively. A deeper medium/high-resolution follow-up with high-quality metallicities and radial velocities is needed to settle this argument.

1.3.3 GD-1

The stellar stream GD-1 was discovered by Grillmair & Dionatos (2006) using SDSS. This stream is quite exceptional as it is one of the longest and densest streams known, spanning 100° on the sky (Webb & Bovy, 2019). The stream is located at approximately 10 kpc away from Earth and is thought to originate from a globular cluster with a mass of $\sim 4 \times 10^4 M_\odot$ (Koposov et al., 2010; Shih et al., 2022). This theory is supported by its small velocity dispersion, metal-poor population, and because it is a dynamically cold structure (Bonaca et al., 2020).

GD-1 is very narrow and has a well-defined track across the sky, making it easier to model compared to other more diffuse streams (Malhan et al., 2019). Interestingly, GD-1 is not as simple as that. It has some prominent substructures, known as the spur, blob and gaps (Price-Whelan & Bonaca, 2018; Bonaca et al., 2020). These substructures are thought to be caused by interactions with other globular clusters or dark matter subhalos that were previously associated with Sgr (Bonaca et al., 2020). Thanks to GD-1's dense and narrow nature, defining its unperturbed initial configuration is relatively easy. From that point onwards, globular clusters, gravitational potentials and dark matter halos can be introduced to simulate GD-1's interaction with these structures and see how they affect the stream. The gaps in GD-1 could also be explained by dark matter subhalos, which would kick up stars in the stream, creating gaps and irregularities in an otherwise smooth structure (Bonaca et al., 2020). This makes GD-1 extremely useful to study the distribution of dark matter in the MW but also in globular clusters and other substructures.

1.4 Stellar Evolution

The Galactic Halo and the long-lived stars that inhabit this part of the galaxy are vital to understanding the Milky Way's formation history, as mentioned in Section 1.2. Low-mass stars have lifetimes longer than the age of the Universe and therefore keep an excellent record of the environment in which they were formed (de Zeeuw & Norris, 1999). Once these low-mass stars have exhausted the hydrogen in their core, the outward pressure fuelled by hydrogen fusion diminishes. Hence the star is not in hydrostatic equilibrium any more and gravity will cause the

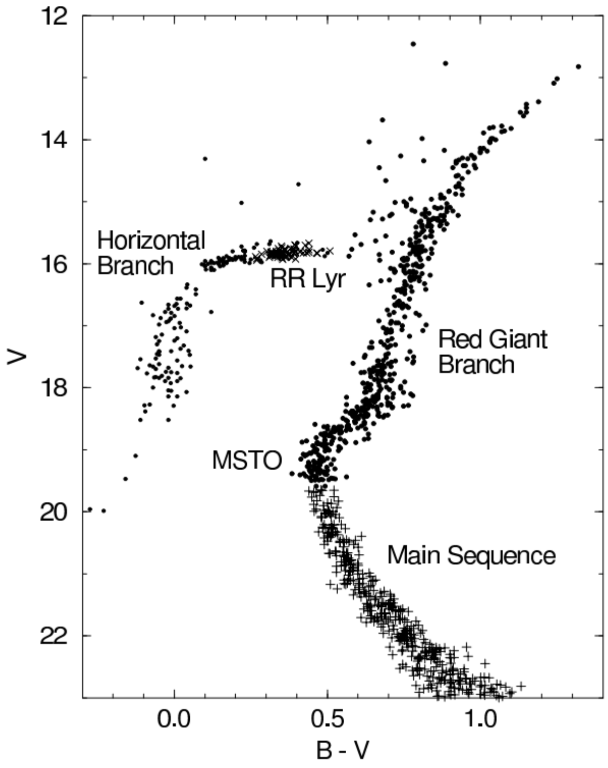

Figure 1.4: This is a Colour Magnitude Diagram displaying its key features. For this thesis, the Horizontal branch, populated by RRLs and BHBs, and the tip of the Red Giant Branch are of importance. Credit: Chaboyer (1996)

star to contract, increasing its gravitational potential energy. This energy heats the outer layers of the star's atmosphere, causing these layers to expand. This process increases the radius of the star. It lowers the opacity of the outer layers, allowing more photons to escape the star's surface and increasing its luminosity. The star leaves the MS due to its increased luminosity and moves onto the Red Giant Branch (RGB) (see Figure 1.4) (Salaris & Cassisi, 2005).

When the core hydrogen burning stops, the star starts shell hydrogen fusion. While on the RGB, the star keeps fusing hydrogen in its shell. The star is on the RGB when the hydrogen burning layer is around $0.001 M_\odot$. RGB stars are great for Galactic Archaeology as they are big, bright, and relatively numerous in the Halo, so they are visible out to great distances (Karttunen et al., 2007). Main Sequence stars are still more numerous, but in most cases too faint to observe in the Galactic Halo. RGB stars have effective temperatures ranging from 3300K to 5500K, and M_V between -0.3 and 0.9 mag. Stars spend less than 1 Gyr in this phase of their evolution, especially when the stars are metal-poor, as expected in the Halo. In the Halo we thus expect many stars in the later stages of the RGB, where they approach the characteristic luminosity $L_{\mathrm{He\ core}}$, making distance estimates more reliable there (Binney, 2021).

While the star burns the hydrogen in the shell, helium gets deposited in the core, making the helium core more dense. At some point, the core reaches a critical density where the core reaches a temperature $\sim 10^8$K and starts fusing helium. This event is referred to as the helium flash. After the helium flash, the star moves onto the Horizontal Branch.

During a star's evolution, it might cross the Instability Strip. In this Instability Strip, the star's gas is partially ionized and compressed by gravity. The energy of this compression goes into the reionization of the gas, which increases the opacity of the gas. The gas then absorbs more heat and pushes outward, decreasing the density and the opacity and releasing heat. Due to the decrease in density, the ions recombine, releasing more energy until the star compresses again. This brings it back to its starting state (Carroll & Ostlie, 2017). In most stars, this oscillation dampens out over time, and they become Blue Horizontal Branch stars (BHBs) or Red Clump stars (RCs). However, stars in the instability strip have the exact properties that maintain this oscillation, such as RR Lyrae stars (RRLs).

RRLs' pulsation periods are less than a day and the star itself is on average very bright ($L \sim 50L_\odot$), making them easily recognisable in observations (Sparke & Gallagher, 2000). These stars are old ($> 9 - 10$ Gyr), core-helium burning stars and can be divided into four categories based on the shape of their light curve (Clementini et al., 2023), which are further discussed in Section 1.4.1.

1.4.1 Pulsation modes of RR Lyrae

RRL can be divided into several categories based on their pulsation mode, referred to as RRab, RRc, RRd and RRe. RRab stars are RRLs whose light curve oscillates in the fundamental mode, RRc stars oscillate in the first overtone, RRd stars in a mixed mode where two modes are simultaneously excited, and RRe in only the second overtone (Soszynski et al., 2011; Demers & Wehlau, 1977).

Fiorentino et al. (2022) showed that the different pulsation modes of RRL could help trace the origin of the field and cluster RRLs. She further investigated Small Amplitude Short Period (SASP) and High Amplitude Short Period (HASP), which correspond to RRc and RRab stars, respectively, and found that HASPs could be indicative of progenitor systems with a fast early galaxy evolution and bigger merger events. SASPs can be considered to be HASPs' counterparts and are thus associated with minor mergers.

This theme also ties into the Oosterhoff dichotomy, which is a very active field of research. It was discovered by Oosterhoff (1939), who saw that RRab stars could be split into two groups based on their periods. Oosterhoff type I (OoI) stars have shorter average periods (0.55 days) and type II (OoII) have slightly longer periods (0.65 days). Between these periods, there is a gap where we barely find any RRLs. OoIs have been associated with more metal-rich environments and RRab stars, while OoIIs are associated with metal-poor environments and RRc stars (Van Albada & Baker, 1973; Bencivenni et al., 1991). If this were to be true, this would indicate that Oosterhoff's initial classification of the RRL pulsation mode was faulty. This could be possible as this discovery was made almost a century ago and the lightcurves were of lesser quality. This problem becomes increasingly more interesting when looking at different parts of the MW. Fabrizio et al. (2019) found no dichotomy in the field RRL and its presence in GCs to be due to a lack of intermediate-metal clusters with RRLs. But the third Gaia Data Release (Clementini et al., 2023) does display a separation between OoI and OoII, which makes the presence and origin of the Oosterhoff still an open problem (Li et al., 2024; Prudil & Arellano Ferro, 2024; Fabrizio et al., 2021). Luongo et al. (2024) notes that there is a strong link between the Oosterhoff dichotomy and the merging history of the MW.

From their light curves, it is possible to determine the pulsation period of the RRLs. The period-luminosity (PL) relations allow for the accurate derivation of the luminosity of RRL, from which reliable distances can be obtained. Zgirski et al. (2023) defined a PL-relation for the Near-Infrared with very little scatter. However, more PL relations have been described for other wavelength bands to make this distance determination applicable to surveys done in different wavelength regimes (Longmore et al., 1986; Narloch et al., 2024). Thanks to these PL relations, distances can be more accurately determined and improve the mapping of far-out structures in the Halo.

This, combined with their intrinsic high luminosity, makes RRLs invaluable for studying the Galactic Halo and uncovering the formation history of the Milky Way. RRLs have a typical absolute V-band magnitude of $M_V \sim 0.65$, and T_{eff} between $5600 - 7000$ K (Li et al., 2023).

RRLs are not the only type of star that populates the horizontal branch. The Blue Horizontal Branch stars (BHBs) are located in a bluer part of the horizontal branch. These hot, bright A-type stars have effective temperatures between 7500 K and 9000 K and are also often used as standard candles. This is because they inhabit an almost horizontal region in the Colour Magnitude Diagram (CMD) around $M_G \sim 0.5$ (Deason et al., 2011). BHBs are great tracers for the Galactic Halo, due to their reliable distances.

Unfortunately, in samples of BHBs, there is quite some contamination of Blue Stragglers (BSs), which are Main Sequence stars that have moved beyond the Main Sequence turn-off point (MSTO) (Carroll & Ostlie, 2017; Starkenburg et al., 2019). The most likely explanation for why BSs can move beyond the MSTO is because these stars are in a binary. This allows them to gain mass from the other star, prolonging their lifetime on the MS (LeBlanc, 2011). The BSs and BHBs have similar colours and temperatures and are therefore hard to distinguish in photometric surveys. It is vital to clean up the BHB sample, as BSs are intrinsically fainter than BHBs. So if you leave the sample as is, treat everything as BHBs, and try to determine the distances to these stars, the sample will appear to go much farther out and have many more stars in the Halo. This will give a faulty picture of the Halo or structure you are trying to observe.

One commonly used technique to clean up the BHB samples is to look at the Balmer lines. For BSs, the wings of the Balmer lines are much broader than for BHBs. This is because BHBs have a lower surface gravity than BSs. Due to the higher surface gravity, spectral lines are widened. The Balmer lines are sensitive to gravitational influences and therefore a great tool for distinguishing BHBs from BSs (Starkenburg et al., 2019). The main problem with this method is that fairly good spectroscopy is needed to see these differences, which gets even harder when going further out in the Halo. Therefore, a different method to distinguish these stars was proposed in Starkenburg et al. (2019), where they trace the Balmer jump, which is also gravity-sensitive. This to a BHB sample with purity and completeness of 93% and 91%, respectively. This method combines the $CaHK$ filter from the Pristine with u-band observations from SDSS. When plotting the BHBs and BSs in this space, they follow two different tracks, which have been defined as a polynomial of the SDSS magnitude of $g_0 - r_0$ by Deason et al. (2011). The distances from the star to the two tracks can then be calculated. Based on these distances, the probability of belonging to either of these tracks can be attributed to the star. In Starkenburg et al. (2019), they defined a BHB as having a probability of being a BHB higher than 0.8.

In this section, several evolutionary stages of low-mass stars in the outer Halo have been discussed. To study this structure, bright stars are needed that form in metal-poor environments and have a predictable absolute magnitude. RGB stars, RRLs, and BHBs lent themselves well to this purpose. These stars are invaluable in tracing the Halo and researching the progenitor systems that stellar streams in the Milky Way originated from.

In the next section, Colour-Magnitude Diagrams (CMDs) are discussed and how they can tell more about the system they depict. The main focus will be on the shape of the different components of the CMD and what these shapes tell us about the formation environments of RGB stars, RRLs, and BHBs.

1.5 Colour-Magnitude Diagrams

Colour-Magnitude Diagrams (CMDs) are invaluable tools in observational astronomy for learning about a structure's stellar population and evolutionary state. In these diagrams, the absolute or apparent magnitude of a star is plotted versus the dereddened difference between two colour bands. In the case of this thesis, those will be the blue and red passbands from Gaia, which will be referred to as BP and RP. Dereddening is a crucial step in this as, if not done properly, it can shift the stars plotted in the diagram too much, distorting the view of the stellar population. The reddening of the stars is caused by dust between the star and the observer, which mainly absorbs the blue light of a star and re-emits the star's light in the infrared, causing these stars to appear redder than they originally were. A precise map of the dust in the galaxy is needed to correct this. Efforts have been made by Schlegel et al. (1998), whose maps will be used in this thesis, on all the samples used. These dereddening maps were chosen because it is all-sky and give an integrated extinction suitable for halo targets.

As a star moves through its evolutionary stages, it also moves through the CMD. Several features of the CMD can be identified, such as

- The Main Sequence, where core hydrogen burning stars can be found. A star will spend the majority of its life on this feature,

- The Red Giant Branch (RGB), where the star has exhausted the hydrogen in its core and started burning hydrogen in its shell,

- The Horizontal Branch (HB), where we find core Helium burning stars. This part of the CMD has a nearly constant absolute magnitude, making it great for distance determination,

and many more. The comparison of these features, such as the RGB and the HB, reveals information about the observed stellar population. In this thesis, the focus will be on the RGB and HB as they are relatively bright, making them visible out to great distances, and tracing many properties of the stellar population.

The RGB appears on the CMD as a nearly vertical structure and can reveal a lot about the metallicity of the population. It is especially sensitive to metallicity, where a metal-rich population will lead to a redder RGB (Renzini & Fusi Pecci, 1988). Metal-richer stars have a higher opacity, making the outer layers cooler. These lower temperatures result in a redder colour. The RGB branch of metal-poorer populations tends to extend more vertically as well as can be seen in Figure 1.5.

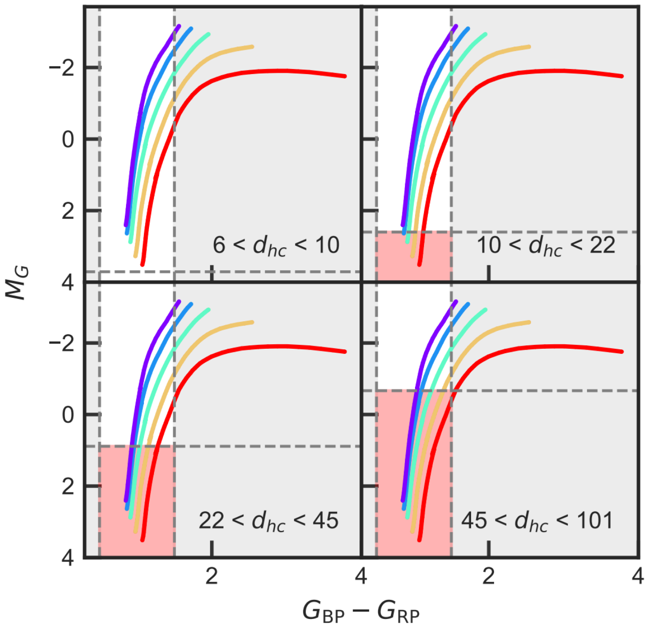

Figure 1.5: This figure is taken from Viswanathan, Byström, et al., 2024 and displays five PARSEC RGB isochrones with metallicities of -0.25, -0.75, -1.25, -1.75 and -2.25 dex going from red to purple. The grey areas are not in the RGB sample due to colour cuts done in this paper.

By comparing the position and length of the RGB structures, it is possible to infer which structure is metal-richer. The age of the stellar population also plays a big role in the population of the RGB. Typically, metal-richer populations with lower mass stars spend more time on the RGB, making the RGB more populated. Hence a stream that has relatively more RGB stars compared to younger stars such as MS or MSTO stars, will most likely be older and populated by lower mass stars (Sparke & Gallagher, 2000). Furthermore, the width of the RGB reveals the if the stars were formed at a similar point in time or over a longer period. If the stars were formed over a larger period, the RGB would be a superposition of isochrones of different ages. The narrowness is thus indicative of the period of star formation, with a broader RGB indicating a more continuous star-forming period (Keane et al., 1993; Binney, 2021)

In this thesis, we use two types of stars on the Horizontal Branch (HB): the RR Lyrae and Blue Horizontal Branch stars. Similarly to the RGB, the shape of the HB can reveal many qualities of the stellar population. The colour and extent of the HB are influenced by the mass loss while the star is on the RGB. If a star loses a lot of mass on the RGB, the hydrogen envelopes are slightly thinner, making the star appear bluer (Lee et al., 1994). However, the extent can also be influenced by the Helium abundance in stars, as a high abundance has been observed to correlate with a more extended HB (Piotto et al., 2007). Additionally, Catelan (2009), showed that an extended HB is also an indicator of the age of a stellar population. Older populations typically have lower mass stars on the HB, which translates into a more extended HB.

Unfortunately, the HB is a part of stellar evolution that is not fully understood yet, and many factors influence its shape and extent. These factors include rotation, extra mixing and pollution, age, and mass loss (Catelan, 2007). However, it is poorly understood which factors influence the stellar evolution of low-mass stars and how they precisely influence the HB. This open question is often referred to as the second parameter problem, although in the light of more recent studies, the second and third parameter problem would be a better name (Gratton et al., 2010). The first parameter is metallicity, but there is some dispute over the second and third parameters, with the most common suggestions being the age of the star and the mass loss when leaving the RGB (Catelan, 2009; Gratton et al., 2010). Even though it is widely agreed upon that the RGB mass loss controls the exact placement of a star on the HB, no solid theoretical explanation exists on how this exactly works (Belokurov et al., 2020). The effect of mass loss is often included in stellar evolution models by simple parameterizations (Schröder & Cuntz, 2005). However, this is incredibly difficult to test with observations, as the mass loss is not an observable parameter. It is also not entirely known how mass loss affects the HB, as there exists evidence arguing that there is minimal influence, as well as having more influence than metallicity (McDonald & Zijlstra, 2015; Heyl et al., 2015). This makes the evolution of low-mass stars an active research field with many open questions, that, when answered, can teach us more about the evolution of stellar populations and substructures.

These features can also be used together to infer the properties of the stellar population. Comparing the number of stars on the RGB and HB, $R = N_{HB}/N_{RGB}$, could help estimate the stellar populations' helium abundance and mass loss efficiency.

1.6 This Thesis

The structures further examined in this work will be the Sagittarius stream, Jhelum and GD-1. All of these are streams with different progenitor systems and are all disrupted. This makes it significantly harder to select them in a survey. So in that regard, it would be easier to look at structures that are still bound, such as intact dwarf galaxies and GCs. However, these bound and disrupted structures cannot be used interchangeably. Grimozzi et al. (2024) showed notable differences between the properties and origin of disrupted and surviving satellites. Disrupted satellites are found to have a lower metallicity than their bound counterparts at a similar mass (Naidu et al., 2022). But their chemical composition is also different. The disrupted satellites have a higher [Mg/Fe] at fixed metallicity, which corresponds strongly with the redshift at which these structures were accreted (Grimozzi et al., 2024). The simulations presented in Grimozzi et al. (2024) also showed that the disrupted dwarfs of the MW were typically formed and evolved in much denser environments than the intact satellites of the MW. Hence by researching streams instead of intact dwarf galaxies and GCs, we can research stellar populations we don't see in intact satellites.

Additionally, more and more streams are being found, and they are often a lot closer than the bound populations. So streams can give a more complete sample of their populations. These two factors combined make streams a very interesting avenue to explore the early Universe.

To research these streams, we are using BHBs, RRLs and RGB stars. These stars trace different populations and can be used together to obtain a more complete image of the stellar populations of the progenitor systems. These stars are also very bright, allowing us to trace further out structures in the Galaxy and beyond.

This thesis investigates the relation between the ratios of different stellar types and the metallicity, the metallicity distribution as traced by different stellar types and what the morphology of the Horizontal Branch and the Red Giant Branch can tell us about the evolutionary path of the progenitor systems. In doing so, we will try to be as quantitative in our comparisons as possible, to allow for comparisons in future work.

Chapter 2

Data Samples

In this thesis, we look at three types of stars: RGBs, RRLs, and BHBs to investigate what their colour and metallicity information can tell us about the stellar population of the progenitor system. To identify these stars, different procedures are needed for their characterization, which have different requirements of the survey that observes them. This led to multiple surveys being used to compose our samples. In the following section, we will discuss where the data comes from and why certain catalogues were chosen over others. Moreover, we have performed several tests on the samples to increase their purity and fine-tune them to fit the needs of this thesis better.

2.1 Red Giant Branch Stars

For the RGB stars in this sample, the RGB sample from Andrae et al. (2023) was initially used. They present a catalogue of 175 million stars with values for [M/H], T_{eff} and $\log g$ derived using the XGBoost algorithm for stars with XP spectra from Gaia DR3. Of this catalogue, a subset was used of 17 million bright Red Giants, with a limiting absolute G magnitude of 16 and constraining parallaxes. This subset was published as a separate table in the same paper by Andrae et al. (2023). The distance to the RGB stars is also necessary to compare the different types of stars, however, this was not given in the catalogue. The most reliable method for distance calculation is via the parallax. Unfortunately, the parallax becomes less reliable when looking at further out structures. Luckily, a method independent of parallax was developed by Viswanathan, Byström, et al., 2024 to calculate the distances to RGB stars. It uses an isochrone fitting method, which allows one to derive farther out distances and is used in this work. The code takes the BP-RP colour and metallicity and returns the absolute G magnitude. The catalogue also includes the apparent G magnitude, so we can use Equation 2.2 to obtain the distances.

2.1.1 Testing of the Sample

To determine the spread of distances using the isochrone method, a comparison was made with the results from the isochrone matching method using T_{eff} instead of $BP_0 - RP_0$. When plotting the distance obtained via $BP_0 - RP_0$ and T_{eff} versus each other, a large spread could be observed that increased with increasing distance. To get to the bottom of this behaviour, another comparison was made where the distances from BP_0 and T_{eff} were compared to the parallax, which can be approximated as $1/d$. Two parallax cuts were made, one of $\varpi/\delta\varpi > 5$ and one of $\varpi/\delta\varpi > 20$. The first quality cut is a bit less certain but allows us to trace further out stars in our comparison. When the parallax is multiplied by the distance, the product of the two should be equal to one, if the distance from the isochrone matching and the parallax perfectly agree. This method allows us to determine the spread in the T_{eff} and $BP_0 - RP_0$ methods.

This quantity was plotted versus the absolute G magnitude, $BP_0 - RP_0$ and T_{eff}, which can be seen in Figure 2.2. From the right panel of Figure 2.2, it becomes apparent that the spread in distances is less for the method using T_{eff}, as the root mean squared deviation (rmsd) is generally lower for T_{eff}. Therefore, the isochrone matching method with metallicity and T_{eff} will be used in the rest of this thesis. T_{eff} is also a more robust parameter, which results in a more reliable distance estimate. As T_{eff} comes out of the XGBoost algorithm, it is based on multiple observables, such as parallax, XP spectra and photometry, whereas $BP_0 - RP_0$ only depends on the BP and RP observations, and the quality of your de-reddening map. Hence, it also makes sense from a logical perspective to go with the more robust parameter and derive the distances with T_{eff}. The results of this testing were also adopted in Viswanathan, Byström, et al., 2024, where they are used for the scientific exploration of the Halo.

In Figure 2.2, we see the bimodality in the dataset as well. The left panel of Figure 2.2 clusters strongly around $G_0 \approx 0.5$. This magnitude would correspond to the Red Clump Giants(Ruiz-Dern et al., 2018). To more definitively conclude if these stars belong to the Red Clump, different metallicity bins were created and the histograms of those bins were plotted in Figure 2.1. Red Clump stars are a branch of metal-rich giants with a metallicity of [Fe/H] ≥ -1(Nataf et al., 2021). Hence, if the RCG causes this bimodality, it should only appear in the metallicity bin of $[Fe/H] \geq -1$.

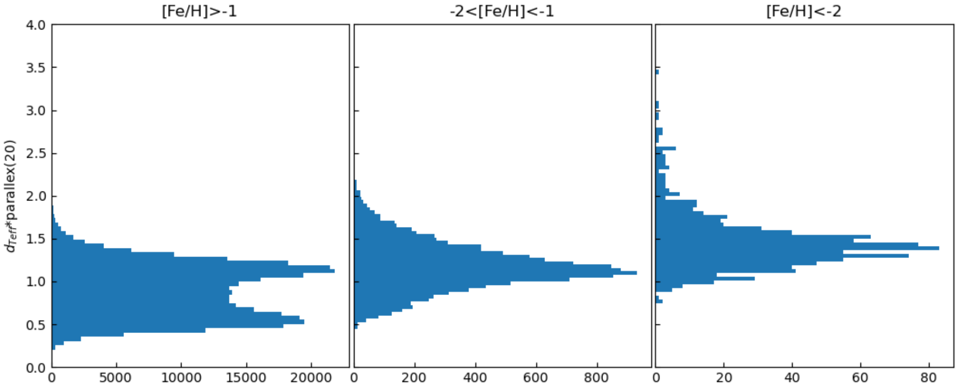

Figure 2.1: A histogram is plotted for the distance times the parallax for different metallicity ranges to check if Red Clump stars cause the bimodality. The distance selected for these plots is calculated using T_{eff}, as we will use this for the final distance calculation. The quality cut for parallax is $\varpi/\delta\varpi > 20$. As the bimodality shows up only for metallicities higher than -1, we can conclude that Red Clump stars probably cause this bimodality.

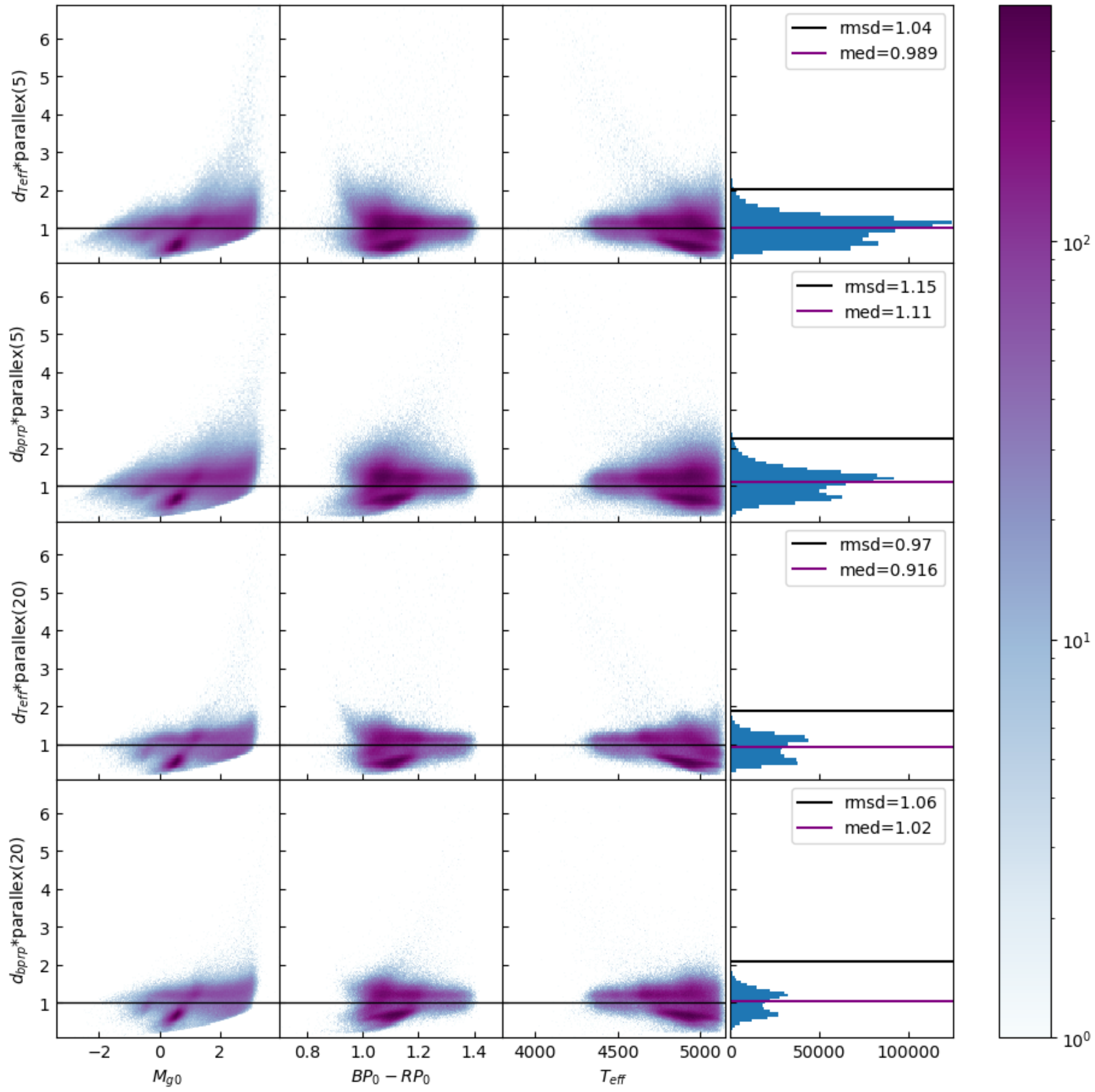

Figure 2.2: This figure displays the distances of the RGB sample as calculated with the isochrone matching method using T_{eff} and $BP_0 - RP_0$ for two quality cuts for the parallax. The y-axis displays the parallax multiplied by the distance, which should be one of the two quantities agreed. This quantity is plotted versus the absolute G magnitude, $BP_0 - RP_0$ and T_{eff}. The right-most plots are a histogram of the value plotted on the y-axis, which makes the bimodality even clearer.

This can indeed be seen in Figure 2.1, and we can thus conclude that the RCG causes this bimodality. As displayed in Figure 2.2, the distances to the RCG are systematically underestimated. This makes sense when considering the method used to derive the distances. The isochrones used do not include a Red Clump branch. Hence, any RCGs in our sample will be forced on the RGB isochrone, which shifts them downwards on the colour-magnitude diagram, resulting in a fainter absolute magnitude than what the stars have in reality. So the method will assign a lower distance to these stars.

When implementing this method on the sample by Andrae et al. (2023), the RGB stars only went out to approximately 20 kpc. As this sample does not go deep enough to probe the Sagittarius Stream, other samples from Viswanathan, Byström, et al., 2024 will be used. One sample extends to 100 kpc and is based on deep-PRISTINE data. This sample will be referred to as the VB1 sample and is limited to the Pristine footprint (see Figure 2.3). We also use the all-sky sample from Viswanathan, Byström, et al., 2024 (VB2) that uses Gaia and Pristine data, where they get the metallicity from Gaia XP spectra. Even though VB2 is all-sky it does not go as deep, only extending to a little under 70 kpc. Hence VB2 will only be used for comparisons to nearby structures. Furthermore, we implement a cut on $\log g$, taking only values smaller than 2.3. This cut ensures that we only select the tip of the RGB.

2.1.2 Conclusion on RGB sample

We will be using the deep-PRISTINE and PRISTINE-Gaia samples from Viswanathan, Byström, et al., 2024, VB1 and VB2 respectively, for the RGB samples. This first sample is limited to the PRISTINE footprint but allows for the study of further out structures, while VB2 is all sky and can only be used to study nearby structures. As a result of the analysis in Section 2.1.1, Viswanathan, Byström, et al., 2024 use T_{eff} instead of $BP_0 - RP_0$ to fit the isochrones and derive a distance to the RGB stars.

2.2 RR Lyrae Stars

The initial sample that was used for the RRLs was a sample produced by Sesar et al. (2017a). This sample uses the Pan-STARRS1 3π survey, hereafter referred to as PS1, and applies a machine learning algorithm to analyse the light curves of the stars to determine whether these stars were RRLs. The algorithm returned a classification score of a star being an RRab, RRc or RRd star together with the distance modulus. Hernitschek et al. (2017) used this sample to examine the Sagittarius stream and took all the stars with a probability of being an RRab, $S3_{ab}$, higher than 0.75 to be RRLs. This gave a sample of over 44,000 RRLs with a purity of 90% and completeness of 80% out to 80 kpc. The complete sample extends to 120 kpc, but after 80 kpc, the purity and completeness decrease slightly. The same selection is used in this work.

With this quality cut, we got a very pure and complete sample with reliable distances extending far out. Unfortunately, PS1 is not an all-sky survey, which might pose problems when looking at other streams, and only selected stars based on $S3_{ab}$ and it does not make any further differentiation between the different types of RRLs.

Hence, it would be great to have an all-sky sample documenting the type of RRL a specific star is. Therefore, we also decided to look at the Gaia DR3 catalogue of RRLs. This catalogue by Clementini et al. (2023) counts over 270,000 RRLs and has a column stating the type of RRL that it has been classified as. The one major downside of this dataset is the lack of distances to the stars. A catalogue of $\sim 136,000$ RRLs with distances has been published by Li et al. (2023). This catalogue unfortunately does not contain all RRL in Gaia DR3, as it only includes the stars from Clementini et al. (2023) with Fourier composition parameters available. However, the Li et al. (2023) Gaia sample still has more stars with distances than the PS1 sample.

2.2.1 Testing of the sample

To settle on which sample will be used in this thesis, the quality of the samples has to be assessed. We will look at the agreement between the distance estimates, the probability of being an RRL, and the apparent magnitude of the stars in the samples.

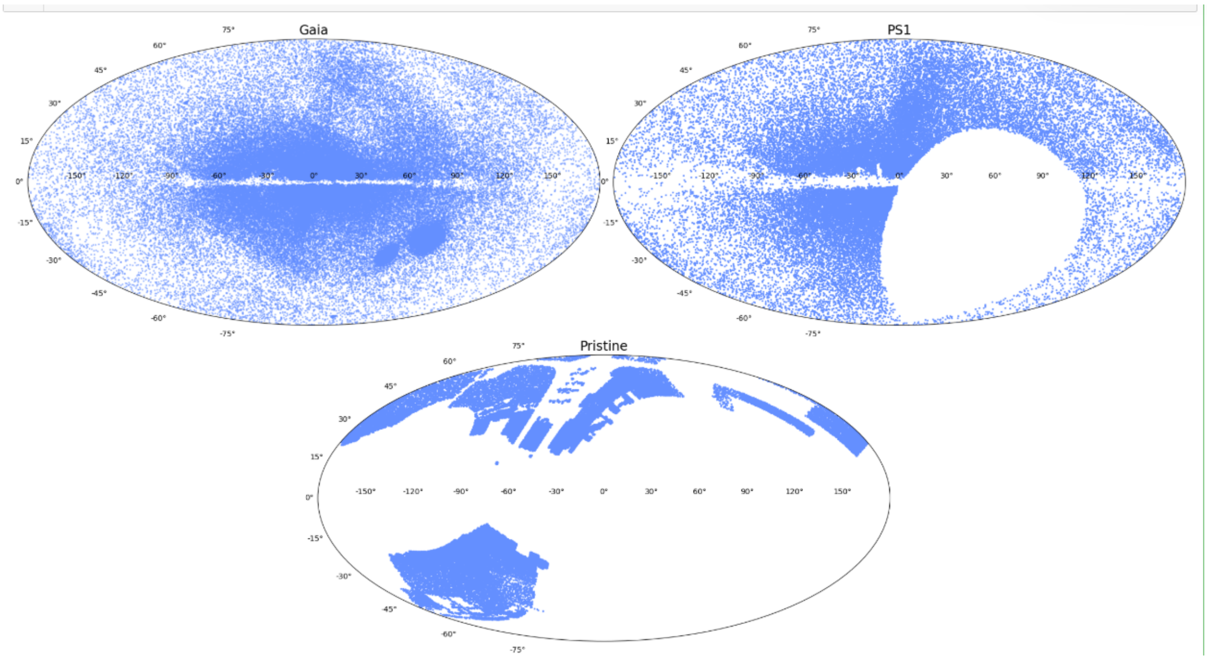

Figure 2.3: These three panels show the footprint of the three surveys on which the samples are based. The top left plot is the Gaia survey, the top right is the PanSTARRS1 survey and the bottom plot shows the Pristine footprint. The blue points are the stars in the samples

For the distance comparison, the two tables were crossmatched, taking only the stars that appear in both catalogues. The difference of the derived distances was taken for every star in both catalogues and plotted in Figure 2.4. In the image on the left, the mean and standard deviation are taken over all the points in the plot, while in the right plot, the mean and standard deviation are derived for every bin of 20 kpc. From this figure, it becomes apparent that the distances seem to agree with each other for nearby stars and become a bit more uncertain once we go farther out. It is noteworthy that at higher distances, the PS1 distances seem to be slightly overestimated compared to Gaia distances and that overall, PAN-STARRS1 assigns slightly higher distances than Gaia. It seems that the dispersion is a result of the increase in uncertainty on the distances. Overall, the distances seem to agree, and there is no strong preference for either.

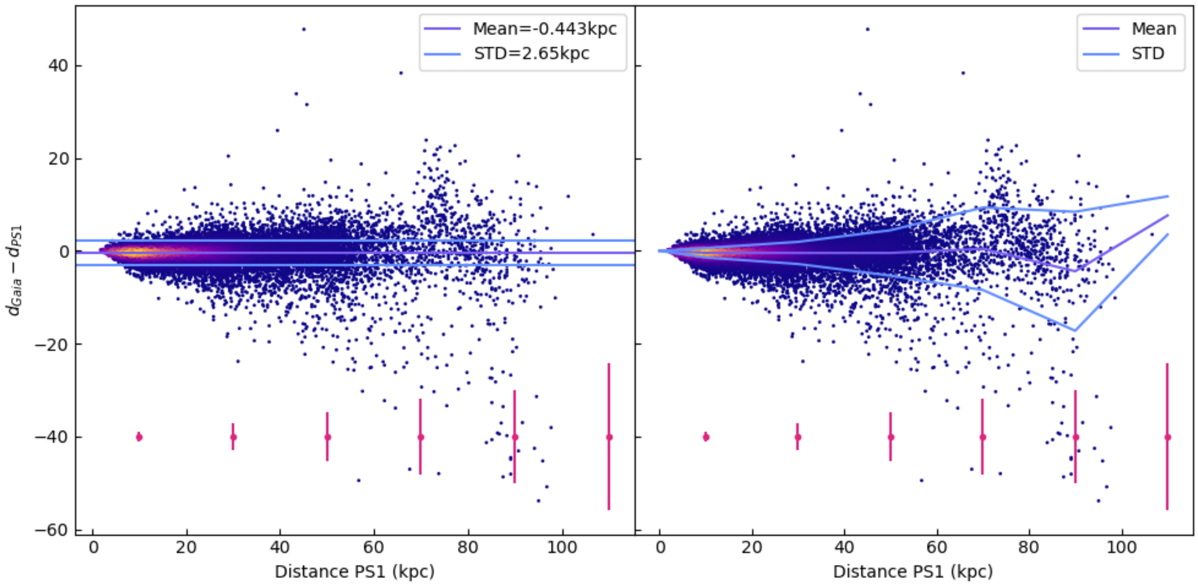

Figure 2.4: This figure displays the difference in distances attributed to individual RRLs by Li et al. (2023) and Sesar et al. (2017a). The pink lines at the bottom are the average uncertainty within 20 kpc bins. The right panel is essentially the same as the left panel but now the mean and standard deviation is calculated for 20 kpc bins.

Afterwards, a subsample of the Gaia RRL sample was taken, consisting of the stars that were also in PS1. For these stars, we looked at the magnitude and probability of being an RRab assigned by Sesar et al. (2017a) to see if the Gaia stars were more represented in a specific magnitude regime or probability of being an RRab. Looking first at the magnitude distribution, the left panel of Figure 2.5 shows that both samples observe in the same magnitude range, implying that we are observing RRLs in the same distance range. It appears that the PS1 survey does observe slightly fainter stars than Gaia. The right panel of Figure 2.5 shows that for magnitudes fainter than ∼ 19 dex, the ratio of stars in Gaia to stars in PS1 drops considerably. This means that the Gaia sample is significantly underrepresented at these magnitudes and hence goes less deep than PS1.

An interesting behaviour that can be seen for both surveys are the two spikes at $m_G \approx 19.3$ and $m_G \approx 20.1$. After applying the selection of Sgr described in Section 3.1, the bump at 20.1 disappears. The other bump at 19.3 correlates with parts of the Sgr stream itself. Figure 2.6 displays this well. The left panel is a polar plot of the full PS1 sample where we see clear overdensities at the radius corresponding to m_G ≈19.3 and 20.1. For 20.1 this corresponds to some globular clusters and extended features of the Sgr stream. The points that have $m_G = 19 - 19.6$ are highlighted in pink and belong to parts of the leading arm of Sgr.

The purity of the samples shows a great agreement in the quality of the samples. When plotting the score of being and RRab star from Sesar et al. (2017a) of both these samples, they seem to follow each other perfectly. Meaning that the distribution of the certainty of a star being an RRab is the same for both samples. We can hence conclude that the purity of the samples is comparable.

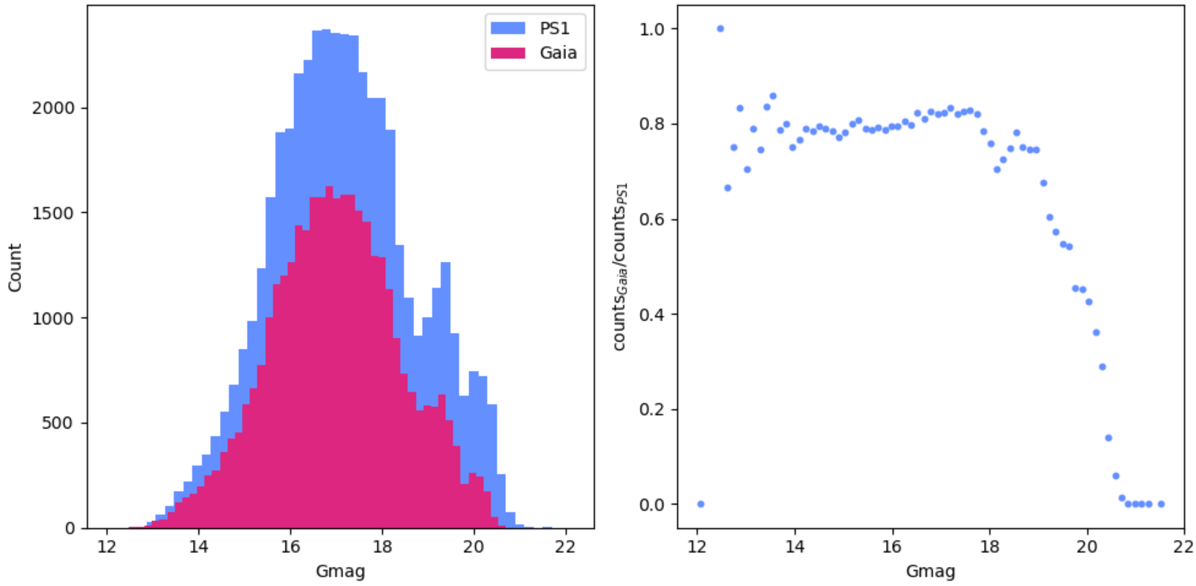

Figure 2.5: This plot compares the apparent G-band magnitudes in which the RRLs are observed in PAN-STARRS1(blue) and Gaia (pink). The right panel shows the ratio of the number of stars in Gaia vs PS1 in the bins displayed in the left panel. The ratio drops drastically after $m_G \approx 19$, indicating that Gaia has much lower completeness for magnitudes lower than 19.

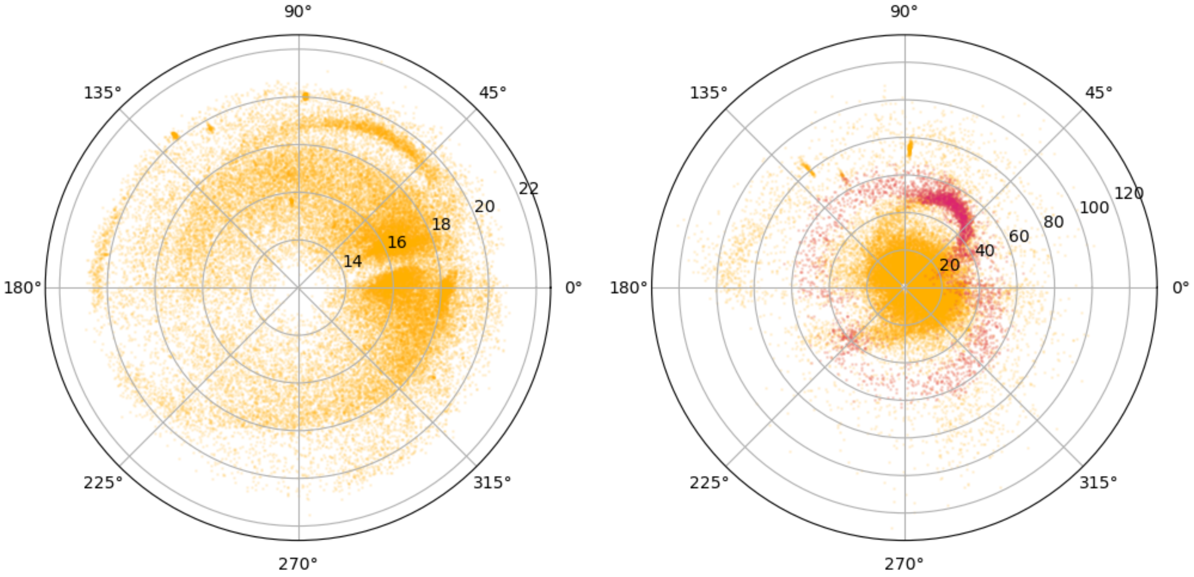

Figure 2.6: This figure shows polar plots of the PS1 RRL sample, where the angle is the stream longitude, $\Lambda_{\odot}$. On the left plot, the radius of the circle is the apparent dereddened G magnitude and on the right plot it is the heliocentric distance. The right plot also shows points highlighted in pink which correspond to the peak in Figure 2.5 and 19.3.

2.2.2 Conclusion on the RR Lyrae Sample

As the quality is comparable, there is no strong preference for either dataset. The main advantage of the PS1 dataset is that it has reliable distances for many stars and it traces the farther regions of Sgr better. Gaia on the other hand is far more numerous, all-sky, and includes RRab, RRc and RRd stars. We will not be comparing the different types of stars based on distances, as will be explained in Section 3. Hence the main advantage of the PS1 survey becomes somewhat obsolete. We therefore will use the Gaia catalogue using the Li et al. (2022) distances in the rest of this thesis, referred to as the L22 sample. We will include PS1 to check the results obtained from Gaia. As these two samples are independent of each other, our results will be more compelling if they show the same behaviour based on both samples.

The PS1 catalogue will also be used in Section 3 to test our selection of the streams. This catalogue will show accurately if our selection is rigorous enough to clean up foreground stars and ignore uncertain far-out stars, due to its reliable distances and high completeness at 80 kpc.

2.3 Blue Horizontal Branch Stars

Two samples for BHBs were used in this work. One sample (BHB1) was provided by M. Bayer (priv.com), which goes far out but is limited to the Pristine footprint. This sample is selected using the same technique as Starkenburg et al. (2019), but goes beyond, as it uses a more recent version of the Pristine data. Pristine continued collecting data and has thus a bigger footprint compared to the data released in 2019. The other sample (BHB2) is provided by A. Zwerver (priv. com), which is based on Gaia DR3 and uses the XP spectra to select the BHBs. This makes the sample all-sky but only extends out to approximately 16 kpc. In making these samples, they followed the same methodology as described in Starkenburg et al. (2019), where the broad-band SDSS ugr_0 and narrowband Pristine Survey $CaHK_0$ are used to identify candidate BHB stars efficiently. When plotting these values versus each other, two clear tracks can be seen, followed by Blue Straggler and BHB stars. These tracks, displayed in the left panel of Figure 2.7, are a good method to differentiate these two types of stars. A probability of being a BHB star is given based on their position relative to these two tracks. To keep our findings in line with the work by Starkenburg et al. (2019), we also only select stars with a probability of $p \geq 0.8$ in our sample. The sample did not include a distance column, hence the distance was calculated by first calculating the absolute magnitude in line with Deason et al. (2011)

$$G = 0.434 - 0.169(g_0 - r_0) + 2.319(g_0 - r_0)^2 + 20.449(g_0 - r_0)^3 + 94.517(g_0 - r_0)^4 \tag{2.1}$$

. We can use this with

$$d(pc) = 10^{\frac{m_G - M_G}{5} + 1} \tag{2.2}$$

to obtain the distances.

2.3.1 Testing of the Samples

The Pristine footprint limits the BHB1 sample, hence gaps are visible for the Sgr stream, as can be seen in the plot as displayed in Figure 2.3. We also found that some of the BHB stars extend very far out, even further out than the spur feature. These very extended sources were selected to see where they are located on the two tracks and looked up in SIMBAD. These sources were all quasars according to SIMBAD, which is interesting as all the variable sources should have been filtered out of the sample. When highlighting these quasars in the right plot in Figure 2.7

we can see where these sources are in the sample. The quasars are far removed from the tracks and are only included due to their large error bars. As the quasars are the only sources so far to the right of the tracks, we do not think this problem further affects our sample. In a more recent sample by M. Bayer, released after the work in this thesis was performed, a quality cut was performed on $CaHK$, where only the sources with $\Delta CaHK < 0.1$ were kept. This should eliminate the quasars found in this work.

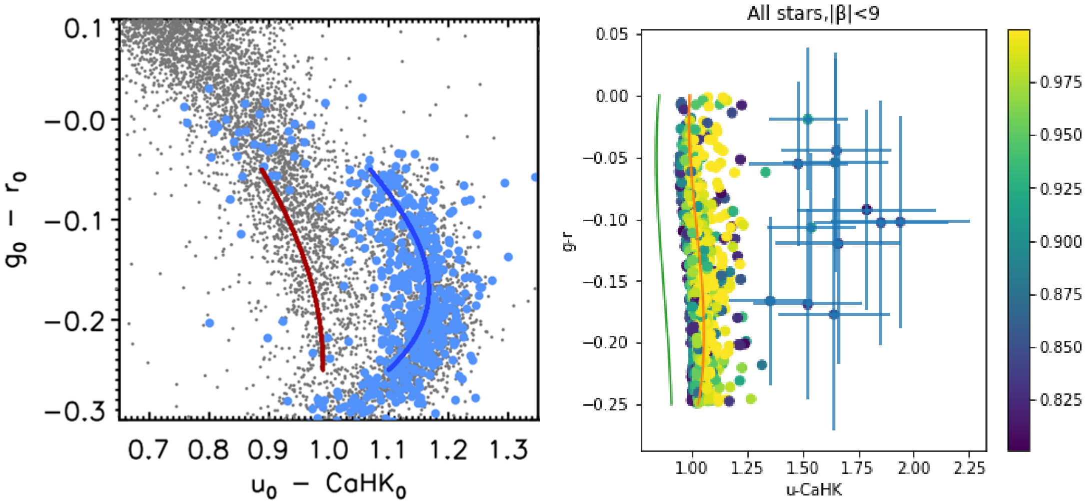

Figure 2.7: The left panel shows the tracks that were used to separate the BHBs from the BSs(Starkenburg et al., 2019). The tracks are defined by Deason et al. (2011), where the blue track defines the BHBs and the red one the BSs. The light blue points are the BHB sample from Xue et al. (2011). The right panel displays the used BHB sample. The stars are colour-coded on the probability of being a BHB star. The stars that have error bars are the stars in the far-out feature displayed in Figure 3.3, which turned out to be quasars. As these stars are the only ones so far removed from the tracks and have large error bars, we don't think it will influence the rest of the sample much. The green and orange lines are the tracks for the Blue Stragglers and BHBs respectively.

2.3.2 Conclusion on the BHB Sample

The final BHB samples used in this work will consist of all the stars with $p_{BHB} > 0.8$ from the catalogue composed by M. Bayer (BHB1) and A. Zwerver (BHB2), where BHB1 will be used for structures that are farther away than 16 kpc, and BHB2 will only be used if they are closer than that. We investigated a suspicious feature in BHB1 at very large distances which turned out to be quasars. They appear to be a small subset of the catalogue and are a distinct group in Figure 2.7, so they can be easily filtered out. As they are so distinct from the rest of the stars in the sample, it is not expected that there will be any further similar significant contaminations.

Chapter 3

Methods

Three streams will be looked at to investigate the connection between the presence of the three types of stars and the properties of the progenitor system and streams. These streams are the Sgr stream, Jhelum and GD-1. To avoid any biasing between the different types of samples, the selection of members of the stream will be done using Gaia parameters that all catalogues have in common. Hence the selection will be done on position, proper motion and parallax. In the following sections, these selections will be explained, as well as the coordinate transformations for each stream and what the selections are based on.

3.1 Selection Sagittarius Stream

The Sagittarius stream is the main focus of this thesis, hence a method was developed to select the stream in all our samples, without introducing a bias for one of the samples. To select the stream, we shift the coordinate system to a longitude and latitude defined with respect to the Sgr orbit, with the centre of the Sagittarius dwarf as the centre of our coordinate system ($\Lambda_\odot$ and $\beta\odot$). The transformation from Belokurov et al. (2014) is used to go from right ascension, α, and declination, δ, to $\Lambda_\odot$ and $\beta\odot$ is

$$\begin{aligned}\Lambda_\odot = \operatorname{atan2}(&-0.93595354\cos\alpha\cos\delta - 0.31910658\sin\alpha\cos\delta + 0.14886895\sin\delta,\\ &0.21215555\cos\alpha\cos\delta - 0.84846291\sin\alpha\cos\delta - 0.48487186\sin\delta)\end{aligned} \tag{3.1}$$

$$\beta\odot = \arcsin(0.28103559\cos\alpha\cos\delta - 0.42223415\sin\alpha\cos\delta + 0.86182209\sin\delta). \tag{3.2}$$

To now select the stars within the Sagittarius stream, a cut on $\beta\odot$ is made where only stars with $|\beta_\odot| < 20^\circ$ are selected. To demonstrate the effect of this cut, the RRL sample was used to perform the data selection in steps. On the left panel of Figure 3.1, the L22 sample can be seen after the cut in β. The Sgr stream has already become very visible, but there is still much contamination from foreground stars and globular clusters.

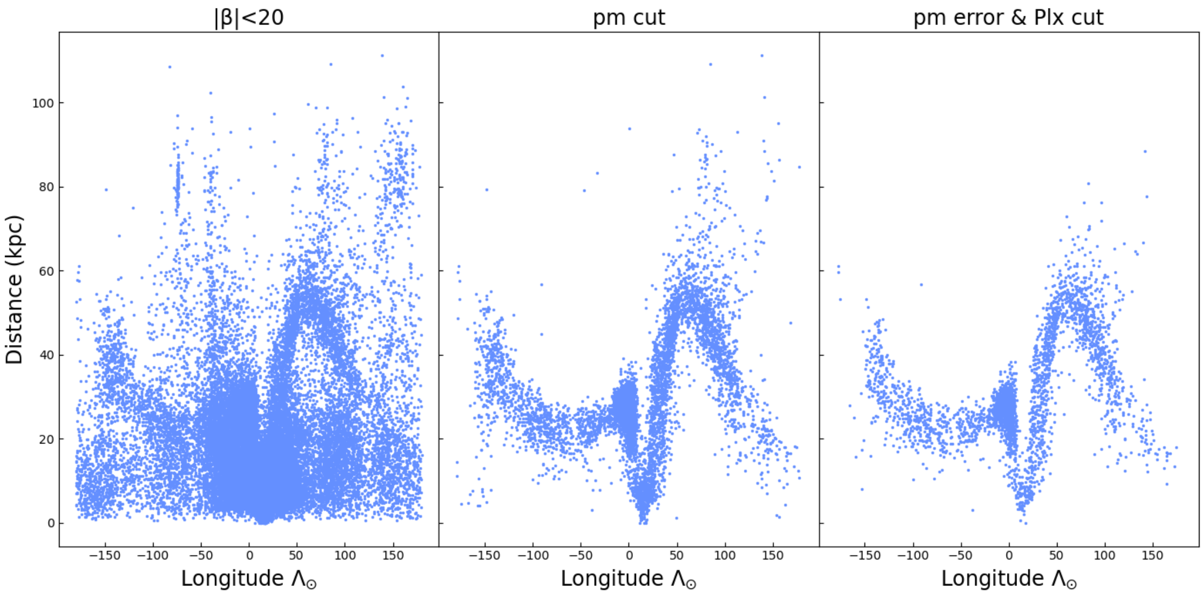

Figure 3.1: These panels display the various selection and clean-up stages of Sgr. At first, a selection based on stream longitude was made ($\beta_\odot$, left panel), followed by proper motion in ra and dec (middle panel) and lastly clean-up by making cuts on the parallax and error in proper motion (right panel).

Therefore, a second cut was made based on the proper motion of the stars in right ascension and declination. The proper motion of Sagittarius is not constant over the stream but varies throughout (V21). The N-body simulation of the Sagittarius stream presented in V21 was used to select the stars on proper motion. A continuous function of proper motion across the stream is needed to select the stars. Therefore, a running average was taken over the simulated proper motion of the test particles, which was then interpolated to get a continuous function. The upper and lower boundaries were taken to be the 95th percentile and the 5th percentile, respectively, to reduce outliers in our fit but maintain the bulk of the simulated data. All stars with a longitude higher than 150° were removed, because the proper motion distribution of the simulated stars flares out considerably after this point. It is therefore difficult to effectively select stars based on proper motion for stars at higher longitudes. All the proper motions are retrieved by crossmatching the catalogues with Gaia. To avoid biases in the selection between the different catalogues, we select the stars on proper motions, as all the proper motions come from Gaia and there is therefore no influence from the instrument from which the sample came.

The selection based on proper motion cleaned up a large part of the foreground contamination as can be seen in the middle panel of Figure 3.1. Unfortunately, some foreground contamination near the core, where Sgr crosses the disk, persisted. So an extra cut based on parallax was made, where all stars with a parallax lower than 0.05” were kept in the sample. Furthermore, this selection still included some further out parts of Sgr, such as the trailing arm apocentre and spur feature. These structures are likely still in the selection due to larger uncertainty on their proper motion, and thus still fall within the selection bounds. A final cut on error is proper motion is done, where only stars with a proper motion error smaller than 0.6 are selected. These final two cuts complete the selection of Sgr. The right panel of Figure 3.1 shows how the last two cuts influence the selection. The samples resulting from these cuts are displayed in Figure 3.3 and contain 3420 RRLs, 167 BHBs and 2455 RGBs. A plume of stars called "feature 3" is also indicated and will be discussed in more detail in Section 4.1.3

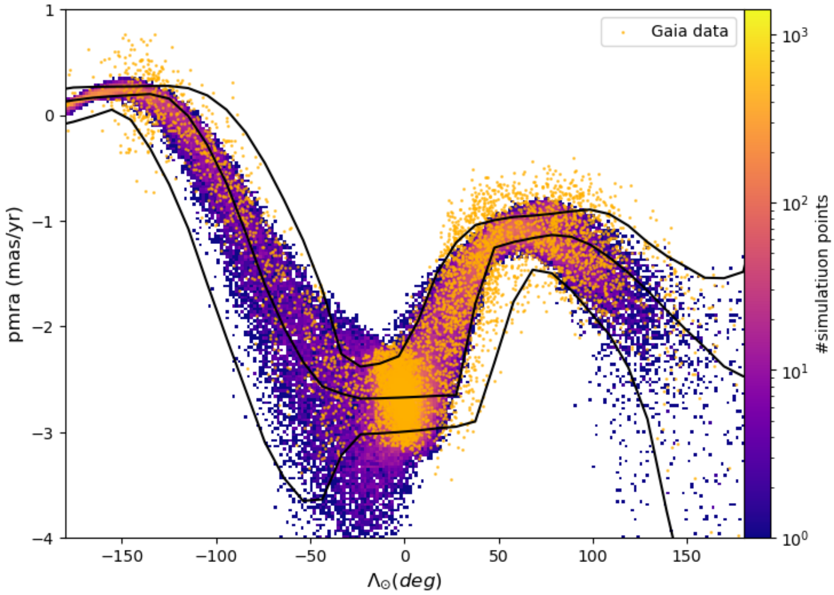

Figure 3.2: The colour-coded points illustrate the test particles from the N-body simulation from the simulation presented in V21. The centre black line is a running average taken over the test particles and the outer black lines encompass 90% of the data. The yellow points are the RRLs selected on pmra and pmdec as described in Section 3.1.

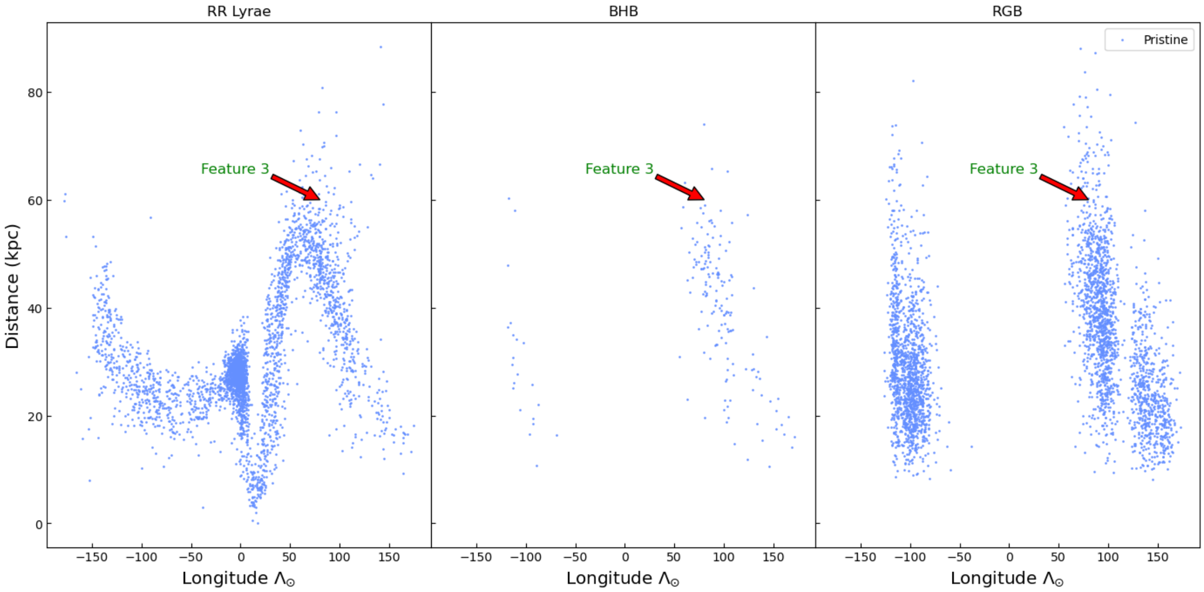

Figure 3.3: The three Sgr samples used in this thesis, are converted and selected as described in Section 3.1. On the left panel, we see the L22 sample for the RRL. In the middle one, we see the BHB1 sample. The right panel shows the VB1 sample for the RGB stars.

As a quick check of the distances from the different samples, a running average was taken over the samples, which gave Figure 3.4. This one plot, which was meant as a sanity check, quickly revealed features in our samples and of the stream which had gone unnoticed till now. The blue line represents the RRLs and has the distances that we trust the most. We will therefore

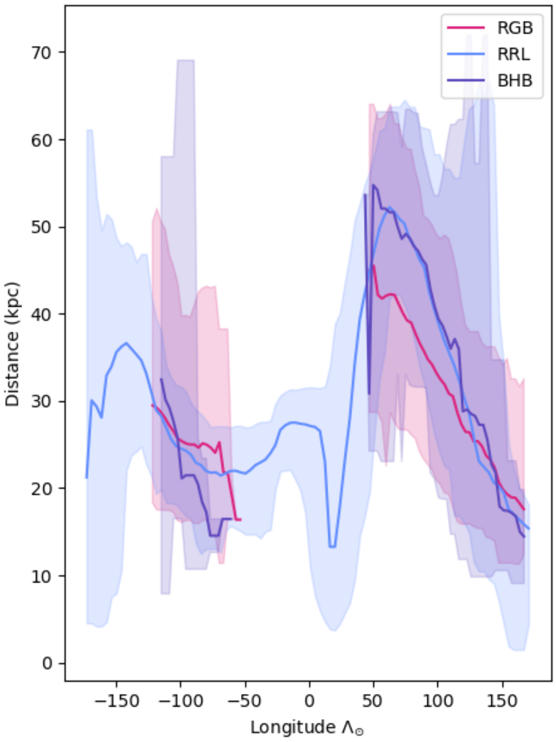

Figure 3.4: The plot displays the running average of the distances of the samples from Figure 3.3 used for Sgr. The shaded regions are the middle 90% of the stars selected to be part of Sgr.

compare the distances of the other samples to the RRL sample.

The BHB1 sample appears to be in good agreement with the L22 sample. We can see that the distances of the VB1 sample are slightly underestimated around the leading arm apocentre. Due to larger uncertainties for the individual distances for the RGB stars, we can shift the distances of this sample up a bit for later comparisons.

3.2 Selection Jhelum

We also looked at other, smaller streams to expand our science case. One of which is Jhelum. The selection presented in Awad et al. (2024) will be used to select this stream. They used the LAAT stream finding algorithm to define the Jhelum stream members on position. Based on that sample, they defined its proper motion range. To start our selection, we must transform into the Jhelum frame (ϕ_1, ϕ_2) as defined in Bonaca et al. (2019) and implemented in `gala`.

The stars' proper motion is also converted into the Jhelum coordinate frame, yielding μ_{ϕ_1} and μ_{ϕ_2}. This is also done using the `gala` module, where a constant distance to the stream of 13 kpc is assumed (Awad et al., 2024). Now that we have the quantities to select Jhelum on, the following cuts are made:

- Select the longitude to be between $-5°$ and $30°$, $-5° <$ `phi1` $< 30°$,
- Select the latitude to be between $-5°$ and $5°$, $|$`phi2`$| < 5°$,
- Select proper motion in ϕ_1 between -8 and -4 [mas/yr], $-8 <$ `pm_phi1` < -4 [mas/yr],
- Select proper motion in ϕ_2 between -2 and 2 [mas/yr], $|$`pm_phi2`$| < 2$ [mas/yr].

As Jhelum is at an approximate distance of 13 kpc, we can use the VB2 sample for the RGBs and the BHB2 sample. Applying the selection to our RGBs, BHBs and RRLs gives us 118, 11 and 9 stars, respectively. The distribution of these stars is displayed on the top panels of Figure 3.5

3.3 Selection GD-1

The other smaller stream that we will cover in this work is GD-1. For this selection we followed the work of Price-Whelan & Bonaca (2018), where we start by moving to the GD-1 coordinate system presented in Koposov et al. (2010). There they defined the longitude and latitude (ϕ_1 and ϕ_2, respectively) as

$$\begin{Bmatrix} \cos(\phi_1)\cos(\phi_2) \\ \sin(\phi_1)\cos(\phi_2) \\ \sin(\phi_2) \end{Bmatrix} = \begin{Bmatrix} -0.4776303088 & -0.1738432154 & 0.8611897727 \\ 0.510844589 & -0.8524449229 & 0.111245042 \\ 0.7147776536 & 0.4930681392 & 0.4959603976 \end{Bmatrix} \times \begin{Bmatrix} \cos(\alpha)\cos(\delta) \\ \sin(\alpha)\cos(\delta) \\ \sin(\delta) \end{Bmatrix} \tag{3.3}$$

These coordinate transformations are also defined in `gala`, where they also have a function to transform the proper motions into this coordinate frame. To make this transformation on the proper motions, we again assumed the stream to be at a constant distance of 12.3 kpc Koposov et al. (2010). Having obtained the new coordinates and proper motions of GD-1, we can now do the selection of the stream as follows:

- Select the longitude to be between $-100°$ and $20°$, $-100° < \texttt{phi1} < 20°$,
- Select the latitude to be between $-1°$ and $1°$, $|\texttt{phi2}| < 1°$,
- Select proper motion in ϕ_1 between -9 and -4.5 [mas/yr], $-9 < \texttt{pm\_phi1} < -4.5$ [mas/yr],
- Select proper motion in ϕ_2 between -1.7 and 1 [mas/yr], $-1.7 < \texttt{pm\_phi2} < 1$ [mas/yr].

Due to its proximity, we can use the VB2 and BHB2 samples. The above selection gave us a sample of 93 RGBs, 6 BHBs and 8 RRLs. The distribution of these stars is displayed on the bottom two panels of Figure 3.5

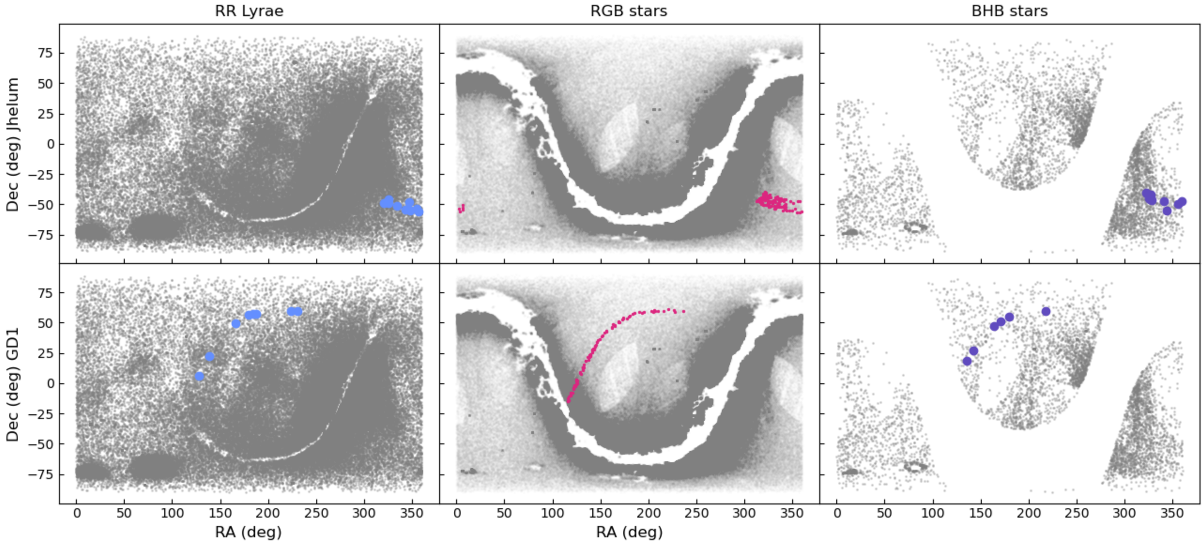

Figure 3.5: The figure displays the distribution of RRLs (left panels) and RGB stars (right panels) on the sky for the Jhelum (top panels) and GD-1 (bottom panels). The selection of these streams is based on work done by Awad et al. (2024) and Price-Whelan & Bonaca (2018) and are described in depth in sections 3.2 and 3.3

Chapter 4

Results

In this chapter, I will investigate the properties of the streams selected from various tracers and the ratios between them. This will provide us with a complete view of their stellar populations. One of our main goals is to investigate the link between the metallicity and the ratios of the star types for these streams. To calculate the ratio between the stars, the total amount of one type of star in a patch was compared to that of another type of star in the same patch. Hence, the ratios can be expressed as

$$R = \frac{N_1}{N_2} \tag{4.1}$$

A Poisson distribution well describes the errors in this quantity, hence the error on this ratio can be expressed as

$$\sigma_R = \sqrt{R\frac{N_1 + N_2}{N_2^2}} \tag{4.2}$$

This plot and ratio calculation will be done for every stream and with all the surveys available for the stream in question.

As mentioned in Section 1.5, the CMDs of stellar populations can tell a lot about their properties, such as metallicity, age, and star formation history. Therefore, the CMD of the different streams and stream sections will also be compared to see if we can infer anything about the stellar populations from the differences in CMD.

4.1 Sagittarius

4.1.1 The Metallicity Structure of the Sgr Stream from Various Tracers

To investigate the behaviour of the metallicity across the stream, it is important first to get some insight into the metallicity distribution. The work by Cunningham et al. (2024) was followed to do this. They looked at RGB stars in the Sagittarius stream and detected a metallicity gradient across the stream as a function of stream latitude. When looking at the bottom panel in Figure 1 of Cunningham et al. (2024) it also becomes apparent that the metallicity in the leading and trailing arms differs (see Figure 4.1). It is higher in the trailing arm and lower in the leading arm. This method is very insightful in understanding how metallicity varies throughout the stream. This type of plot will be recreated for all streams covered in this work to gain more insight into the metallicity distribution of the streams. It will only be made with RBGs and RRLs, as the BHBs in the used catalogue do not have metallicities.

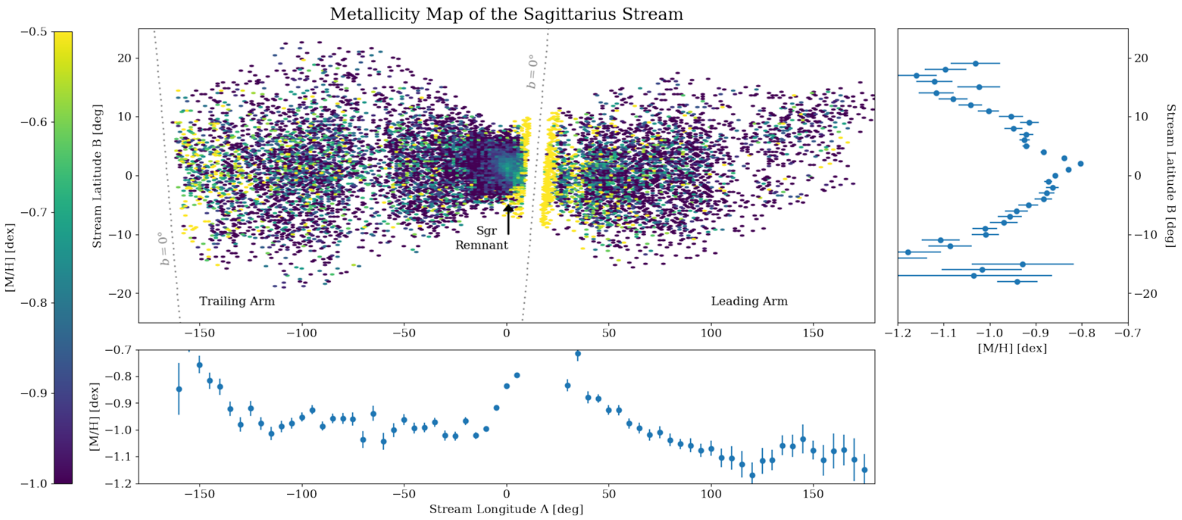

Figure 4.1: This figure is Figure 1 from Cunningham et al. (2024), where the top panel shows the RGBs from Andrae et al. (2023) plotted in stream coordinates and colour-coded by metallicity. The bottom and right panels show the mean metallicity binned in stream longitude and latitude, respectively.

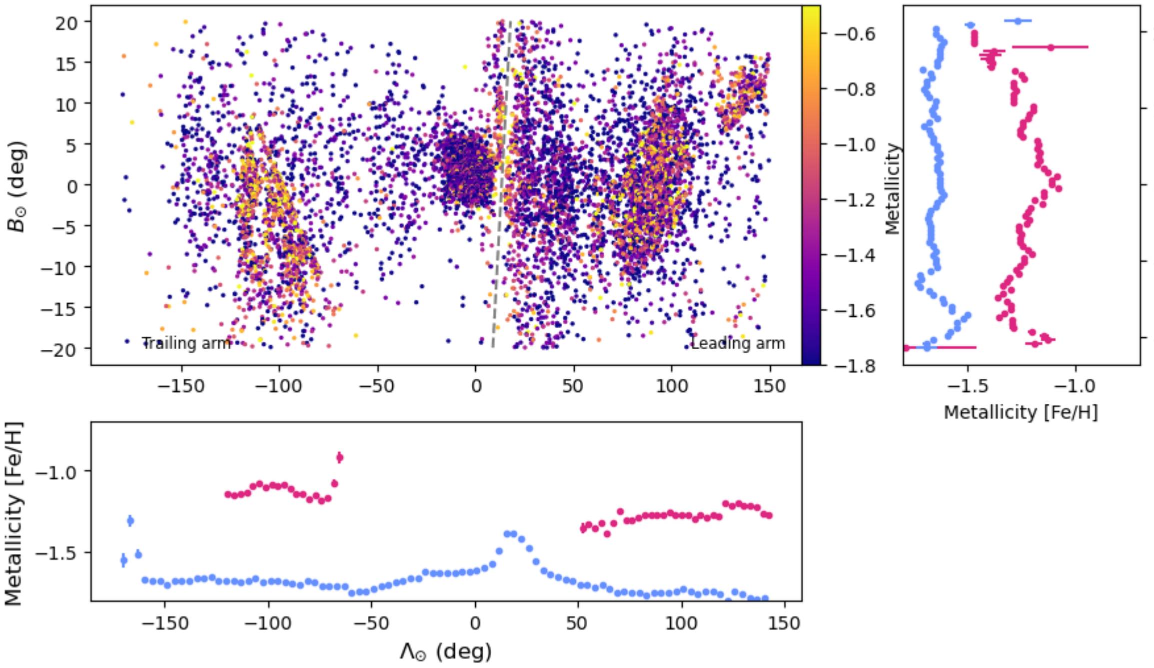

Figure 4.2: These panels illustrate the metallicity distribution of Sgr using RRLs and RGBs. The top left plot shows stars selected to be in Sgr as described in Section 3.1, plotted in Sgr stream coordinates $(\Lambda_\odot, B_\odot)$ and are colour-coded on [Fe/H] from Viswanathan, Byström, et al., 2024 and Li et al. (2023). The right panel plots the mean metallicity binned in stream latitude, and the bottom panel is binned in stream longitude. The dashed grey line indicates the galactic plane. The pink points are the RGBs, and the blue points are the RRLs.

Figure 4.2 shows the distribution of metallicities in Sgr using our samples and selection of the Sgr stream. The RRL metallicity distribution, plotted in blue, seems to follow the RGB metallicity distribution reported in Figure 1 of Cunningham et al. (2024) very well. The metallicity is on average higher in the trailing arm than in the leading arm, just as we see in Cunningham et al. (2024). Interestingly, the RRLs are shifted down compared to the RGB metallicities.

In contrast to the RRLs, the RGBs in this work have comparable values to those reported in Cunningham et al. (2024), with only small offsets. They also show the metallicity gradient with stream latitude. As the Pristine footprint limits the RGB sample, only two patches of Sgr are visible, one in the trailing arm and the other in the leading arm. In these two patches, an offset is visible between the metallicities, with a higher metallicity in the trailing arm. To keep the comparison between RRL, BHB and RGB stars fair, the Pristine footprint was imposed on the all-sky RRL sample for the ratio calculations later. Two patches were selected, one in the trailing arm and the other in the leading. The goal was to use the Pristine footprint optimally, which gave the following selection

- Trailing arm patch: $\Lambda_{\odot} < -50$
- Leading arm patch: $B_{\odot} > 0.35\Lambda_{\odot} - 43$

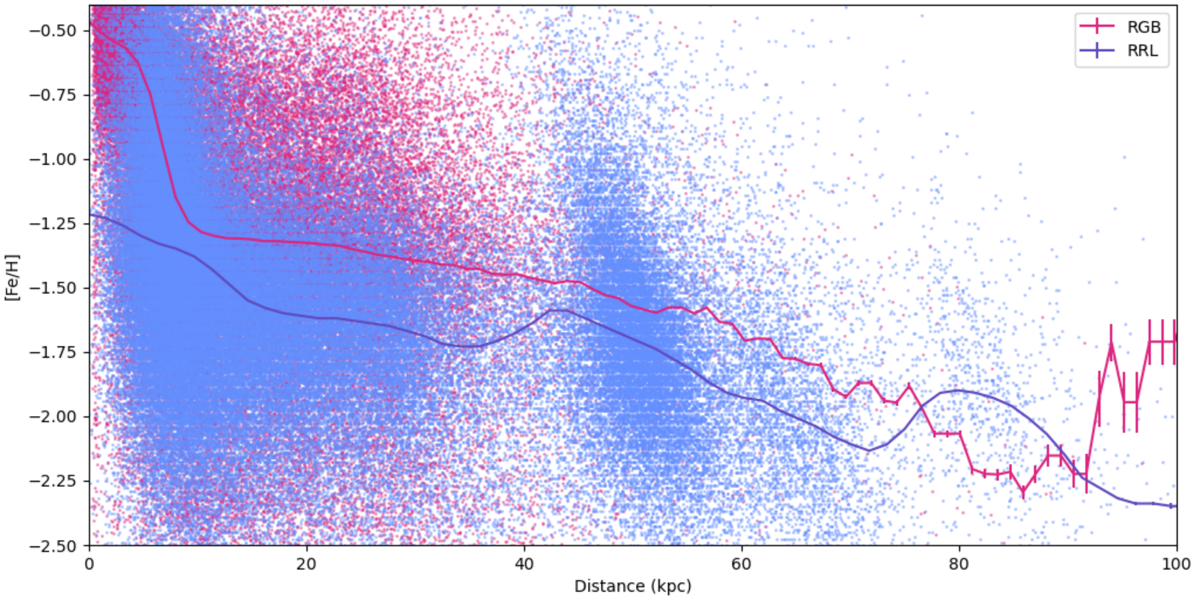

Figure 4.3: This plot shows the metallicity distribution as a function of distance. The pink line is the RGB stars and the blue line is the RRLs. In the regime of our patches of Sgr (20-40 kpc), the metallicity of the RRL seems to be lower on average than the RGB metallicity. This could be due to an observational bias or be due to features in the stellar populations.

Figure 4.3 shows the metallicity of the RGBs from VB1 and RRL from L22 as a function of distance to investigate the offset in metallicity between the RRLs and RGB stars in the Sgr stream. From this figure, we can see that the RRL sample indeed seems to trace mostly the metal-poor populations, as its average metallicity is systematically lower across all distances. However, interestingly, higher metallicity RRLs exist in the sample, mainly close by and around 50 kpc. We can furthermore see from Figure 4.3, that the RGB star sample is not influenced by this, and has a decently constant metallicity range between 10-50 kpc. This is pretty nice, as the (sections of the) streams that we will cover in this work are in this range. Hence, if the overall metallicity stays stable in the entire catalogue, any differences that we will see later in this analysis are most likely caused by the stream itself.

4.1.2 CMD and Stellar Ratios

The ratios of the different types of stars between the leading and trailing arms give more insight into what is happening in these sections of Sgr. These ratios are displayed in Table 4.1. The most telling of these is the ratio between RGBs and RRLs, where they differ by an order of magnitude. We see relatively more RGBs in the metal-richer patch (trailing arm) than in a metal-poor environment (leading arm). These results are consistent for the ratio between RGBs and BHBs, where all differences remain within 3σ. These results indicate that the ratios would be a good tracer for metallicity. Interestingly, the ratio between RRL and BHB seems to stay almost constant between patches.

	RRL/BHB	RGB/RRL	RGB/BHB	$[\mathrm{Fe/H}]_{\mathrm{RGB}}$	$[\mathrm{Fe/H}]_{\mathrm{RRL}}$
Trailing arm	2.62 ± 0.67	19.1 ± 2.7	50.1 ± 11	-1.1 ± 0.02	-1.7 ± 0.05
Leading arm 1	2.47 ± 0.25	3.0 ± 0.18	7.41 ± 0.66	-1.3 ± 0.02	-1.8 ± 0.02
Leading arm 2	1.82 ± 0.36	14.4 ± 1.7	26.3 ± 4.2	-1.3 ± 0.02	-1.8 ± 0.09

Table 4.1: The ratios between different types of stars within specific areas with Sgr are displayed in this table. The trailing arm is selected as $\Lambda_{\odot} < -50°$. Leading arm 1 is the initial selection of the leading arm, which had the downside of being at a different distance regime than the leading arm selection but made optimal use of the Pristine footprint. Leading arm 2 is an improved selection in a more comparable distance regime. The uncertainties on the ratios have been calculated with Equation 4.2 and the uncertainty for the mean metallicity is the uncertainty on the mean calculated as $\sigma_{[\mathrm{Fe/H}]}/\sqrt{N}$.

However, the difference in metallicity in these two patches is relatively small, especially within the given uncertainties. Hence, such a big difference in the ratio is unexpected. So we investigate if there could be another factor that influences this ratio. A reasonable explanation would be that the distances of the two patches are different. The completeness at various distances in the samples could vary from one sample to another. So the ratio between stars does not vary because there are physically fewer stars in that part of the stream, but because the completeness of one of the samples varies across the stream. The left panel of Figure 4.4 shows the distribution of distances in the patches displayed in the left panels of Figure 4.5. From this figure, it becomes evident that the two patches probe two distance regimes. As this can heavily influence the completeness of the samples in the patches, the patch in the leading arm will be moved to where the distance regimes will be more comparable. This new patch is defined as $\Lambda_{\odot} > 103$ and moves the distances downward to around 35 kpc. The distance distributions of this new selection are displayed in the right plot in Figure 4.4 and the ratios in Table 4.1. We note that we are restricted to the Pristine footprint and can therefore not select patches that perfectly overlap in distance. However, this new configuration allows us to test the assumption that the distances are largely responsible for the observed differences.

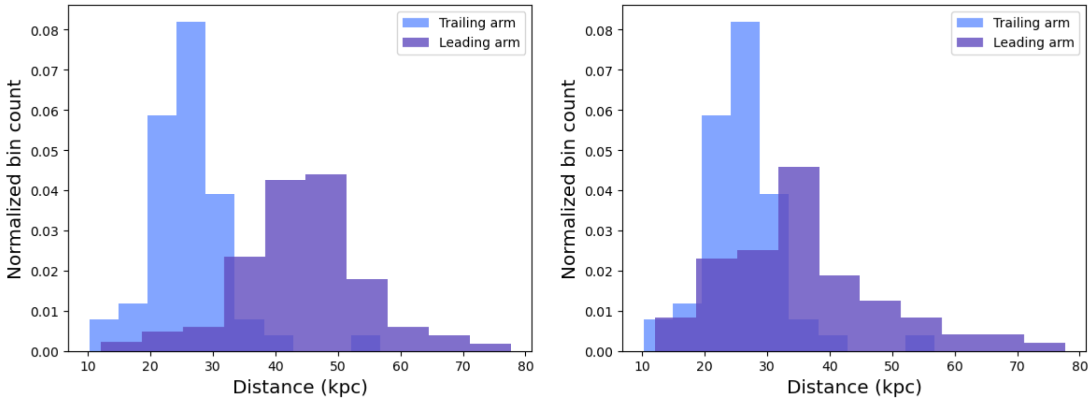

Figure 4.4: These plots display the distance distribution of RRL of selected areas in Sgr. The left plot shows the distance of an initial selection to optimize the usage of the Pristine Footprint. Unfortunately, this selection does not return patched with comparable distances. Therefore, the selection of the leading arm was altered to make the distance regimes more comparable, which yielded the distance distributions displayed on the right.

Indeed, this new selection of the leading arm of Sgr influences the ratios quite a lot. The order of magnitude difference that could be seen with the previous selection seems to disappear completely when comparing the bottom 2 rows of Table 4.1. The selection's metallicity stays the same. The differences in the ratios between the leading and trailing arm have shrunken, but still hold up for RGB/RRL and RGB/BHG within 1σ.

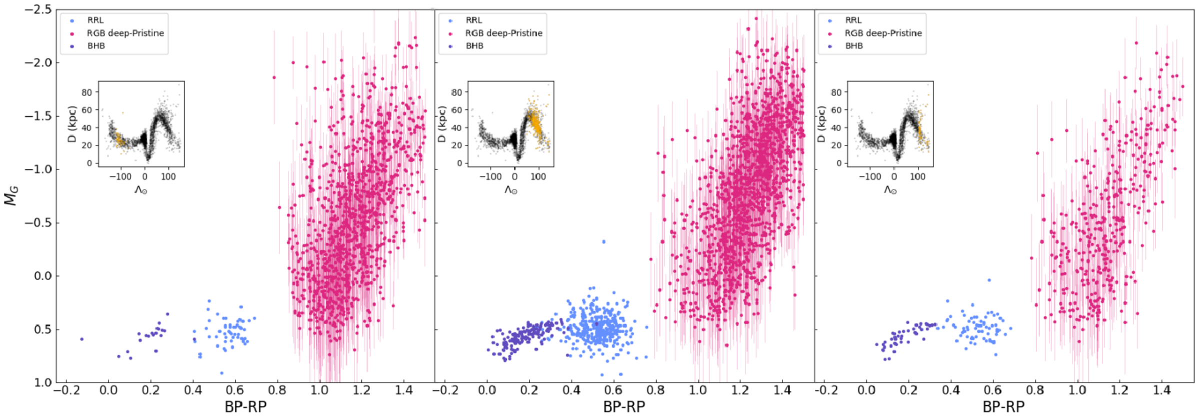

Figure 4.5: These plots display the CMDs of different patches selected within Sgr. The left panel displays the leading arm, and the middle and the right panels show the initial and final selection of the trailing arm, respectively. In this CMD, the BHBs (purple), RRLs (blue), and RGBs (pink) are plotted.

The stars from this new selection were plotted in a CMD displayed in the left and right panel of Figure 4.5. The error bars on the RGB in this figure are based on the uncertainties given in the VB2 catalogue for the photometric distance. These uncertainties are systematic and based on the T_{eff}, $\log g$ and the photometric metallicities (for more details on the error determination, see Section 3.5 of Viswanathan, Byström, et al., 2024). To calculate the error on the absolute magnitude, we took the uncertainty of the distance and used error propagation on Equation 2.2. We did not take the error on the apparent g magnitude into account, as these errors were negligible. The RGB of the trailing arm seems to be denser populated and flares out a bit more at brighter magnitudes, which might be an effect of having more stars in general in this patch. The HB of the trailing arm is much more populated compared to the HB in the leading arm. These features indicate that the population in the leading arm is more metal-poor. There is one BHB star in the trailing arm at ≈ -0.2, which would indicate a metal-poor population, but this could also result from more efficient mass loss when that star was on the RGB.

An interesting feature of the CMD of Sgr's trailing arm is the gap between the RRLs and BHBs on the HB. The BHBs start at a comparable point to the leading arm; hence, the RRLs are a bit redder in the leading arm. This could be due to a lower density of BHBs and RRLs in the trailing arm. A more in-depth analysis of the properties and distribution of the BHBs and RRLs is needed to definitively explain this gap.

4.1.3 Feature 3

Figure 3.4 shows that the distance of the BHBs varies slightly at lower longitudes. The lower amount of data points in this region can explain this. However, when going to higher longitudes, the BHBs shoot up in the distance around 120°. Figure 3.3 displays a plume of stars around that longitude in the RRL sample. Sesar et al. (2017b) has noted this plume as "feature 3". Feature 3 has also been confirmed to be present in BHBs by Fukushima et al. (2018). A small increase at the same longitude can be seen in the RGB Pristine sample in Figure 3.4. There is a denser region below $\approx$ 48kpc and a more diffuse patch of stars above. For BHB and RRL, this transition is around 55 kpc. The distance for RGB seems to be underestimated. From this and the comparison in Figure 3.4, we find that the difference is approximately 15%. When we compensate for this effect by shifting the RGBs by 15% the transition from the dense to the diffuse region happens at approximately the same distance.

Feature 3 is likely the result of stars with higher orbital energy that overshoot slightly when Sgr approaches the apocentre (Fardal et al., 2019). Hence if one of the samples is underrepresented in feature 3, this might indicate that some stellar populations follow a different orbital energy distribution in the original dwarf galaxy.

To see how well-represented Feature 3 is in our samples and the simulations, we will compare the amount of stars in Feature 3 to the amount in the leading arm. Feature 3 is visible between $50^\circ < \Lambda_\odot < 140^\circ$ and starts after approximately 55 kpc. Hence to separate feature 3 from the leading arm, we define feature 3 as the stars above 55 kpc between $50^\circ < \Lambda_\odot < 140^\circ$. This will be compared against the portion of the leading arm directly below feature 3, so all stars below 55 kpc and between $50^\circ < \Lambda_\odot < 140^\circ$. The ratio is defined as the stars in feature 3 divided by the stars in the trailing arm and results in 0.177 ± 0.018 for RRL, 0.126 ± 0.033 for BHB and 0.103 ± 0.010 for RGB (after distance correction), which are also displayed in Figure 4.6. These ratios were also checked with the RRL from PS1, which yielded a value of 0.17 ± 0.015. This value agrees well with the main RRL sample and thus indicates no significant difference between the two RR Lyrae catalogues. The average ratio based on all our observational samples is 0.144 ± 0.042. The ratio from the RGB sample seems to disagree the most with the rest of the observational ratios, although it is still within uncertainties. This could be caused by the uncertainty of the distances. As previously mentioned, the distances seem to be off by an average factor of 1.15, and there might be further inaccuracies. As the selection of the compared areas is based on distance, the collection of stars attributed to be part of Feature 3 might not be very pure or complete for this sample.

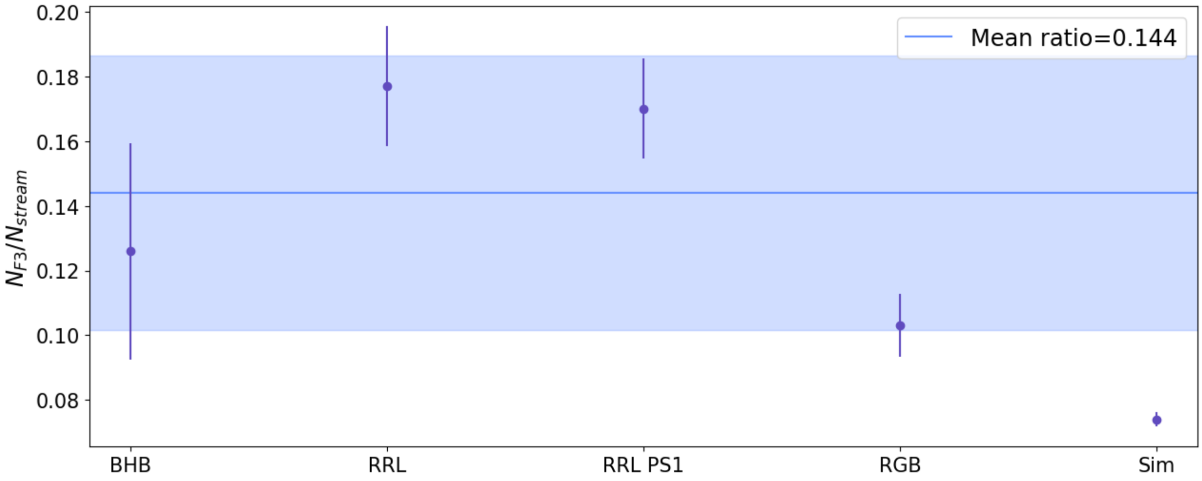

Figure 4.6: The figure displays the ratios of stars above and below 55 kpc, between $50° < \Lambda_{\odot} < 140°$. This division is made to select the stars in Feature 3. These ratios were calculated for the BHB, deep-Pristine RGB, Gaia RRL and PS1 RRL samples. The mean ratio was calculated for the first three samples, as the rest of the comparison is also based on these. The same ratio was also calculated for the stellar particles from the Vasiliev et al. (2021) simulations and are plotted on the far right.

We think that feature 3 is present in all three samples and would hint at a progenitor system with a larger orbital energy component that results in a plume of stars near the apocentres of the stream. This feature near the apocentres can also be seen in the simulations from Vasiliev et al. (2021). One big difference between the morphology of feature 3 in the N-body simulation and Figure 3.3 is that the feature seems much more concentrated in the simulations, which might disfavour the large orbital energy explanation(Fardal et al., 2019). It would therefore be interesting to make a similar comparison with the stellar particles used in the Vasiliev et al. (2021) simulations. This yielded a 0.074 ± 0.002 ratio, which does not agree with the observational ratios. This could mean that the assumed velocity distribution in the Vasiliev et al. (2021) simulations of the Sgr progenitor is incorrect. However, this difference can be overcome by making small changes to the basic dynamical model. By introducing these changes, Fardal et al. (2019) says that feature 3 is probably an older, higher-energy stream component. The simulations might also underestimate this ratio due to the lack of binary systems, clusters, and random interactions between stars. Since they use an N-body simulation, these smaller-scale interactions and inhomogeneities in the density profile of the progenitor are not accounted for. If these effects were accounted for in the simulations, we expect the ratio to be higher and would thus be in better agreement with the observational ratios.

4.2 Jhelum and GD-1

4.2.1 The Metallicity Structure of Jhelum and GD-1

Now that we have covered the Sgr stream, we will expand on it by also looking at other streams, that are closer by and have a less massive progenitor than Sgr. We will try to keep the analysis as similar as possible. Unfortunately, L22 contains only a few RRLs in both Jhelum and GD-1, hence the ratios will be calculated for the entire stream instead of patches within the stream. Therefore, the ratio comparison will be between Jhelum and GD-1. VB2 on the other hand, seems to trace both GD-1 and Jhelum well, with adequate coverage over the entire stream. It is therefore still interesting to look at the metallicity mapping of the streams.

The average metallicity of Jhelum and GD-1 were around -1 with the selection described in Section 3.2 and 3.3. When looking at literature values, the metallicity of Jhelum and GD-1 are -1.77 and -2.24, respectively (Malhan et al., 2019; Awad et al., 2024). The metallicity distribution was investigated using histograms to find out where this discrepancy comes from. These histograms showed a bump around the literature metallicity and a separate second peak around metallicities of -0.3. We think this might be solar neighbourhood contamination. To select only the most metal-poor sample that is less contaminated, only stars with a metallicity lower than -0.7 and -0.75 are kept for GD-1 and Jhelum, respectively, filtering out the most metal-rich peak. This gave mean metallicities of -1.4, which is still not perfect, but these imperfections could be attributed to the lower quality metallicity estimates from the Gaia XP spectra in the VB2 catalogue (the VB1 catalogue, used in the previous section for Sagittarius has a better metallicity accuracy). The resulting RGB samples have 54 stars in both GD-1 and Jhelum.

Continuing with these filtered samples, the metallicity distribution along Jhelum and GD-1 are further examined by making plots similar to Figure 4.2. The points in the right and bottom panel of Figure 4.2 are running averages taken over multiple distance bins. As the samples do not have many RRLs and RGBs in Jhelum and GD-1, there are some metallicity plateaus and more data points than there are stars in the sample in Figure 4.7 and 4.8. This results from taking the running average across and along the stream.
The metallicities of the two streams seem to be similar on average. The metallicity of GD-1, displayed in Figure 4.7, is a bit more constant (especially when looking at the top right panel) than the metallicity of Jhelum (see Figure 4.8). This is expected when considering that GD-1 has a GC progenitor, so a more constant metallicity is typical. The metallicity along the stream (bottom panel) seems to vary a bit for GD-1, this can most likely be attributed to the quality of the XP spectra estimates for the metallicity.
The metallicity of Jhelum varies more across the stream, which might be due to the dwarf galaxy progenitor. The metallicity of the stream seems to dip around $\phi_1 \approx 7^\circ$. We can see this dip in the RGB and the RRL sample. It would be interesting to follow up on this region of Jhelum with a large sample that better traces this part of the stream.

Taking a more general perspective, it is interesting to note that the RRL and RGB metallicities are in better agreement for Jhelum and GD-1 than for Sgr. This could be because Jhelum and GD-1 are more metal-poor populations, hence the RGBs trace the same population as the RRLs.
Furthermore, the metallicities of both streams seem to dip around $\phi_2 \approx 0^\circ$, while for Sgr, we see that it peaks around this point (see Figure 4.1). It might be that this increase in metallicity in the outer regions of Jhelum and GD-1 can be attributed to more contamination. It would be interesting to follow up on this with more streams.

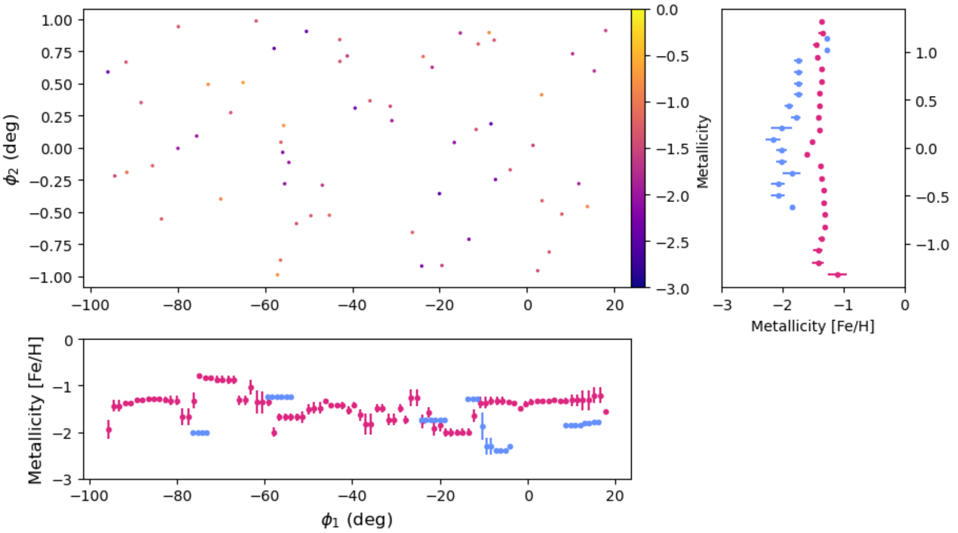

Figure 4.7: These plots illustrate the metallicity distribution of GD-1 using RRLs and RGBs. The top left plot shows stars selected to be in GD-1 as described in Section 3.3, plotted in GD-1 stream coordinates (ϕ_1, ϕ_2) and are colour-coded on [Fe/H] from Viswanathan, Byström, et al., 2024 and Li et al. (2023). The right panel plots the mean metallicity binned in stream latitude, and the bottom panel is binned in stream longitude. The pink points are the RGBs, and the blue points are the RRLs.

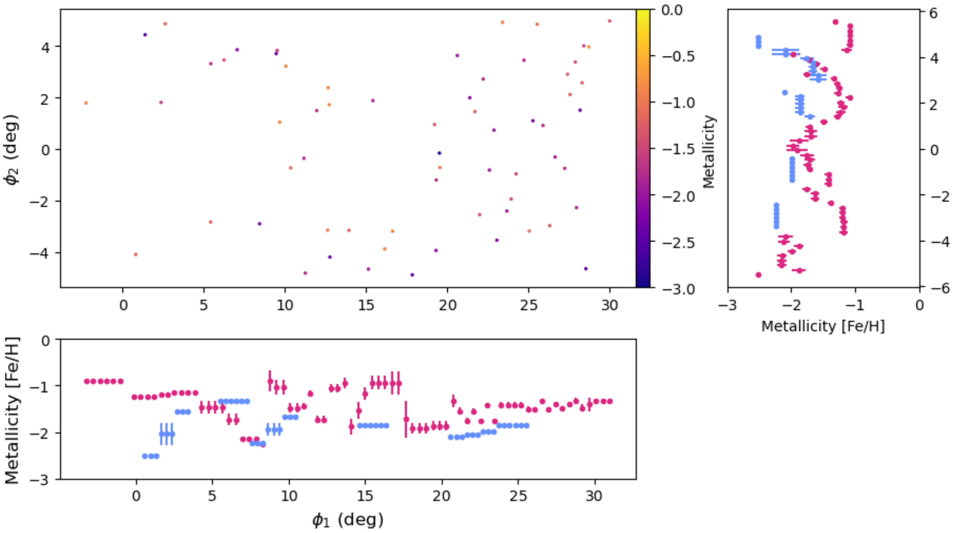

Figure 4.8: These plots illustrate the metallicity distribution of Jhelum using RRLs and RGBs. The top left plot shows stars selected to be in Jhelum as described in Section 3.2, plotted in Jhelum stream coordinates (ϕ_1, ϕ_2) and are colour-coded on [Fe/H] from Viswanathan, Byström, et al., 2024 and Li et al. (2023). The right panel plots the mean metallicity binned in stream latitude, and the bottom panel is binned in stream longitude. The pink points are the RGBs, and the blue points are the RRLs.

4.2.2 CMD and Stellar Ratios

For now, we are limited to commenting on the overall behaviour of the streams. Figure 4.9 shows the CMD of Jhelum and GD-1. In general, they look quite similar. The RRLs in the Horizontal Branch appear more clustered for Jhelum than for GD-1, which could indicate a narrower metallicity range or a more constant mass loss efficiency in the progenitor system. However, due to the low number of RRLs in both these streams, nothing conclusive can be said about this.

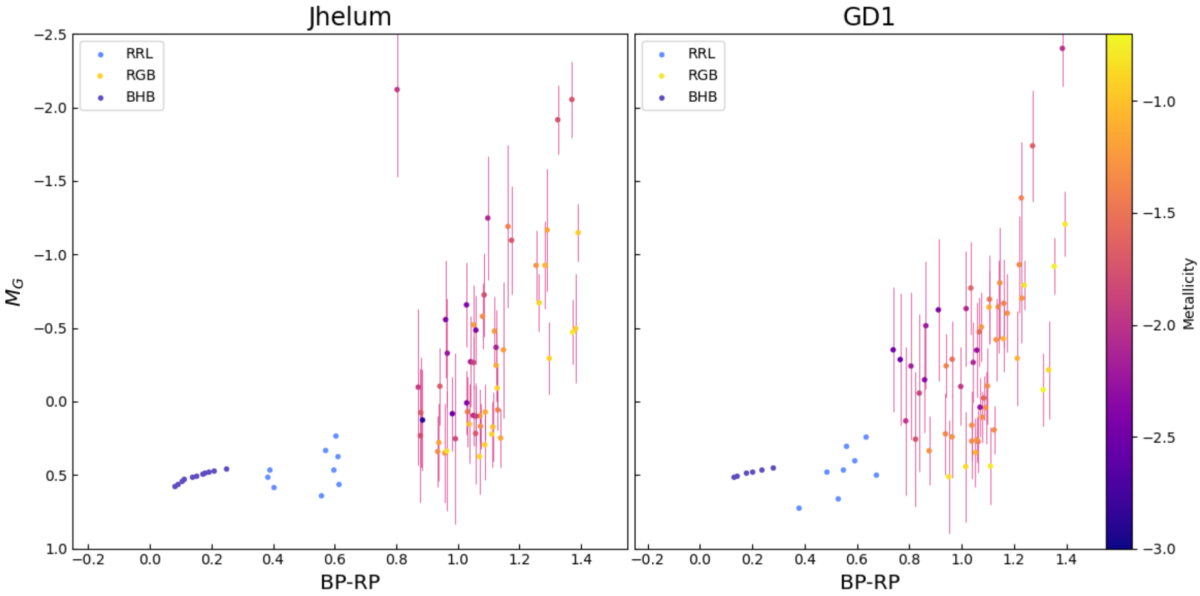

Figure 4.9: These plots display the CMDs of GD-1 and Jhelum using the G_{phot} from Viswanathan, Byström, et al., 2024. The left panel displays Jhelum, and the right panel shows GD-1. The RRLs (blue), BHBs(purple) and RGBs are plotted in this CMD. The RGBs are colour-coded based on their metallicity.

In Section 4.2.1, we already mentioned that the metallicities for the RGB stars are not the best. But as the absolute G magnitude is based on the metallicities, we tried a method to calculate the absolute G magnitude independent of metallicity. This was done by interpolating over the RRL distances along ϕ_1 and assigning distances to the RGB stars based on that. If ϕ_1 was outside the interpolation bounds, the average distance was attributed to the RGBs. Then the absolute G magnitude was calculated from the dereddened apparent G magnitude using Equation 2.2. This gave the CMD displayed in Figure 4.10. The RGB is a lot narrower, what you would expect from the RGB of a GC progenitor or dwarf galaxy and GC progenitor. Unfortunately, the RGB extends too far from what you would expect for populations of metallicity ≈ -2.2 (see Figure 1.5). Additionally, the interpolation over the distances was not very smooth, due to the small sample of RRL in both streams. This method does hence not provide reliable estimates for the absolute G magnitude for the RGB stars. Therefore, it was decided to use the estimates from VB2 based on the XP spectra, displayed in Figure 4.9.

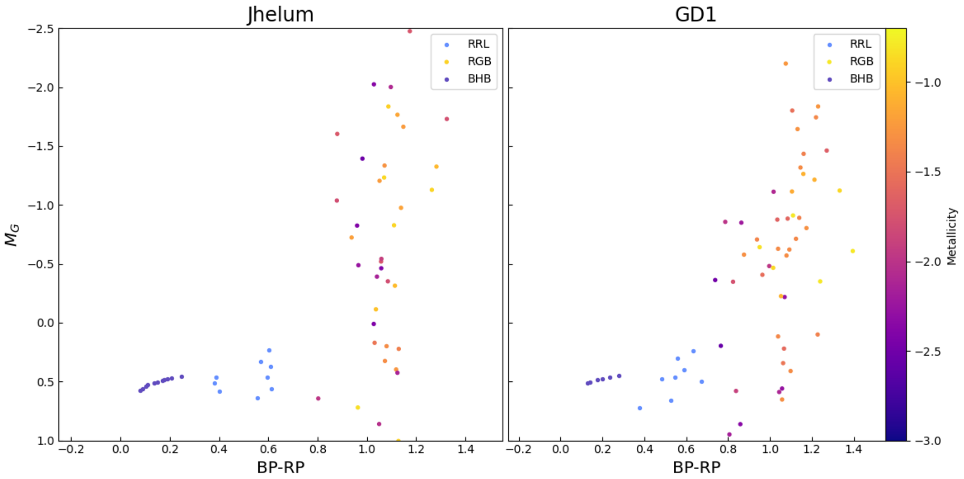

Figure 4.10: These plots display the CMDs of GD-1 and Jhelum using the M_G calculated with interpolated RRL distances and Gaia $m_{G,0}$. The left panel displays Jhelum, and the right panel shows GD-1. The RRLs (blue), BHBs(purple) and RGBs are plotted in this CMD. The RGBs are colour-coded based on their metallicity.

It is interesting to see the difference in the width of the RGB between Jhelum and GD-1. As displayed in Figure 4.9, the RGB from GD-1 seems to extend far bluer and is broader in general. This indicates that GD-1 experienced a longer period of star formation, and hence the RGB is a superposition of different isochrones of stellar populations at different ages. This is not expected from a stream with a GC progenitor. These systems have a short star formation burst, resulting in a population that has similar ages and metallicities. There is some discussion on the origin of GD-1 being a GC (Bonaca et al., 2020; Shih et al., 2022). However, Malhan et al. (2019) found a "cocoon" of stars around GD-1, indicating a slightly more complex star formation history indicative of an ex-situ structure. However, none found a chemically diverse population in GD-1, so the broad RGB Figure 4.9 is likely a result of contamination in our sample or high uncertainties on M_G.

Table 4.2 quantifies the differences between the two streams. As our RGB sample has limited accuracy in the metallicities, but detailed spectroscopic studies of stars in these streams exist (Sheffield et al., 2021; Balbinot et al., 2022; Awad et al., 2024), we will use these metallicities in the remainder of this work. We note, that for these streams the RR Lyrae metallicities that we find are quite close to the literature values (for these more metal-poor streams), although the RGB sample covers both streams better than the RRL sample. The average metallicities of the streams are very similar, especially when considering the error bars. Hence, it is not surprising that the ratios of RGB to RRL stars are similar too. It is hence impossible to draw any definitive conclusions from this, as the error bars on these values are so large and the metallicities are very similar. It is also important to note that the ratios provided are likely an upper limit. Gaia is sufficiently complete to detect most RGBs at these streams' distances, hence the RGB sample in these streams is probably a decently complete but contaminated sample by stars that are not part of Jhelum or GD-1. The ratios for RGBs may be in reality lower for pure samples of the streams.

	RRL/BHB	RGB/RRL	RGB/BHB	$[\mathrm{Fe/H}]_{\mathrm{RGB}}$	$[\mathrm{Fe/H}]_{\mathrm{RRL}}$	$[\mathrm{Fe/H}]_{\mathrm{lit}}$
Jhelum	0.82 ± 0.37	6.0 ± 2.16	4.91 ± 1.6	-1.4 ± 0.07	-1.9 ± 0.11	-1.77 ± 0.13 (1)
GD-1	1.33 ± 0.72	6.75 ± 2.6	9.0 ± 3.9	-1.4 ± 0.07	-1.8 ± 0.14	-2.24 ± 0.21 (2)

Table 4.2: The ratio between RGB and RRL stars in Jhelum and GD-1 is displayed in the above table. The uncertainties on the ratios have been calculated with Equation 4.2 and the uncertainty for the mean metallicity is the uncertainty on the mean calculated as $\sigma_{[\mathrm{Fe/H}]}/\sqrt{N}$. Sources: (1) Awad et al. (2024), (2) Malhan et al. (2019).

4.3 Relation between Stellar Population and Metallicity

Putting all the results from the above sections together yields Figure 4.11. It shows the ratios between the RGB, RRL, and BHB stars for the L22 and PS1 samples, where the points with the dashed shaded boxes are the ratios from PS1. Jhelum, unfortunately, does not have any stars in PS1 as it is not within the footprint. It is interesting to note that the ratios for the leading arm of Sgr are identical in both surveys, while fewer RRLs are detected in the trailing arm in PS1 [1].

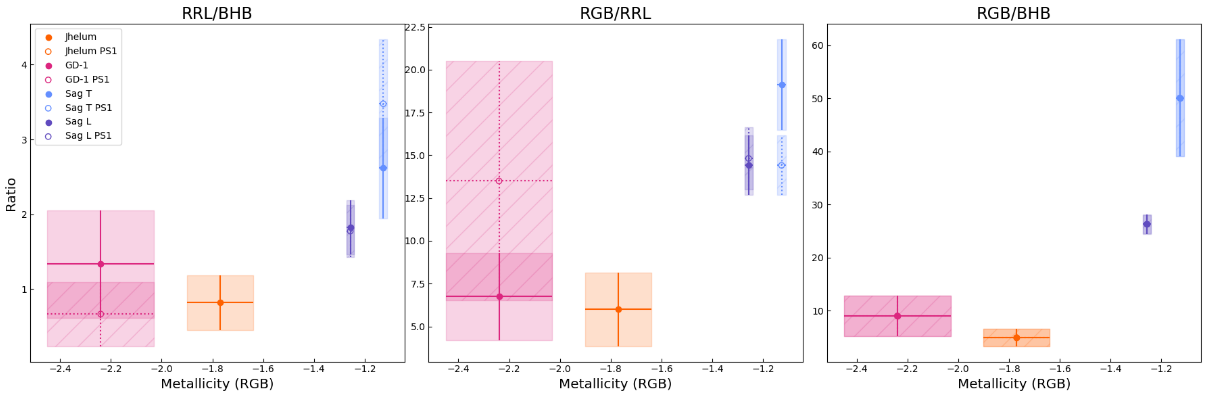

Figure 4.11: These panels display the different stellar ratios versus the metallicity of the stream or stream section. In these plots, the dashed rectangles are the data points where RRL from the PS1 data set were used, and the even rectangles are with RRL from L22. As Jhelum is not within the PS1 footprint, there is no PS1 data in that stream. The left panel shows the ratio of RRL to BHB stars, the middle is RGB to RRL stars, and the left panel displays the ratio of RGB to BHB stars.

The left panel Figure 4.11 displays the ratio of RRLs to BHBs as a function of metallicity. There appears to be a strong upward trend. The scale on which these points are distributed reveals that the values are still pretty close to one another, varying between 0.5 and 3.5. So the purity and completeness of the samples have to be high to return a trustworthy ratio within these margins. This should not be that difficult, as BHBs and RRLs are easier to find in surveys and create a relatively complete and pure sample. The ratios calculated with the L22 sample show that the ratio for Jhelum is lower even though it has a higher metallicity. We do not think that this is a significant outlier as the errors for metallicity as well as ratio are similar for GD-1 and Jhelum. Hence the hypothesis of a positive correlation is still plausible with this data.

---

[1] As the difference in ratio holds for GD-1 and Sgr trailing arm, I suspect that the exact overlap of the ratios in the leading arm is an outlier and has some explanation. Part of this explanation could be feature 3, which is relatively more present in the L22 sample than in the PS1 sample. Follow-up is necessary to determine the root cause

Examining the ratio between RGB stars and RRLs also shows a positive correlation, however, I trust this correlation a bit less. This is mainly caused by the large error bars on the ratio in GD-1, which makes a large range of slopes possible for the relation between metallicity and RGB/RRL. The discrepancy in the ratios in the trailing arm between L22 and PS1 makes determining a clear relation between these two variables more difficult.

RGB/BHB appears to be a promising candidate, with ratios varying between 10 and 55 over a metallicity range of 1 dex. This would enable you to make a metallicity estimate even if your samples are not perfectly complete and pure. However, this ratio becomes much less promising when looking at the metal-poor end, where it slightly decreases with metallicity and the ratios are very close together. This can be in part attributed to the uncertainties. Looking at the general shape of this relation, it also seems that the ratios might hit a plateau at lower metallicities. More data points of streams with varying metallicities are needed to confirm this.

Moving on to comparing the CMDs of the streams, I plotted Figures 4.5 and 4.9 together in Figure 4.13 to make comparing them a bit easier. Due to the large uncertainties on the RGB and the small sample of RGB stars in Jhelum and GD-1, we cannot see any significant differences between the three streams.

However, the HB of Jhelum and GD-1 appear to be narrower than Sgr's HB. This could mean that the spread in metallicity is larger in the leading and trailing arm of Sgr than for Jhelum and GD-1. The latter have lower metallicities, where the effect of metallicity on the RGB is smaller. This can be seen in Figure 1.5, where the lines get closer together at lower metallicities. This would make sense as streams with a GC progenitor such as GD-1 have a narrow metallicity range. Jhelum's progenitor is most likely a mix of a dwarf galaxy and a GC, with a lower mass than the Sgr progenitor, hence smaller metallicity ranges can also be suspected. This cannot be seen in Figures 4.2, 4.7 and 4.8. The metallicity plotted in those figures is the running average, which would flatten out the spread in metallicity. The metallicity distribution of Sgr, Jhelum and GD-1, displayed in Figure 4.12, actually shows that the selected patches in Sgr have a slightly larger spread in metallicity than GD-1 and Jhelum. This could explain why the HB is a bit narrower for these two streams. I would like to emphasise that the metallicities plotted for Jhelum and GD-1 are the RGB metallicities based on the Gaia XP spectra. So the metallicity distribution plotted in the right panel of Figure 4.12 might not be the most accurate picture. We trust the metallicity distributions of the left panel a lot more. These are also based on RGBs, but as they are from the VB1 sample, these metallicities are based on Pristine measurements, which return more accurate metallicity estimates. Finding more stars with metallicity information in GD-1 and Jhelum streams would help understand the distribution of their metallicities, as the sample size is also a bit too small to observe a clear distribution.

As M_G is determined from the relation stated in Deason et al. (2011), the narrowness of the BHBs might also be the projection of that relation. That would mean that the spread observed in Sgr could be due to multiple values for $g_0 - r_0$ existing for a single value of $bp_0 - rp_0$. We do not know why this is the case. It could be that this is related to the spread in metallicity, but fundamental knowledge of the HB is lacking to sufficiently explain this (Belokurov et al., 2020).

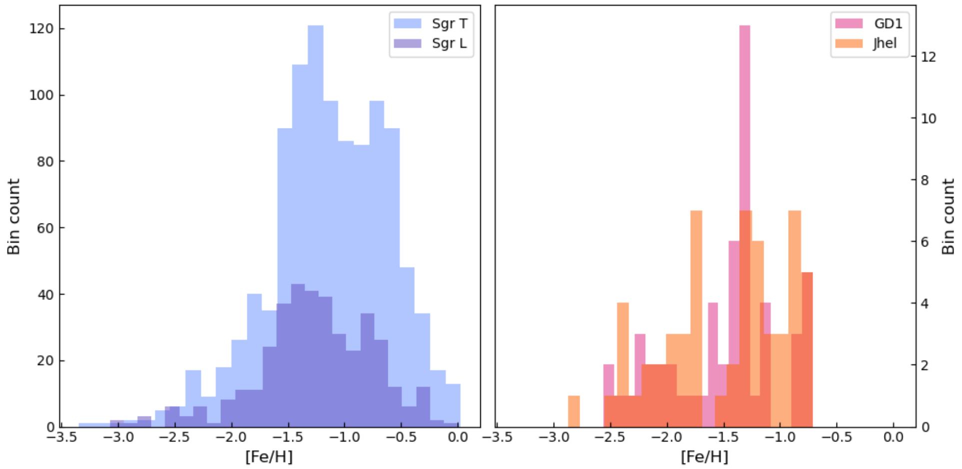

Figure 4.12: This figure displays the metallicity distribution to RGB stars in the trailing and leading arm of Sgr (left) and Jhelum and GD-1 (right).

To assess the correlation strength between the stellar ratio and metallicity, the Spearman correlation coefficient, r, is used. This coefficient is used as it has the fewest initial assumptions to evaluate the correlation. On the other hand, many correlation coefficients assume a linear relation between the variables, r only sees if the variables are increasing or decreasing. In other words, it determines the strength of the monotonic relation between the two variables, using the rank of the variables instead of the raw value. If there is a strong positive correlation, r will be 1, no correlation corresponds to a value of 0 and a strong negative correlation would give $r = -1$. The function `spearmanr` from `scipy.stats` was used to calculate r. This function takes the variables and returns r and the p-value.

Unfortunately, this function does not consider the error values of those variables when determining the correlations' strength. Therefore, a bootstrap simulation was written that takes the variables and their errors. In this simulation, r is calculated 1000 times, and the data points are drawn from a normal distribution with a standard deviation of the error values of that point. The final value of r is the median of the generated values.

These calculations were performed on the data points in Figure 4.11 to obtain the r-values in Table 4.3. These values indicate some correlation between the metallicity and the ratio between various types of stars, with the strongest correlation being between RRLs and BHBs. It shows a robust positive correlation, which might even become stronger as the error bars on our values become smaller. I think that if we can overcome some of the limitations of this work, which will be outlined in Section 5.1, these ratios could prove fruitful in estimating the metallicity of stellar populations.

	All	Gaia RRL	PS1 RRL
RRL/BHB	0.82	0.80	1.00
RGB/RRL	0.68	0.80	0.50
RGB/BHB	0.86	0.80	0.80

Table 4.3: This table displays the Pearson correlation coefficient, r, for the stellar ratios displayed in Figure 4.11.In the calculation, a bootstrap simulation accounts for the uncertainties in the data. The median value that came out of these simulations is displayed in this table. The values are calculated for the L21 sample (only looking at the even rectangles), the PS1 sample (only looking at the dashed rectangles) and both samples together.

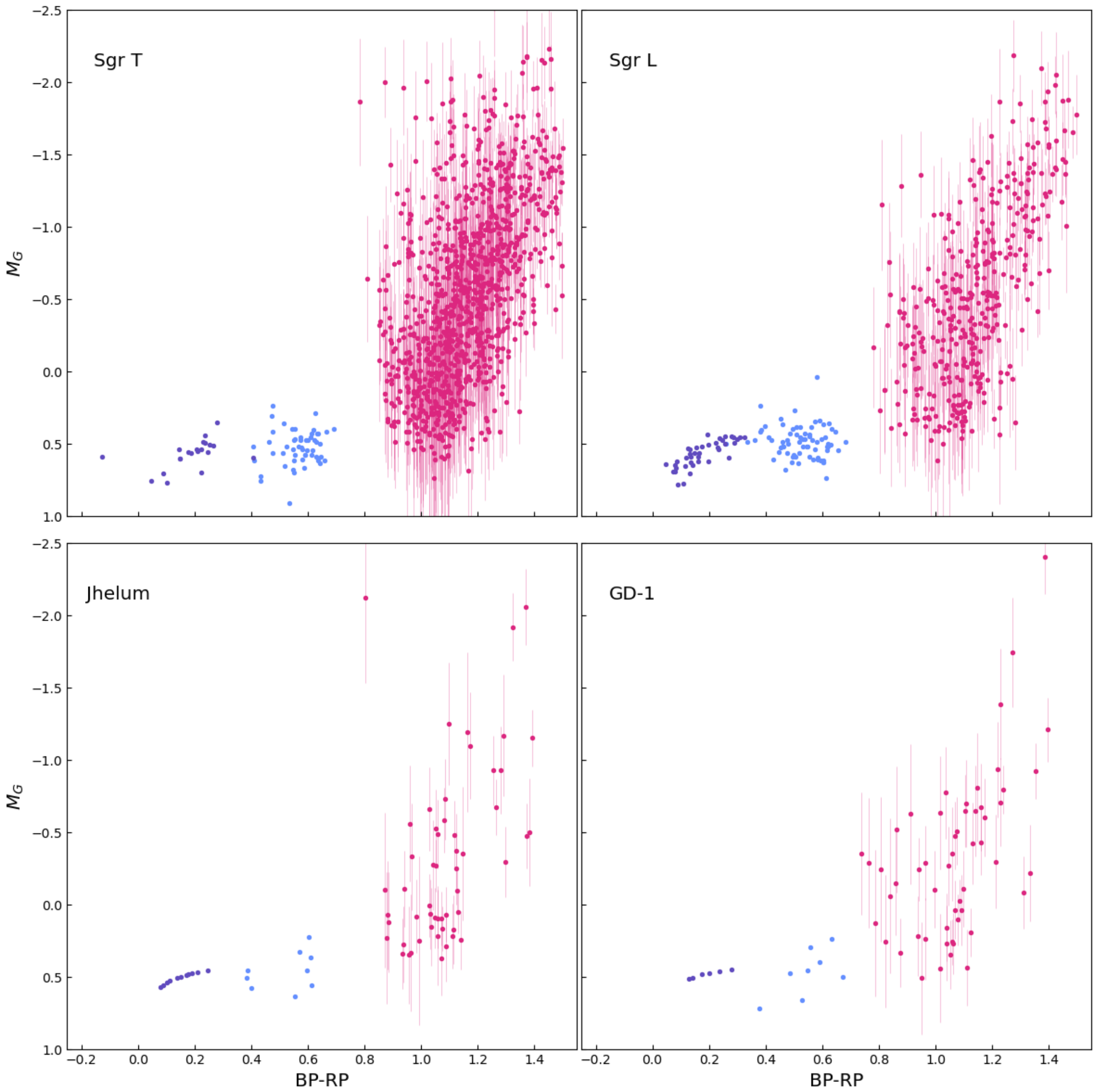

Figure 4.13: These plots display the CMDs of the trailing and leading arm of Sgr (top panels), and GD-1 and Jhelum (bottom panels). The RRLs (blue), BHBS (purple) and RGBs (pink) are plotted in this CMD.

Chapter 5

Discussion

5.1 Limitations

The study outlined in this thesis has some limitations. One of those limitations was touched upon earlier, namely the low-number statistics. For Sgr, that is not a big issue as there are a couple thousand RGB stars and a few hundred RRLs and BHBs. However, this becomes an issue for GD-1 and Jhelum, where there are around 10 BHBs and RRLs, and around 50 RGB stars. The error bars on the ratios and metallicities are rather large because the error on these values is Poissonian and thus dependent on the sample size. Even though the uncertainties on the ratios presented in this thesis are sizeable, they still make a compelling case for a strong correlation between the stellar ratio and metallicity, as expected by theory and previous work (Starkenburg et al., 2019; Binney, 2021). We see that the weakest correlation is for RGB/RRL, this is largely due to the large uncertainty for the PS1 coverage of GD-1, which allows for a large range of slopes to be fitted through the data.

Another limiting factor was the use of different surveys (in this work Gaia, Pristine, and PanSTARR1. While these surveys each gave a relatively pure and complete sample of the stars, the differences between the surveys might have induced some biases in the data. One of these biases could be caused by the different coverage and/or scanning patterns of the surveys. While we tried to keep the coverage of the compared patches similar within one survey, it is almost impossible to keep this constant throughout all three surveys. The (Gaia) scanning patterns could create a patch on the sky in which there is more or deeper data available as some scanning stripes get more observing time. In the Pristine survey, there are deeper areas where weather was better than average (and the reverse for worse weather), or where multiple observing fields overlapped. This could cause one type of star to appear more abundant in a region than in others. This is not because there are physically more stars there, but because more stars are found in that section, as the survey spent more time observing there. It is quite hard to fully correct this. However, we tried to limit this effect by selecting our regions of interest to be far removed from the magnitude limits of the surveys.
This, combined with the limiting magnitude of the surveys, results in samples that do not go out to the same distance from us. Gaia, for example, wants to make an all-sky map, which results in lower overall exposure per area on the sky, which gives a lower S/N. Other surveys are more specialised and do longer observations or are more sensitive, giving those surveys more reliable observables out to great distances.

The surveys also have different pipelines to process their raw data and make catalogues. These pipelines may have different thresholds on when to throw out data. Then there is another round of filtering the data when astronomers make more specialised catalogues out of the output data from the surveys. They can choose when they find certain observables trustworthy enough to be used in their calculations, which makes the sample less complete. These cuts are often based on the sensitivity of the instrument used, which also varies per sample in this case. The catalogue from Li et al. (2022) for instance, contains about half of the RRL in the Gaia DR3. This is largely because not all Gaia RRL have Fourier decomposition parameters, but also due to some quality cuts. This makes it difficult to understand what part of the population did not make it in this catalogue.

Lastly, there is still the issue of the completeness and purity of the samples at various distances. For the selection of some types of stars, the method gets difficult as the stars are farther away, due to a decrease in the quality of the data. This will affect how complete and pure the sample will be at those distances. If you were to apply the same method on different surveys, the completeness, and purity of the samples would still not be the same as the completeness and quality of the data drops differently for different surveys. Now considering that three different types of stars are used, and thus three different ways of identifying them in a survey, the completeness of these samples at the same distances might vary considerably.

I tried to mitigate this problem by basing the selection of the streams in this work purely on variables from Gaia, such that the influence of the individual types of stars and surveys would be as small as possible. Additionally, for our comparisons, we took care to be at a similar distance. For the Sgr leading and trailing arm comparison, we have selected patches that are as close as possible in distance. We show (in Section 4.1.2) that going further out with this comparison does have a noticeable effect on the results. Additionally, GD-1 and Jhelum are at very comparable distances (12.3 and 12 kpc). While there is a distance gap between GD-1 and Jhelum on the one hand, and the Sgr patches on the other hand, they are all selected to be reasonably close (e.g., within approximately 10 kpc). We have been selecting the streams with these criteria in mind, where the selection of coordinates and proper motions proves to be a trustworthy and accessible way of selecting streams (Hernitschek et al., 2017; Awad et al., 2024). Detailed profiles of the proper motion in the ra and dec of other streams are required if this method is to be expanded.

5.2 Constraining Stellar Evolution

As mentioned in Section 1.4, I described that the stellar evolution of low-mass stars is not fully understood. This also limits us a bit in the interpretation of our results. There is no wide consensus on the parameters that determine the position of a star on the HB, and by extent, the HB morphology. Hence, it is difficult to pin down if these different stellar ratios are caused by just the metallicity or other factors, such as the age of the population or the mass loss on the RGB.

Additionally, this analysis would probably work less well for structures that have experienced multiple episodes of bursty star formation. These structures would likely have multiple distinct populations with different metallicities, hence the ratios would likely be too general to accurately depict the stellar population and star formation history of these structures. The CMD of these structures should provide a better picture of the stellar population as you should see the multiple isochrones. If the environment that you are looking at has (had) steady star formation, the methods presented in this thesis, should be applicable. This thesis mostly researched metal-poor populations, hence we do not know how well it describes metal-rich populations as we are mostly looking at stars that typically form in metal-poor environments (BHB and RRL). It would be interesting to expand this work to metal-rich environments.

There is very little work done on combining RRLs, BHBs and/or RGBs to infer the properties of the populations. Starkenburg et al. (2019) made a qualitative comparison between the RRLs and BHBs in Sgr, where they claimed that a larger fraction of RRLs could indicate different parent stellar populations, that differ in e.g. metallicity. However, RGBs were not taken into account when making the comparison. Deason et al. (2017) was the first paper to combine RRLs, BHBs and RGBs to investigate the stellar halo of the MW. However, these stars were mainly used as tracers for the Halo, and they only remarked on how the proper motions of these stars agreed. They did not make any implications for what having more or less of a type of star could imply for the stellar population. Other work mainly focussed on one specific type of star to learn about the stellar evolution and properties of the population. These analyses often remained qualitative, so it is difficult to compare our results to the literature. Even though, these uncertainties in stellar evolution pathways limit the interpretation of our results, more detailed studies of well-understood, close-by systems, like the one presented in this thesis, could help constrain stellar evolution. If more quantitative studies were published on close-by structures, it could provide a wider scientific basis to interpret our results, while simultaneously improving our understanding of stellar evolution pathways.

5.3 Future Prospects

Future work could expand on the work done in this thesis. One of the biggest limiting factors was the footprint of the Pristine survey in the study of the Sgr stream, which put a constraint on which parts of Sgr could be studied with RGB stars and BHBs. Luckily, a new programme has recently been accepted, which aims to expand on the Pristine footprint, making it possible to study the full extent of bigger structures in the Halo but also the smaller streams that are currently left out of the footprint like Jhelum.

With this work we cover a metallicity range from -2.24 to -1.1, where we have data on the relatively metal-rich Sgr stream on the one hand and the relatively metal-poor GD-1 and Jhelum streams on the other hand, but no intermediate metallicity structures. Future work could benefit by bridging the metallicity gap between GD-1 and Jhelum, and Sgr or by looking at even metal-poorer structures. Ibata et al. (2024) presented a list of 87 streams with their average metallicity and members found in Gaia DR3. The metallicity range could be extended to the metal-poor end using streams like C-19 with a metallicity of -3.58 and 46 members, and Gaia-12 with a metallicity of -3.28 and 46 members. To bridge the gap between the data in this thesis, you could include streams like NGC 288, with 173 members or Indus with 1021 members. I advise any future researcher on this topic to look through Table 3 of Ibata et al. (2024) to get a good overview of the streams with average metallicity and members found.

Many limitations in this work could be overcome in the next couple of years with the new data releases. The fourth Gaia release would greatly help with limiting the differences between the data samples. This data release would go much deeper than DR3 and would be able to trace the Sgr stream in all our stellar types. This could mean that the samples do not have to come from different surveys, which would severely limit the different drops in completeness between the samples. It would also provide identical scanning patterns across all our samples and increase the sample sizes of our data.

As the ratio of RRLs vs BHBs proves to be the most promising avenue for establishing a quick view of the HB and thus an independent view of stellar populations, it would be worthwhile to create a BHB catalogue using PanSTARRS1. This could be done by using the z-band from this survey. This would not select the BHBs using the Balmer lines but would be sensitive to the Paschen lines instead (Titulaer, 2021). Unfortunately, PanSTARRS1 does not have a u-band filter so it is not possible to make an RGB star catalogue using only this survey. However, this can be mitigated by u-band data from CFIS in the future (Errani et al., 2024).

As new and exciting spectroscopic surveys are coming up on the horizon, our ability to identify and collect large numbers of these types of stars in other galaxies grows. The stellar ratios could be used to infer the metallicity of faraway galaxies, if more research were to be done to more concretely establish the relation between stellar ratios, such as RRL/BHB, and metallicity, age and/or mass-loss. This could provide an alternative to spectroscopy to establish the properties of the host galaxy when spectroscopy is too expensive or not possible. At the same time, determining the stellar ratios of more structures in the Universe with known properties could help to understand stellar evolution onto and on the BHB better.

Of course, more work needs to be done on this topic before we can extend it to extragalactic environments. However, with new data releases on the horizon, this method could prove valuable in studying galaxies at higher redshift.

Chapter 6

Conclusion and Future Prospects

This thesis aims to see what we can learn about stellar streams and their progenitor systems by combining RGBs, RRLs, and BHBs. To this end, I have examined the relationship between metallicity and stellar ratios and compared the shapes and features of the CMDs to infer more about the underlying stellar population.

As a first step, catalogues had to be created of RGBs, RRLs and BHBs. In this work, we have taken these catalogues from external sources (Li et al. (2022), Viswanathan, Byström, et al., 2024 and private communications) and they were carefully tested for caveats. These findings can be summarized as follows:

- For the purpose of determining distances to the RGB stars, T_{eff} works better than colour (this conclusion was subsequently adopted in Viswanathan et al. (2024))
- No major differences were found between the RRL catalogue of PS1 and Gaia in the apparent magnitude ranges and sky area where they overlap. The main advantage Gaia has over PS1 is that it is all-sky. PS1 on the other hand is deeper.
- When looking at the magnitude limit of the BHB sample, care has to be taken to remove quasars that move into this sample due to their very large uncertainties.

To learn more about the metallicity distribution of our streams, the methodology of Cunningham et al. (2024) investigating the metallicity distribution of the Sgr with RGBs was followed. We combined the RRL and RGB samples, as these samples had metallicity information. The values for the metallicities from RGB stars agreed with the values found by Cunningham et al. (2024) and that the shape of the metallicity distribution traced by RRLs followed the shape of the RGB stars in this paper too. However, the average metallicity of the RRL was about 0.5 dex lower across the Sgr stream compared to the RGB metallicities. RRL typically trace metal-poor stars, which could result in a lower average metallicity. Metallicities from RRL show qualitative results that are very comparable with RGB stars in the Sgr stream. However, we note that the current RRL catalogues cannot be used to trace the average metallicity, as they only trace the metal-poor populations well. It is still interesting to see that the shape of the distribution agreed so well between the RRL and RGB samples. Figure 4.2 also showed that the metallicity was higher in the trailing arm than in the leading arm. We therefore expect that part of the stream to have relatively more RGB stars as stars spent more time on the RGB if they have a higher metallicity.

Two patches were selected to investigate this further, one in the leading arm and one in the trailing. In the first selection of the trailing arm, the ratios between the leading and trailing arm differed much more than expected, given the difference in metallicity. After investigating other factors that might influence the ratios, it became clear that the selected parches were not at the same distance, hence the ratios traced the difference in completeness between the compared samples rather than a difference in stellar population. Hence, a different patch for the leading arm was selected that better matched the distance of the patch in the trailing arm. When this selection was applied, the stellar ratios were a lot closer together than before.

Even though the values were closer, an offset remained between the two ratios. The ratio between RRLs and BHBs stays constant between the two patches given the uncertainty of the ratios. The ratios between RGBs and RRLs, and RGBs and BHBs both increased with increasing metallicity. The ratios were different within 1σ.

Lastly, the CMDs of the two different parts of Sgr were compared. The HB branch of the leading arm seems to be more populated compared to the RGB, which would indicate that the leading arm is more metal-poor or had more efficient mass loss when the stars evolved off the RGB. Furthermore, there is a gap in the HB for the trailing arm. This seems to be a lack of bluer RRLs, as the BHBs extend equally far red as in the leading arm.

A known substructure in the Sgr stream called "Feature 3" was present in all our samples and, within uncertainties, equally well represented in all samples and stellar types. The lowest ratio of stars in feature 3 to stars in the main stream was found for the RGB stars. This could be explained by a larger uncertainty in the distances for RGB stars and a lower completeness at large distances. Comparing the observational ratios with the simulation ratios tells a completely different story. Feature 3 is severely underpopulated in the simulations compared to the observations. This could be due to an incorrect velocity distribution assigned to the Sgr progenitor in the simulation, or small-scale interactions and inhomogeneities that are hard to account for in an N-body simulation.

Furthermore, we also investigated Jhelum and GD-1. There were very few RRLs and BHBs found in our samples in these streams, hence they were considered in their entirety rather than selecting patches. RGB stars traced these streams a bit better and could reveal more about their metallicity distribution. The metallicity of GD-1 and Jhelum stayed relatively constant, with the exception around $\phi_1 \approx 6^\circ$ in Jhelum where it drops. It would be interesting to follow up on this with a sample that maps these streams a bit better, such as MS stars (Viswanathan, Byström, et al., 2024).

The CMD of these streams hints at GD-1 having a more continuous star-formation history, due to a broader RGB. However, this broader RGB is most likely caused by contamination in the selection of GD-1. This stream is thought to have a GC progenitor, and hence a short period of star formation. Hence, uncertainties on the RGB are too big to make any claims on the nature of the progenitor of GD-1. Furthermore, the HB of Jhelum is more clustered than for GD-1, indicating a narrower metallicity range or more constant mass loss efficiency for Jhelum.

Just looking at Jhelum and GD-1 does not reveal much about the relation between stellar ratios and metallicity. The sample of RRLs and BHBs is too small to make any statistically significant claim about this. Combining it with more streams or increasing the sample sizes in these streams should help to overcome this.

By combining these streams, we can comment on the relation between the stellar populations and metallicity. In general, there seems to be some correlation between the metallicity and the ratios plotted in Figure 4.11. However, this correlation is not equally strong for all ratios. The strongest correlation was for RRLs to BHBs, which displayed a positive correlation between the ratio and the metallicity. This means that relatively more RRL would translate to a higher metallicity. A slightly weaker correlation was found for the ratio between RGBs and BHBs, which also gave a positive correlation. Lastly, the weakest correlation was for RGB/RRL vs metallicity, with an average r of 0.66. These correlation coefficients, from decently small samples, tell us that there is probably a strong correlation between the stellar ratios and the metallicity of streams. If this work is expanded upon by the inclusion of more streams at varying metallicities, their relation could be more accurately determined and this work could perhaps be expanded to other galaxies.

Chapter 7

Acknowledgements

First and foremost, I would like to thank my supervisors, Else Starkenburg and Manuel Bayer. I could not have done that without their guidance and feedback throughout this project. I would like to thank them for their support, insight, and flexibility. I appreciated the balance between guidance and letting me do my thing during this thesis, which allowed me to follow my interests and take this work in directions I never expected it to go. I would like to thank Manuel and Annemarijn Zwerver for the work they have done to make the BHB catalogues used in this work.

I would also like to thank Akshara Viswanathan and Amanda Byström, for including me in their paper. It allowed me to work with a scientific team, and it inspired and motivated me to perfect my own work and delve deeper into the topics discussed in the paper.

I would also like to thank Else's and Amina Helmi's research groups, for providing a stimulating research environment. At first, I felt a bit intimidated by the academic community, but they provided a safe space where I could ask all the (stupid) questions I had, and discuss papers and results.

I would also like to thank Martin Vogelaar, for helping me out with any computer problems I had, especially at the beginning of the project. I had some problems running `galstreams` on the local host and he always managed to help me quickly without sounding too annoyed when I came knocking on his door for the 11th time.

I would be remiss in not mentioning the use of AI in this thesis. It helped me greatly in summarizing papers when I couldn't focus on reading them myself. This allowed me to still get a good idea of the key points of a paper so that I could revisit it at a later time when I had the brainpower again to focus on papers.

Lastly, I would also like to thank my friends for supporting and encouraging me throughout this experience and allowing me to take it a bit easier when I took too much upon myself. They helped me stay motivated and gave me plenty to look forward to after it was done. They gave me a family away from home during my studies and motivated me to reach new heights.

Bibliography

Andrae R., Rix H.-W., Chandra V., 2023, The Astrophysical Journal Supplement Series, 267, 8

Athanassoula E., 2002, arXiv preprint astro-ph/0209438

Awad P., et al., 2024, Astronomy & Astrophysics, 683, A14

Balbinot E., Cabrera-Ziri I., Lardo C., 2022, Monthly Notices of the Royal Astronomical Society, 515, 5802

Barbuy B., Chiappini C., Gerhard O., 2018, Annual Review of Astronomy and Astrophysics, 56, 223

Belokurov V., et al., 2006, The Astrophysical Journal, 642, L137

Belokurov V., et al., 2014, Monthly Notices of the Royal Astronomical Society, 437, 116

Belokurov V., et al., 2020, Monthly Notices of the Royal Astronomical Society, 496, 1922

Bencivenni D., Caputo F., Manteiga M., Quarta M., 1991, Astrophysical Journal, Part 1 (ISSN 0004-637X), vol. 380, Oct. 20, 1991, p. 484-494. Research supported by CNPq and CNR., 380, 484

Bensby T., Feltzing S., Oey M., 2014, Astronomy & Astrophysics, 562, A71

Binney J., 2021, Galactic astronomy. Princeton University Press

Bland-Hawthorn J., Gerhard O., 2016, Annual Review of Astronomy and Astrophysics, 54, 529

Bonaca A., Geha M., Küpper A. H., Diemand J., Johnston K. V., Hogg D. W., 2014, The Astrophysical Journal, 795, 94

Bonaca A., Conroy C., Wetzel A., Hopkins P. F., Kereš D., 2017, The Astrophysical Journal, 845, 101

Bonaca A., Conroy C., Price-Whelan A. M., Hogg D. W., 2019, The Astrophysical Journal Letters, 881, L37

Bonaca A., et al., 2020, The Astrophysical Journal Letters, 892, L37

Bonaca A., et al., 2021, The Astrophysical Journal Letters, 909, L26

Carroll B. W., Ostlie D. A., 2017, An introduction to modern astrophysics. Cambridge University Press

Catelan M., 2007, arXiv preprint astro-ph/0703724

Catelan M., 2009, Astrophysics and Space Science, 320, 261

Chaboyer B., 1996, Nuclear Physics B-Proceedings Supplements, 51, 10

Clementini G., et al., 2023, Astronomy & Astrophysics, 674, A18

Cunningham E. C., Hunt J. A., Price-Whelan A. M., Johnston K. V., Ness M. K., Lu Y. L., Escala I., Stelea I. A., 2024, The Astrophysical Journal, 963, 95

Deason A., Belokurov V., Evans N., 2011, Monthly Notices of the Royal Astronomical Society, 416, 2903

Deason A. J., Belokurov V., Koposov S. E., Gómez F. A., Grand R. J., Marinacci F., Pakmor R., 2017, Monthly Notices of the Royal Astronomical Society, 470, 1259

Demers S., Wehlau A., 1977, Astronomical Journal, Vol. 82, p. 620-625, 82, 620

Errani R., Navarro J. F., Smith S. E., McConnachie A. W., 2024, The Astrophysical Journal, 965, 20

Fabrizio M., et al., 2019, The Astrophysical Journal, 882, 169

Fabrizio M., et al., 2021, The Astrophysical Journal, 919, 118

Fardal M. A., van der Marel R. P., Law D. R., Sohn S. T., Sesar B., Hernitschek N., Rix H.-W., 2019, Monthly Notices of the Royal Astronomical Society, 483, 4724

Fellhauer M., et al., 2006, The Astrophysical Journal, 651, 167

Fiorentino G., et al., 2022, Memorie della Societa Astronomica Italiana, 93, 47

Fuhrmann K., 2011, Monthly Notices of the Royal Astronomical Society, 414, 2893

Fukushima T., et al., 2018, Publications of the Astronomical Society of Japan, 70, 69

Grand R. J., et al., 2017, Monthly Notices of the Royal Astronomical Society, 467, 179

Gratton R. G., Carretta E., Bragaglia A., Lucatello S., D'Orazi V., 2010, Astronomy & Astrophysics, 517, A81

Grillmair C. J., Dionatos O., 2006, The Astrophysical Journal, 643, L17

Grimozzi S. E., Font A. S., De Rossi M. E., 2024, Monthly Notices of the Royal Astronomical Society, 530, 95

Haywood M., Di Matteo P., Lehnert M., Snaith O., Khoperskov S., Gómez A., 2018, The Astrophysical Journal, 863, 113

Helmi A., 2004, The Astrophysical Journal, 610, L97

Helmi A., 2020, Annual Review of Astronomy and Astrophysics, 58, 205

Helmi A., White S. D., 1999, Monthly Notices of the Royal Astronomical Society, 307, 495

Helmi A., White S. D., De Zeeuw P. T., Zhao H., 1999, Nature, 402, 53

Hernitschek N., et al., 2017, The Astrophysical Journal, 850, 96

Heyl J., Kalirai J., Richer H. B., Marigo P., Antolini E., Goldsbury R., Parada J., 2015, The Astrophysical Journal, 810, 127

Ibata R. A., Gilmore G., Irwin M., 1994, Nature, 370, 194

Ibata R., et al., 2024, The Astrophysical Journal, 967, 89

Ji A. P., et al., 2020, The Astronomical Journal, 160, 181

Johnston K. V., 1998, The Astrophysical Journal, 495, 297

Johnston K. V., Law D. R., Majewski S. R., 2005, The Astrophysical Journal, 619, 800

Karttunen H., Kröger P., Oja H., Poutanen M., Donner K. J., 2007, Fundamental astronomy. Springer

Keane M., Olszewski E., Suntzeff N., Saha A., 1993, in American Astronomical Society, 182nd AAS Meeting, id. 32.03; Bulletin of the American Astronomical Society, Vol. 25, p. 844. p. 844

Koposov S. E., Rix H.-W., Hogg D. W., 2010, The Astrophysical Journal, 712, 260

Koposov S. E., et al., 2012, The Astrophysical Journal, 750, 80

Laporte C. F., Johnston K. V., Gómez F. A., Garavito-Camargo N., Besla G., 2018, Monthly Notices of the Royal Astronomical Society, 481, 286

Law D. R., Majewski S. R., 2010, The Astrophysical Journal, 714, 229

LeBlanc F., 2011, An introduction to stellar astrophysics. John Wiley & Sons

Lee Y.-W., Demarque P., Zinn R., 1994, The Astrophysical Journal, Part 1 (ISSN 0004-637X), vol. 423, no. 1, p. 248-265, 423, 248

Li T. S., et al., 2022, The Astrophysical Journal, 928, 30

Li X.-Y., Huang Y., Liu G.-C., Beers T. C., Zhang H.-W., 2023, The Astrophysical Journal, 944, 88

Li L.-J., Qian S.-B., Zhu L.-Y., Shi X.-D., Liao W.-P., 2024, arXiv preprint arXiv:2404.00911

Licquia T. C., Newman J. A., 2015, The Astrophysical Journal, 806, 96

Limberg G., et al., 2023, The Astrophysical Journal, 946, 66

Longmore A., Fernley J., Jameson R., 1986, Monthly Notices of the Royal Astronomical Society, 220, 279

Luongo E., Ripepi V., Marconi M., Prudil Z., Rejkuba M., Clementini G., Longo G., 2024, Astronomy & Astrophysics, 690, L17

Malhan K., Ibata R. A., Carlberg R. G., Valluri M., Freese K., 2019, The Astrophysical Journal, 881, 106

Masseron T., Gilmore G., 2015, Monthly Notices of the Royal Astronomical Society, 453, 1855

McDonald I., Zijlstra A., 2015, Monthly Notices of the Royal Astronomical Society, 448, 502

McWilliam A., 1997, Annual Review of Astronomy and Astrophysics, 35, 503

Montegriffo P., et al., 2023, Astronomy & Astrophysics, 674, A3

Morrison H. L., et al., 2009, The Astrophysical Journal, 694, 130

Naidu R. P., Conroy C., Bonaca A., Johnson B. D., Ting Y.-S., Caldwell N., Zaritsky D., Cargile P. A., 2020, The Astrophysical Journal, 901, 48

Naidu R. P., et al., 2022, arXiv preprint arXiv:2204.09057

Narloch W., et al., 2024, Astronomy & Astrophysics, 689, A138

Nataf D. M., Cassisi S., Casagrande L., Yuan W., Riess A. G., 2021, The Astrophysical Journal, 910, 121

Newberg H. J., 2005, New Astronomy Reviews, 49, 447

Ngan W., Carlberg R. G., Bozek B., Wyse R. F., Szalay A. S., Madau P., 2016, The Astrophysical Journal, 818, 194

Niederste-Ostholt M., Belokurov V., Evans N., 2012, Monthly Notices of the Royal Astronomical Society, 422, 207

Oosterhoff P. T., 1939, The Observatory, Vol. 62, p. 104-109 (1939), 62, 104

Pearson S., Price-Whelan A. M., Johnston K. V., 2017, Nature Astronomy, 1, 633

Piotto G., et al., 2007, The Astrophysical Journal, 661, L53

Price-Whelan A. M., Bonaca A., 2018, The Astrophysical Journal Letters, 863, L20

Prudil Z., Arellano Ferro A., 2024, Monthly Notices of the Royal Astronomical Society, 534, 3654

Ramos P., et al., 2022, Astronomy & Astrophysics, 666, A64

Renzini A., Fusi Pecci F., 1988, IN: Annual review of astronomy and astrophysics. Volume 26 (A89-14601 03-90). Palo Alto, CA, Annual Reviews, Inc., 1988, p. 199-244. Research supported by the Ministero della Pubblica Istruzione and CNR., 26, 199

Ruiz-Dern L., Babusiaux C., Arenou F., Turon C., Lallement R., 2018, Astronomy & Astrophysics, 609, A116

Salaris M., Cassisi S., 2005, Evolution of stars and stellar populations. John Wiley & Sons

Schlegel D. J., Finkbeiner D. P., Davis M., 1998, The Astrophysical Journal, 500, 525

Schröder K.-P., Cuntz M., 2005, The Astrophysical Journal, 630, L73

Sesar B., et al., 2017a, The Astronomical Journal, 153, 204

Sesar B., Hernitschek N., Dierickx M. I., Fardal M. A., Rix H.-W., 2017b, The Astrophysical Journal Letters, 844, L4

Sheffield A. A., et al., 2021, The Astrophysical Journal, 913, 39

Shih D., Buckley M. R., Necib L., Tamanas J., 2022, Monthly Notices of the Royal Astronomical Society, 509, 5992

Shipp N., et al., 2018, The Astrophysical Journal, 862, 114

Soszynski I., et al., 2011, arXiv preprint arXiv:1105.6126

Sparke L. S., Gallagher J. S., 2000, Galaxies in the universe: an introduction. Cambridge University Press

Starkenburg E., et al., 2019, Monthly Notices of the Royal Astronomical Society, 490, 5757

Titulaer L., 2021, Master's thesis, University of Groningen

Tolstoy E., Hill V., Tosi M., 2009, Annual Review of Astronomy and Astrophysics, 47, 371

Van Albada T., Baker N., 1973, Astrophysical Journal, Vol. 185, pp. 477-498 (1973), 185, 477

Vasiliev E., Belokurov V., Erkal D., 2021, Monthly Notices of the Royal Astronomical Society, 501, 2279

Vera-Ciro C., Helmi A., 2013, The Astrophysical Journal Letters, 773, L4

Viswanathan A., et al., 2024, arXiv preprint arXiv:2408.17250

Webb J. J., Bovy J., 2019, Monthly Notices of the Royal Astronomical Society, 485, 5929

Woudenberg H. C., Koop O., Balbinot E., Helmi A., 2023, Astronomy & Astrophysics, 669, A102

Xue X.-X., et al., 2011, The Astrophysical Journal, 738, 79

Zgirski B., et al., 2023, The Astrophysical Journal, 951, 114

de Zeeuw T., Norris J., 1999, Publications of the Astronomical Society of the Pacific, 111, 653

Appendix A

Code

In [ ]:

```
from astropy.table import QTable, vstack
import numpy as np
from numpy.random import normal
import pandas as pd
import matplotlib.pyplot as plt
import matplotlib as mpl
from matplotlib.colors import LinearSegmentedColormap
import vaex as vaex
from scipy.interpolate import interp1d
from scipy.stats import pearsonr, spearmanr, norm
from astropy import units as u
import gala.coordinates as gc
import astropy.coordinates as coord
```

Basic Calculations

In [ ]:

```
colors=['#ffb000', '#fe6100', '#dc267f', '#648fff', '#604bbf']

def abs_mag(g, r):
    """calculate abs G mag for BHB from Deason et al 2011"""
    u = g-r
    M = 0.434 - 0.169*u + 2.319*u**2 + 20.449*u**3 + 94.517*u**4
    return M

def abs_mag_bs(g, r, FeH=-1):
    """calculate abs G mag for BS from Deason et al 2011"""
    u = g-r
    M = 2.2 + 4.557*u - 0.45*FeH
    return M

def dist(M, m):
    """Standard distance calculations"""
    return 10**((m-M+5)/5)/1e3
def mag(d, m):
    return m - 5*np.log10(1e3*d) +5

def run_ave(data, quan, quan2='Lambda', sim=True):
    xmin = min(data[quan2])
    xmax = max(data[quan2])
    x = np.linspace(xmin-5, xmax+5, 96)
    err = []
    stdu = []
    stdl = []
    mean = []
    for i in range(len(x)-6):
        inbetween = data[(data[quan2]>x[i]) & (data[quan2]<x[i+6])]
        if len(inbetween) == 0:
            mean.append(np.nan)
            stdu.append(np.nan)
            stdl.append(np.nan)
            err.append(np.nan)
        else:
            #median behaviour
            mean.append(np.median(inbetween[quan]))
            #selecting 90% inbetween (ordering low to high, cutting <5% and >95%)
            stdu.append(sorted(inbetween[quan])[int((len(inbetween)+1)/100*95-1)])
            stdl.append(sorted(inbetween[quan])[int((len(inbetween)+1)/100*5-1)])
            err.append(np.std(inbetween[quan])/len(inbetween[quan]))
    if sim==True:
        return stdl, mean, stdu, x[3:-3]
```

```
    else:
        return mean, err, x[3:-3]


def d_M(dat):
    d = dat['Dist']*1e3
    dd = dat['phot_dist_errs']
    return abs(5/(d*np.log(10)) * dd)

def bootstrap_spearman_with_errors(x, y, x_errors, y_errors, n_bootstrap=1000):
    """
    Calculates Spearman's rank correlation coefficient considering errors
    using bootstrapping.
    """

    bootstrap_correlations = []

    # Perform bootstrapping
    for _ in range(n_bootstrap):
        # Generate random samples within the error bounds (Gaussian distribution)
        x_sample = np.random.normal(x, x_errors)
        y_sample = np.random.normal(y, y_errors)

        # Calculate Spearman rank correlation for this bootstrap sample
        corr, p = spearmanr(x_sample, y_sample)
        bootstrap_correlations.append(corr)

    # Return the mean of the bootstrapped correlations
    return np.median(bootstrap_correlations), np.std(bootstrap_correlations)

def new_G(r_dat, dat):
    """interpolate over RRL distances"""
    f = interp1d(r_dat['phi1'], r_dat['Dist'])

    G = []
    #define interpolation bounds of f
    minp = min(r_dat['phi1'])
    maxp = max(r_dat['phi1'])
    #median distance if value is outside integration bounds
    md = np.median(r_dat['Dist'])

    for i in range(len(dat['phi1'])):
        #if data points is within the integration bounds, it gets its distance form
        #else it will get the median distance assigned
        if dat['phi1'][i]>minp and dat['phi1'][i]<maxp:
            d = f(dat['phi1'][i])
        else:
            d = md
        #calculate distance with standard equation
        G.append(mag(d, dat['G_0'][i]))
    return G
```

Selecting Sag

In [ ]:

```
def l_sag(RA, DEC):
    """convert to latitude with Sag centre at centre"""
    ra = np.radians(RA)
    dec = np.radians(DEC)
    y = (-0.93595354*np.cos(ra)*np.cos(dec) - 0.31910658*np.sin(ra)*np.cos(dec)
     + 0.14886895*np.sin(dec))
    x = (0.21215555*np.cos(ra)*np.cos(dec) - 0.84846291*np.sin(ra)*np.cos(dec)
     - 0.48487186*np.sin(dec))
```

```
    L = np.arctan2(y,x)
    return np.degrees(L)

def b_sag(ra, dec):
    """convert to longitude with Sag centre at centre"""
    ra = np.radians(ra)
    dec = np.radians(dec)
    B = np.arcsin(0.28103559*np.cos(ra)*np.cos(dec) - 0.42223415*np.sin(ra)*np.cos(d
                  +  0.86182209*np.sin(dec))
    return -np.degrees(B)

def select_sag(dat):
    #defining upper and lower acceptable boundry for pm for rrl
    dat['eu_pmra'] = stdu_pmra(dat['Lambda'])
    dat['eu_pmdec'] = stdu_pmdec(dat['Lambda'])
    dat['el_pmra'] = stdl_pmra(dat['Lambda'])
    dat['el_pmdec'] = stdl_pmdec(dat['Lambda'])

    #making cuts on pm for rrl (including error on pm of data)
    dat_sel = dat[(dat['pmra']<dat['eu_pmra']+dat['pmra_error']) &
                  (dat['pmra']>dat['el_pmra']-dat['pmra_error']) &
                  (dat['pmdec']<dat['eu_pmdec']+dat['pmdec_error']) &
                  (dat['pmdec']>dat['el_pmdec']-dat['pmdec_error']) &
                  (dat['pmra_error']<0.6) & (dat['pmdec_error']<0.6) &
                  (dat['Plx']<0.05) &
                  (dat['Lambda']<150) & (abs(dat['Beta'])<20)]
    if str(dat)==str(Ak_sam) or str(dat)==str(Ak_sam_gaia):
        #foreground clean up and selecting tip of rgb
        dat_sel = dat_sel[(dat_sel['logg_xgboost']<2.3)]
    return dat_sel
```

Selecting Jhelum

In [ ]:

```
def jhel_coords(data):
    """Convert the coordinate system to spherical coordinates centred around Jhelum
    to retriece phi1, phi2 and the propermotion with respect to those coordinates as
    are at a distance of 12 kpc (Awad 20214)"""
    dat = data.copy()
    c = coord.SkyCoord(ra = dat['ra']*u.deg,
                       dec=dat['dec']*u.deg,
                       pm_ra_cosdec = dat['pmra']*u.mas/u.yr,
                       pm_dec = dat['pmdec']*u.mas/u.yr,
                       distance = 13 *u.kpc)
    jhel = c.transform_to(gc.JhelumBonaca19())
    dat['phi1'] = jhel.phi1.value
    dat['phi2'] = jhel.phi2.value
    dat['pm_phi1'] = jhel.pm_phi1_cosphi2.value
    dat['pm_phi2'] = jhel.pm_phi2.value
    return dat

def select_jhel(dat):
    """Selection by P. Awad 2024 on phi1, phi2 and their respective proper motions""
    dat_sel = dat[(dat['phi1'].value>-5) & (dat['phi1'].value<30) &
                  (abs(dat['phi2'].value)<5) &
                  (dat['pm_phi1'].value>-8) & (dat['pm_phi1'].value<-4) &
                  (abs(dat['pm_phi2'].value)<2)]
    return dat_sel
```

Selecting GD1

In [ ]:

```
def gd1_coords(data):
    """Convert the coordinate system to spherical coordinates centred around GD1 (Ko
    to retriece phi1, phi2 and the propermotion with respect to those coordinates as
    are at a distance of 12.26 kpc (Koposov 2010)"""
    dat = data.copy()
    c = coord.SkyCoord(ra = dat['ra']*u.deg,
                       dec=dat['dec']*u.deg,
                       pm_ra_cosdec = dat['pmra']*u.mas/u.yr,
                       pm_dec = dat['pmdec']*u.mas/u.yr,
                       distance = 12.26167861 *u.kpc)
    gd1 = c.transform_to(gc.GD1Koposov10())
    dat['phi1'] = gd1.phi1.value
    dat['phi2'] = gd1.phi2.value
    dat['pm_phi1'] = gd1.pm_phi1_cosphi2.value
    dat['pm_phi2'] = gd1.pm_phi2.value
    return dat

def select_gd1(dat):
    """Selection by Price-Whelan & Bonaca 2018 on phi2 and their respective proper m
    dat_sel = dat[(dat['phi1']>-100) & (dat['phi1']<20) &
                  (abs(dat['phi2'].value)<1) &
                  (dat['pm_phi1'].value>-9) & (dat['pm_phi1'].value<-4.5) &
                  (dat['pm_phi2'].value>-1.7) & (dat['pm_phi2'].value<1)]
    return dat_sel
```

Plotting and results

In [ ]:

```
def plot_cmd(rrl1, rgb1, bhb1, rrl2, rgb2, bhb2, plot=True):
    """Plotting CMD and making the comparison between metallicity and ratios"""
    if plot==True:
        #Plotting CMD
        fig, ax = plt.subplots(1,2, figsize=(12,6), sharey=True, sharex=True)
        S=8
        ax[0].scatter(rrl1['bprp0'], rrl1['MGmag'], s=S, color=colors[-2], label='RR
        ax[0].errorbar(rgb1['BP_0']-rgb1['RP_0'], rgb1['G_phot'], yerr=rgb1['Gphot_e
                       ecolor=colors[2], fmt='none', marker='none', mew=0, lw=.5, zo
        ax[0].scatter(rgb1['BP_0']-rgb1['RP_0'], rgb1['G_phot'], s=S,
                      c=rgb1['FeHphot_gaia'], vmin=-3, vmax=-0.7, cmap='plasma', lab
        ax[0].scatter(bhb1['bprp0'], bhb1['M'], s=S, color=colors[-1], label='BHB')
        ax[0].set_title('Jhelum', size='xx-large')
        ax[0].legend()

        ax[1].scatter(rrl2['bprp0'], rrl2['MGmag'], s=S, color=colors[-2], label='RR
        ax[1].errorbar(rgb2['BP_0']-rgb2['RP_0'], rgb2['G_phot'], yerr=rgb2['Gphot_e
                       ecolor=colors[2], fmt='none', marker='none', mew=0, lw=.5, zo
        im = ax[1].scatter(rgb2['BP_0']-rgb2['RP_0'], rgb2['G_phot'], s=S,
                      c=rgb2['FeHphot_gaia'], vmin=-3, vmax=-0.7, cmap='plasma', lab
        ax[1].scatter(bhb2['bprp0'], bhb2['M'], s=S, color=colors[-1], label='BHB')
        ax[1].set_title('GD1', size='xx-large')
        ax[1].legend()
        plt.colorbar(im, ax=ax[1], label='Metallicity', pad=0)

        ax[0].set_ylabel('$M_G$', size='x-large')
        for axs in ax.flat:
            axs.set_ylim(1, -2.5)
            axs.set_xlim(-0.25, 1.55)
            axs.set_xlabel('BP-RP', size='x-large')
            axs.tick_params(axis='y', direction='in')
            axs.tick_params(axis='x', direction='in')
        plt.tight_layout(w_pad=0)
        plt.show()
```

```
    #Calculation ratios and errors
    N_rrl_1 = len(rrl1['ra'])
    N_rrl_2 = len(rrl2['ra'])
    N_rgb_1 = len(rgb1['ra'])
    N_rgb_2 = len(rgb2['ra'])
    N_bhb_1 = len(bhb1['ra'])
    N_bhb_2 = len(bhb2['ra'])

    #There are no PS1 RRL in Jhelum, so to keep the code from crashing,
    #we're putting down nans if there are no RRL
    if N_rrl_1 != 0:
        rgb_rrl_1 = N_rgb_1/N_rrl_1
        e_1_rgb_rrl = (rgb_rrl_1*((N_rgb_1+N_rrl_1)/N_rrl_1**2))**0.5
        m_rrl1 = np.mean(rrl1['Fe_H'])
        em_rrl1 = np.std(rrl1['Fe_H'])/N_rrl_1**0.5
        rrl_bhb_1 = N_rrl_1/N_bhb_1
        e_1_rrl_bhb = (rrl_bhb_1*((N_rrl_1+N_bhb_1)/N_bhb_1**2))**0.5
    else:
        rgb_rrl_1 = np.nan
        e_1_rgb_rrl = np.nan
        m_rrl1 = np.nan
        em_rrl1 = np.nan
        rrl_bhb_1 = np.nan
        e_1_rrl_bhb = np.nan


    rgb_bhb_1 = N_rgb_1/N_bhb_1
    e_1_rgb_bhb = (rgb_bhb_1*((N_rgb_1+N_bhb_1)/N_bhb_1**2))**0.5

    rrl_bhb_2 = N_rrl_2/N_bhb_2
    e_2_rrl_bhb = (rrl_bhb_2*((N_rrl_2+N_bhb_2)/N_bhb_2**2))**0.5

    rgb_rrl_2 = N_rgb_2/N_rrl_2
    e_2_rgb_rrl = (rgb_rrl_2*((N_rgb_2+N_rrl_2)/N_rrl_2**2))**0.5

    rgb_bhb_2 = N_rgb_2/N_bhb_2
    e_2_rgb_bhb = (rgb_bhb_2*((N_rgb_2+N_bhb_2)/N_bhb_2**2))**0.5

    #Mean metallicity
    m_rgb1 = np.median(rgb1['FeHphot_gaia'])
    em_rgb1 = np.std(rgb1['FeHphot_gaia'])/N_rgb_1**0.5
    m_rgb2 = np.median(rgb2['FeHphot_gaia'])
    em_rgb2 = np.std(rgb2['FeHphot_gaia'])/N_rgb_2**0.5

    m_rrl2 = np.median(rrl2['Fe_H'])
    em_rrl2 = np.std(rrl2['Fe_H'])/N_rrl_2**0.5

    ratios = [rrl_bhb_1, rgb_rrl_1, rgb_bhb_1, rrl_bhb_2, rgb_rrl_2, rgb_bhb_2]
    err = [e_1_rrl_bhb, e_1_rgb_rrl, e_1_rgb_bhb, e_2_rrl_bhb, e_2_rgb_rrl, e_2_rgb_
    m = [m_rgb1, m_rrl1, m_rgb2, m_rrl2]
    em = [em_rgb1, em_rrl1, em_rgb2, em_rrl2]
    print(N_rrl_1, N_rrl_2,N_rgb_1,N_rgb_2)

    print('         |   rrl/bhb     |     rgb/rrl    |    rgb/bhb   |   rgb [Fe/H]

    print(f'Trailing |  {rrl_bhb_1:.3}+-{e_1_rrl_bhb:.2}   |   {rgb_rrl_1:.3}+-{e_1_
          f'{rgb_bhb_1:.3}+-{e_1_rgb_bhb:.2}  |  {m_rgb1:.2}+-{em_rgb1:.2}   |  {m_r

    print(f'Leading  |  {rrl_bhb_2:.3}+-{e_2_rrl_bhb:.2}   |   {rgb_rrl_2:.3}+-{e_2_
          f'{rgb_bhb_2:.3}+-{e_2_rgb_bhb:.2}  |  {m_rgb2:.2}+-{em_rgb2:.2}   |  {m_r

    return ratios, err, m, em
```

```
def plot_cmd_sag(rrl, rgb, bhb, typ, plot=True):
    #Select trailing arm
    rrl_p1 = rrl[(rrl['Lambda']<-50)]
    rgb_p1 = rgb[(rgb['Lambda']<-50)]
    bhb_p1 = bhb[(bhb['Lambda']<-50)]

    #Select old selection of leading arm (too far out)
    if typ=='old':
        rrl_p2 = rrl[(rrl['Lambda']>49) & (rrl['Beta']>0.35*rrl['Lambda']-43)]
        rgb_p2 = rgb[(rgb['Lambda']>49) & (rgb['Beta']>0.35*rgb['Lambda']-43)]
        bhb_p2 = bhb[(bhb['Lambda']>49) & (bhb['Beta']>0.35*bhb['Lambda']-43)]

    #New selection of Leading arm (dist more comparable)
    else:
        rrl_p2 = rrl[(rrl['Lambda']>103)]
        rgb_p2 = rgb[(rgb['Lambda']>103)]
        bhb_p2 = bhb[(bhb['Lambda']>103)]

    #Sometimes I don't want all the plots, just the return values, so this prevents
    if plot==True:
        plt.hist(rrl_p1['Dist'], color=colors[-2], alpha=0.8, label='Trailing arm',
        plt.hist(rrl_p2['Dist'], color=colors[-1], alpha=0.8, label='Leading arm', d
        plt.xlabel('Distance (kpc)', size='x-large')
        plt.ylabel('Normalized bin count', size='x-large')
        plt.legend()
        plt.show()

        fig, ax = plt.subplots(1,2, figsize=(14,7), sharey=True, sharex=True)
        S=8
        ax[0].scatter(rrl_p1['bprp0'], rrl_p1['MGmag'], s=S, color=colors[-2], label
        ax[0].errorbar(rgb_p1['BP_0']-rgb_p1['RP_0'], rgb_p1['G_phot'], yerr=rgb_p1[
                       ecolor=colors[2], fmt='none', marker='none', mew=0, lw=.5, zo
        ax[0].scatter(rgb_p1['BP_0']-rgb_p1['RP_0'], rgb_p1['G_phot'],
                      s=S, color=colors[2], label='RGB deep-Pristine')
        ax[0].scatter(bhb_p1['bprp0'], bhb_p1['g0']-5*np.log10(bhb_p1['Dist']*1e3)+5
                      s=S, color=colors[-1], label='BHB')
        ax[0].legend()

        ax[1].scatter(rrl_p2['bprp0'], rrl_p2['MGmag'], s=S, color=colors[-2], label
        ax[1].errorbar(rgb_p2['BP_0']-rgb_p2['RP_0'], rgb_p2['G_phot'], yerr=rgb_p2[
                       ecolor=colors[2], fmt='none', marker='none', mew=0, lw=.5, zo
        ax[1].scatter(rgb_p2['BP_0']-rgb_p2['RP_0'], rgb_p2['G_phot'],
                      s=S, color=colors[2], label='RGB deep-Pristine')
        ax[1].scatter(bhb_p2['bprp0'], bhb_p2['g0']-5*np.log10(bhb_p2['Dist']*1e3)+5
                      s=S, color=colors[-1], label='BHB')
        ax[1].legend()

        ax1 = fig.add_axes([0.12, .6, .1, .2])
        ax1.scatter(rrl_sag['Lambda'], rrl_sag['Dist'], marker='.', s=1,
                    alpha=0.3, color='black')
        ax1.scatter(rrl_p1['Lambda'], rrl_p1['Dist'], marker='.', s=1,
                    alpha=0.7, color=colors[0])
        ax1.set_ylabel('D (kpc)', size='large')
        ax1.set_xlabel('$\Lambda_{\odot}$', size='large')
        ax2 = fig.add_axes([0.58, .6, .1, .2])
        ax2.scatter(rrl_sag['Lambda'], rrl_sag['Dist'], marker='.', s=1,
                    alpha=0.3, color='black')
        ax2.scatter(rrl_p2['Lambda'], rrl_p2['Dist'], marker='.', s=1,
                    alpha=0.7, color=colors[0])
        ax2.set_ylabel('D (kpc)', size='large')
        ax2.set_xlabel('$\Lambda_{\odot}$', size='large')

        ax[0].set_ylabel('$M_G$', size='xx-large')
        for axs in ax.flat:
```

```
            axs.set_ylim(1, -2.5)
            axs.set_xlim(-0.25, 1.55)
            axs.set_xlabel('BP-RP', size='xx-large')
            axs.tick_params(axis='y', direction='in', labelsize=14)
            axs.tick_params(axis='x', direction='in', labelsize=14)
        plt.tight_layout(w_pad=0)
        plt.show()

    #Ratio calculation
    N_rrl_1 = len(rrl_p1['ra'])
    N_rrl_2 = len(rrl_p2['ra'])
    N_bhb_1 = len(bhb_p1['ra'])
    N_bhb_2 = len(bhb_p2['ra'])
    N_rgb_1 = len(rgb_p1['ra'])
    N_rgb_2 = len(rgb_p1['ra'])

    rrl_bhb_1 = N_rrl_1/N_bhb_1
    e_1_rrl_bhb = (rrl_bhb_1*((N_rrl_1+N_bhb_1)/N_bhb_1**2))**0.5

    rgb_rrl_1 = N_rgb_1/N_rrl_1
    e_1_rgb_rrl = (rgb_rrl_1*((N_rgb_1+N_rrl_1)/N_rrl_1**2))**0.5

    rgb_bhb_1 = N_rgb_1/N_bhb_1
    e_1_rgb_bhb = (rgb_bhb_1*((N_rgb_1+N_bhb_1)/N_bhb_1**2))**0.5

    rrl_bhb_2 = N_rrl_2/N_bhb_2
    e_2_rrl_bhb = (rrl_bhb_2*((N_rrl_2+N_bhb_2)/N_bhb_2**2))**0.5

    rgb_rrl_2 = N_rgb_2/N_rrl_2
    e_2_rgb_rrl = (rgb_rrl_2*((N_rgb_2+N_rrl_2)/N_rrl_2**2))**0.5

    rgb_bhb_2 = N_rgb_2/N_bhb_2
    e_2_rgb_bhb = (rgb_bhb_2*((N_rgb_2+N_bhb_2)/N_bhb_2**2))**0.5

    #Mean metallicity
    m_rgb1 = np.median(rgb_p1['FeH_Pristine'])
    em_rgb1 = np.std(rgb_p1['FeH_Pristine'])/N_rgb_1**0.5
    m_rgb2 = np.median(rgb_p2['FeH_Pristine'])
    em_rgb2 = np.std(rgb_p2['FeH_Pristine'])/N_rgb_2**0.5
    m_rrl1 = np.median(rrl_p1['Fe_H'])
    em_rrl1 = np.std(rrl_p1['Fe_H'])/N_rrl_1**0.5
    m_rrl2 = np.median(rrl_p2['Fe_H'])
    em_rrl2 = np.std(rrl_p2['Fe_H'])/N_rrl_2**0.5

    #putting the ratios in lists [ratios part 1, ratios part 2]
    ratios = [rrl_bhb_1, rgb_rrl_1, rgb_bhb_1, rrl_bhb_2, rgb_rrl_2, rgb_bhb_2]
    err = [e_1_rrl_bhb, e_1_rgb_rrl, e_1_rgb_bhb, e_2_rrl_bhb, e_2_rgb_rrl, e_2_rgb_
    m = [m_rgb1, m_rrl1, m_rgb2, m_rrl2]
    em = [em_rgb1, em_rrl1, em_rgb2, em_rrl2]
    print(N_rrl_1, N_rrl_2,N_rgb_1,N_rgb_2)

    print('         |   rrl/bhb     |     rgb/rrl    |    rgb/bhb   |   rgb [Fe/H]
    print(f'Trailing |  {rrl_bhb_1:.3}+-{e_1_rrl_bhb:.2}   |   {rgb_rrl_1:.3}+-{e_1_
          f'  {rgb_bhb_1:.3}+-{e_1_rgb_bhb:.2}  |   {m_rgb1:.2}+-{em_rgb1:.2}   |  {

    print(f'Leading  |  {rrl_bhb_2:.3}+-{e_2_rrl_bhb:.2}   |   {rgb_rrl_2:.3}+-{e_2_
          f'{rgb_bhb_2:.3}+-{e_2_rgb_bhb:.2}  |  {m_rgb2:.2}+-{em_rgb2:.2}   |  {m_r

    return ratios, err, m , em



def plot_met(dat1, dat2, sag=False):
    if sag==False:
```

```
        x = 'phi1'
        y = 'phi2'
        z = 'FeHphot_gaia'
        xt = '$\phi_1$'
        yt = '$\phi_2$'
    else:
        x = 'Lambda'
        y = 'Beta'
        z = 'FeH_Pristine'
        xt = '$Λ_{\odot}$'
        yt = '$B_{\odot}$'

    rrl_mean_b, e_rrl_b, B_rrl = run_ave(dat1, quan='Fe_H', quan2=y, sim=False)
    rgb_mean_b, e_rgb_b, B_rgb = run_ave(dat2, quan=z, quan2=y, sim=False)

    rrl_mean_l, e_rrl_l, L_rrl = run_ave(dat1, quan='Fe_H', quan2=x, sim=False)
    rgb_mean_l, e_rgb_l, L_rgb = run_ave(dat2, quan=z, quan2=x, sim=False)

    fig, axs = plt.subplot_mosaic([['lb', 'lb', 'lb', 'b'],
                                   ['lb', 'lb', 'lb', 'b'],
                                   ['l', 'l', 'l', '.']],
                                  figsize=(9,5), layout='constrained')
    if sag==True:
        axs['b'].set_xlim(-1.8, -0.7)
        axs['l'].set_ylim(-1.8, -0.7)

        im = axs['lb'].scatter(dat1[x], dat1[y], s=2, c=dat1['Fe_H'],
                               vmin=-1.8, vmax=-0.5, cmap='plasma')
        axs['lb'].scatter(dat2[x], dat2[y], s=2, c=dat2[z],
                          vmin=-1.8, vmax=-0.5, cmap='plasma')
        axs['lb'].plot([9,18], [-20, 20], ls='--', color='grey')
        axs['lb'].text(-170, -20, 'Trailing arm', size='small')
        axs['lb'].text(110, -20, 'Leading arm', size='small')

    else:
        im = axs['lb'].scatter(dat1[x], dat1[y], s=2, c=dat1['Fe_H'],
                               vmin=-3, vmax=0, cmap='plasma')
        axs['lb'].scatter(dat2[x], dat2[y], s=2, c=dat2[z],
                          vmin=-3, vmax=0, cmap='plasma')
        axs['b'].set_xlim(-3,0)
        axs['l'].set_ylim(-3,0)
    axs['lb'].set_ylabel(f'{yt} (deg)', size='large')

    axs['b'].errorbar(rgb_mean_b[1:-1], B_rgb[1:-1], xerr=e_rgb_b[1:-1], marker='.',
                      linestyle='none', color=colors[2], label='RGB Pristine')
    axs['b'].errorbar(rrl_mean_b[1:-1], B_rrl[1:-1], xerr=e_rrl_b[1:-1], marker='.',
                      linestyle='none', color=colors[-2], label='RRL Gaia')
    axs['b'].yaxis.tick_right()
    axs['b'].set_xlabel('Metallicity [Fe/H]')

    axs['l'].errorbar(L_rgb[1:-1], rgb_mean_l[1:-1], yerr=e_rgb_l[1:-1], marker='.',
                      linestyle='none', color=colors[2], label='RGB Pristine')
    axs['l'].errorbar(L_rrl[1:-1], rrl_mean_l[1:-1], yerr=e_rrl_l[1:-1], marker='.',
                      linestyle='none', color=colors[-2], label='RRL Gaia')
    axs['l'].set_xlabel(f'{xt} (deg)', size='large')
    axs['l'].set_ylabel('Metallicity [Fe/H]', size='large')

    fig.colorbar(im, ax=axs['lb'], label='Metallicity', pad=0)
    fig.set_constrained_layout_pads(w_pad=0, h_pad=0, hspace=0, wspace=0)
    plt.show()

def feature3(data):
    if str(data)==str(rgb_sag):
        above = len(data[(data['Lambda']>50) & (data['Lambda']<140) & (data['Dist']*
```

```
        below = len(data[(data['Lambda']>50) & (data['Lambda']<140) & (data['Dist']*
    else:
        above = len(data[(data['Lambda']>50) & (data['Lambda']<140) & (data['Dist']>
        below = len(data[(data['Lambda']>50) & (data['Lambda']<140) & (data['Dist']<
    ratio = above/below
    e_r = (ratio*((above+below)/below**2))**0.5
    return ratio, e_r
```

Loading in data

In [ ]:

```
#BHB with 80% quality cut
bhb_8 = QTable.read("/net/virgo01/data/users/jstraat/BHB_Pristine_pm.csv")
bhb_8.rename_column('dist_sdss', "Dist")
bhb_8.rename_column('pmRA', 'pmra')
bhb_8.rename_column('pmDE', 'pmdec')
bhb_8.rename_column('e_pmRA', 'pmra_error')
bhb_8.rename_column('e_pmDE', 'pmdec_error')

# ALl-sky BHBs go out to ~20kpc
bhb_c = QTable.read('BHBData/BHB_gaia_20kpc.csv')

#Pan-STARRS1 RRL
rrl_pan = QTable.read('/net/virgo01/data/users/jstraat/Panstarr_RRL_mags.csv')
rrl_pan['MGmag'] = rrl_pan['g0'] - 5*(np.log10(rrl_pan['Dist'])+2)
rrl_pan['Lambda'] = l_sag(rrl_pan['ra'], rrl_pan['dec'])
rrl_pan['Beta'] = b_sag(rrl_pan['ra'], rrl_pan['dec'])
rrl_pan.rename_column('[Fe/H]','Fe_H')

#Pan-STARRS1 RRL w/ Pristine footprint
rrl_pan_fp = QTable.read('/net/virgo01/data/users/jstraat/Panstarrs_pristine_fp.csv'
rrl_pan_fp['MGmag'] = rrl_pan_fp['g0'] - 5*(np.log10(rrl_pan_fp['Dist'])+2)
rrl_pan_fp['Lambda'] = l_sag(rrl_pan_fp['ra'], rrl_pan_fp['dec'])
rrl_pan_fp['Beta'] = b_sag(rrl_pan_fp['ra'], rrl_pan_fp['dec'])
rrl_pan_fp.rename_column('[Fe/H]','Fe_H')

#Gaia RRL Li sample
Gaia_rrl = QTable.read('/net/virgo01/data/users/jstraat/Li_rrl_w_periods.csv')
Gaia_rrl['Lambda'] = l_sag(Gaia_rrl['ra'], Gaia_rrl['dec'])
Gaia_rrl['Beta'] = b_sag(Gaia_rrl['ra'], Gaia_rrl['dec'])

#Gaia RRL with pristine footprint
rrl_prist = QTable.read('/net/virgo01/data/users/jstraat/Gaia_prist_w_pm.csv')
rrl_prist['Lambda'] = l_sag(rrl_prist['ra'], rrl_prist['dec'])
rrl_prist['Beta'] = b_sag(rrl_prist['ra'], rrl_prist['dec'])

#RGB deep Pristine
Ak_s = vaex.open('/net/gaia2/data/users/viswanathan/giants-paper1/rgb_pristine_vApr24
Ak_sam= Ak_s[(Ak_s['logg_xgboost']<2.3)]
Ak_sam.rename_column('phot_dist', 'Dist')
Ak_sam.rename_column('parallax', 'Plx')
Ak_sam['Lambda'] = l_sag(Ak_sam['ra'], Ak_sam['dec'])
Ak_sam['Beta'] = b_sag(Ak_sam['ra'], Ak_sam['dec'])
Ak_sam['Gphot_err'] = d_M(Ak_sam)
#RGB Gaia Pristine
Ak_sam_g = vaex.open('/net/gaia2/data/users/viswanathan/giants-paper1/rgb_pristinega
Ak_sam_gaia = Ak_sam_g[(Ak_sam_g['logg_xgboost']<2.3)]
Ak_sam_gaia.rename_column('pmRA', 'pmra')
Ak_sam_gaia.rename_column('pmDE', 'pmdec')
Ak_sam_gaia.rename_column('e_pmRA', 'pmra_error')
Ak_sam_gaia.rename_column('e_pmDE', 'pmdec_error')
Ak_sam_gaia.rename_column('phot_dist', 'Dist')
Ak_sam_gaia.rename_column('dec_1', 'dec')
```

```
Ak_sam_gaia['Gphot_err'] = d_M(Ak_sam_gaia)


#Simulations of Sag
sag_simt= np.loadtxt('/net/virgo01/data/users/jstraat/Sag_sim/stars.txt', comments='
sag_sim = QTable({'Lambda':sag_simt[:,12], 'Beta':sag_simt[:,13],
                  'pmra':sag_simt[:,9], 'pmdec':sag_simt[:,10],
                  'Dist':sag_simt[:,8], 'Tstrip':sag_simt[:,15]})
```

In [ ]:

```
#Fitting proper motion tracks from Vasili simulations(tango for three)
stdlpmra, meanpmra, stdupmra, x1 = run_ave(sag_sim, 'pmra')
stdlpmdec, meanpmdec, stdupmdec, x2 = run_ave(sag_sim, 'pmdec')

#defining functions for tracks
pmra_track = interp1d(x1, meanpmra)
pmdec_track = interp1d(x2, meanpmdec)
stdu_pmra = interp1d(x1, stdupmra)
stdu_pmdec = interp1d(x2, stdupmdec)
stdl_pmra = interp1d(x1, stdlpmra)
stdl_pmdec = interp1d(x2, stdlpmdec)
```

In [ ]:

```
rrl_jhel = select_jhel(jhel_coords(Gaia_rrl))
pan_jhel = select_jhel(jhel_coords(rrl_pan))
rgb_jhe = select_jhel(jhel_coords(Ak_sam_gaia))
rgb_jhel = rgb_jhe[rgb_jhe['FeHphot_gaia']<-0.75]
bhb_jhel = select_jhel(jhel_coords(bhb_c))


rrl_gd1 = select_gd1(gd1_coords(Gaia_rrl))
pan_gd1 = select_gd1(gd1_coords(rrl_pan))
rgb_gd = select_gd1(gd1_coords(Ak_sam_gaia))
rgb_gd1 = rgb_gd[rgb_gd['FeHphot_gaia']<-0.7]
bhb_gd1 = select_gd1(gd1_coords(bhb_c))

rrl_sag = select_sag(Gaia_rrl)
rrl_sag_fp = select_sag(rrl_prist)

pan_sag = select_sag(rrl_pan)
pan_sag_fp = select_sag(rrl_pan_fp)

rgb_sag = select_sag(Ak_sam)
bhb_sag = select_sag(bhb_8)
```

Jhelum and GD-1

In [ ]:

```
fig, ax = plt.subplots(2,3, figsize=(13,6), sharey=True, sharex=True)

ax[1,1].set_xlabel('RA (deg)', size='large')
ax[1,0].set_xlabel('RA (deg)', size='large')
ax[0,0].set_ylabel('Dec (deg) Jhelum', size='large')
ax[1,0].set_ylabel('Dec (deg) GD1', size='large')
# ax[2,0].set_ylabel('Dec (deg) Jhelum', size='large')
for axs in ax.flat:
#     axs.set_ylim(20, 65)
#     axs.set_xlim(230,140)
    axs.tick_params(axis='y', direction='in')
    axs.tick_params(axis='x', direction='in')
```

```
ax[0,0].scatter(Gaia_rrl['ra'], Gaia_rrl['dec'], s=1, alpha=0.3, color='grey')
ax[0,0].scatter(rrl_jhel['ra'], rrl_jhel['dec'], color=colors[-2])
ax[0,0].set_title('RR Lyrae')
ax[0,1].scatter(Ak_sam_gaia['ra'], Ak_sam_gaia['dec'], s=1, alpha=0.01, color='grey'
ax[0,1].scatter(rgb_jhel['ra'], rgb_jhel['dec'], color=colors[2], s=2)

ax[0,1].set_title('RGB stars')
ax[1,0].scatter(Gaia_rrl['ra'], Gaia_rrl['dec'], s=1, alpha=0.3, color='grey')
ax[1,0].scatter(rrl_gd1['ra'], rrl_gd1['dec'], color=colors[-2])
ax[1,1].scatter(Ak_sam_gaia['ra'], Ak_sam_gaia['dec'], s=1, alpha=0.01, color='grey'
ax[1,1].scatter(rgb_gd1['ra'], rgb_gd1['dec'], color=colors[2], s=2)

ax[0,2].set_title('BHB stars')
ax[0,2].scatter(bhb_c['ra'], bhb_c['dec'], s=1, alpha=0.3, color='grey')
ax[0,2].scatter(bhb_jhel['ra'], bhb_jhel['dec'], color=colors[-1])
ax[1,2].scatter(bhb_c['ra'], bhb_c['dec'], s=1, alpha=0.3, color='grey')
ax[1,2].scatter(bhb_gd1['ra'], bhb_gd1['dec'], color=colors[-1])

fig.tight_layout(h_pad=0, w_pad=0)
plt.show()
```

In [ ]:

```
r_stream, err_stream, m_stream, em_stream = plot_cmd(rrl_jhel, rgb_jhel, bhb_jhel,
                                                     rrl_gd1, rgb_gd1, bhb_gd1)
r_stream_p, err_stream_p, m_stream_p, em_stream_p = plot_cmd(pan_jhel, rgb_jhel, bhb
                                                             pan_gd1, rgb_gd1, bhb_g
                                                             plot=False)
```

In [ ]:

```
G_j = new_G(rrl_jhel, rgb_jhel)
G_g = new_G(rrl_gd1, rgb_gd1)
fig, ax = plt.subplots(1,2, figsize=(12,6), sharey=True, sharex=True)
S=8
ax[0].scatter(rrl_jhel['bprp0'], rrl_jhel['MGmag'], s=S,
              color=colors[-2], label='RRL')
ax[0].scatter(rgb_jhel['BP_0']-rgb_jhel['RP_0'], G_j, c=rgb_jhel['FeHphot_gaia'],
              s=S, vmin=-3, vmax=-0.7, cmap='plasma', label='RGB')
ax[0].scatter(bhb_jhel['bprp0'], bhb_jhel['M'], s=S, color=colors[-1], label='BHB')
ax[0].set_title('Jhelum', size='xx-large')
ax[0].legend()



ax[1].scatter(rrl_gd1['bprp0'], rrl_gd1['MGmag'], s=S, color=colors[-2], label='RRL'
im = ax[1].scatter(rgb_gd1['BP_0']-rgb_gd1['RP_0'], G_g, s=S,
                      c=rgb_gd1['FeHphot_gaia'], vmin=-3, vmax=-0.7, cmap='plasma',
ax[1].scatter(bhb_gd1['bprp0'], bhb_gd1['M'], s=S, color=colors[-1], label='BHB')
ax[1].set_title('GD1', size='xx-large')
ax[1].legend()
plt.colorbar(im, ax=ax[1], label='Metallicity', pad=0)

ax[0].set_ylabel('$M_G$', size='x-large')
for axs in ax.flat:
    axs.set_ylim(1, -2.5)
    axs.set_xlim(-0.25, 1.55)
    axs.set_xlabel('BP-RP', size='x-large')
    axs.tick_params(axis='y', direction='in')
    axs.tick_params(axis='x', direction='in')
plt.tight_layout(w_pad=0)
plt.show()
```

In [ ]:

```
plot_met(rrl_gd1, rgb_gd1)
```

Sagittarius

In [ ]:

```
r_sag, err_sag, m_sag, em_sag = plot_cmd_sag(rrl_sag_fp, rgb_sag, bhb_sag, 'new')
```

In [ ]:

```
r_sag_o, err_sag_o, m_sag_o, em_sag_o = plot_cmd_sag(rrl_sag_fp, rgb_sag, bhb_sag, '
```

In [ ]:

```
r_sag_p, err_sag_p, m_sag_p, em_sag_p = plot_cmd_sag(pan_sag_fp, rgb_sag, bhb_sag, '
```

Feature 3

In [ ]:

```
r_rrl, er_rrl = feature3(rrl_sag)
r_pan, er_pan = feature3(pan_sag)
r_bhb, er_bhb = feature3(bhb_sag)
r_rgb, er_rgb = feature3(rgb_sag)
r_sim, er_sim = feature3(sag_sim)
ratios = [r_bhb, r_rrl, r_pan, r_rgb, r_sim]
e_ratios = [er_bhb, er_rrl, er_pan, er_rgb, er_sim]
r_mean = np.mean(ratios[:4])
e_r = (np.sum([i**2 for i in e_ratios[:4]]))**0.5

x = np.linspace(0,5,5)
my_xticks = ['BHB','RRL', 'RRL PS1','RGB','Sim']

fig, ax = plt.subplots(1, figsize=(15, 6))
ax.fill_between(np.linspace(-0.5, 5.5), r_mean+e_r, r_mean-e_r, alpha=0.3, color=col
ax.axhline(r_mean, color=colors[-2], label=f'Mean ratio={r_mean:.3}')
ax.errorbar(x, ratios, yerr=e_ratios, marker='o', linestyle='none', color=colors[-1]
ax.set_xticks(x, my_xticks)
ax.tick_params(labelsize=15)
ax.set_xlim(-0.2, 5.2)
ax.legend(fontsize='xx-large')
ax.set_ylabel('$N_{F3}/N_{stream}$', size='xx-large')
plt.show()


print('      |      RRL     |      BHB      |      RGB      |      Sim')
print(f'Ratio | {r_rrl:.3}+-{er_rrl:.2} | {r_bhb:.3}+-{er_bhb:.2} | ',
      f'{r_rgb:.3}+-{er_rgb:.2} | {r_sim:.2}+-{er_sim:.1}')
print(f'{r_pan:.3}, {er_pan:.3}')
print(e_r)
```

Overall comparison

In [ ]:

```
fig, ax = plt.subplots(1,3, figsize=(18,6))

metal = np.array([-1.77, -2.24, m_sag[0], m_sag[2]])
e_metal = np.array([0.13, 0.21, em_sag[0], em_sag[2]])
metal_p = np.array([-1.77, -2.24, m_sag_p[0], m_sag_p[2]])
e_metal_p = np.array([0.13
, 0.21, em_sag_p[0], em_sag_p[2]])
```

```
titles = ['RRL/BHB', 'RGB/RRL', 'RGB/BHB']
print('              |    All   |  Gaia RRL  | PS1 RRL  ')

for j in range(3):
    ratios = np.array([r_stream[j], r_stream[j+3], r_sag[j],
                       r_sag[j+3]])
    e_ratios = np.array([err_stream[j], err_stream[j+3], err_sag[j],
                         err_sag[j+3]])
    ratios_p = np.array([r_stream_p[j], r_stream_p[j+3], r_sag_p[j],
                         r_sag_p[j+3]])
    e_ratios_p = np.array([err_stream_p[j], err_stream_p[j+3],
                           err_sag_p[j], err_sag_p[j+3]])

    all_r = np.concatenate((ratios, ratios_p[1:]))
    all_m = np.concatenate((metal, metal_p[1:]))
    all_er = np.concatenate((e_ratios, e_ratios_p[1:]))
    all_em = np.concatenate((e_metal, e_metal_p[1:]))
    sr_p, p_p = spearmanr(metal_p[1:], ratios_p[1:])
    r_p, std_p = bootstrap_spearman_with_errors(metal_p[1:], ratios_p[1:], e_metal_p

    if j==2:
        all_r = np.concatenate((ratios,ratios_p[1:]))
        all_m = np.concatenate((metal,metal_p[1:]))
        sr_p, p_p = spearmanr(metal_p, ratios_p)
        r_p, std_p = bootstrap_spearman_with_errors(metal_p, ratios_p, e_metal_p, e_

    sr_all, p_all = spearmanr(all_m, all_r)
    sr_g, p_g = spearmanr(metal, ratios)
    r_all, std_all = bootstrap_spearman_with_errors(all_m, all_r, all_em, all_er)
    r_g, std_g = bootstrap_spearman_with_errors(metal, ratios, e_metal, e_ratios)


    print(f'{titles[j]} w/ er |   {r_all:.3}     {r_g:.3}       {r_p:.3}')
    labels = ['Jhelum', 'GD-1', 'Sag T', 'Sag L']
    labels_p = ['Jhelum PS1', 'GD-1 PS1', 'Sag T PS1', 'Sag L PS1']
    for i in range(4):
        ax[j].fill_between([metal[i]-e_metal[i], metal[i]+e_metal[i]],
                           ratios[i]-e_ratios[i], ratios[i]+e_ratios[i],
                           color=colors[i+1], alpha=0.2)
        ax[j].scatter(metal[i], ratios[i], color=colors[i+1], label=labels[i],
                      marker='o')
        ax[j].errorbar(metal[i], ratios[i], xerr=e_metal[i], yerr=e_ratios[i],
                       color=colors[i+1])

        ax[j].fill_between([metal_p[i]-e_metal_p[i], metal_p[i]+e_metal_p[i]],
                           ratios_p[i]-e_ratios_p[i], ratios_p[i]+e_ratios_p[i],
                        color=colors[i+1], alpha=0.2, hatch='/')
        ax[j].scatter(metal_p[i], ratios_p[i], color=colors[i+1], label=labels_p[i],
                      marker='o', fc='none')
        eb1 = ax[j].errorbar(metal_p[i], ratios_p[i], xerr=e_metal_p[i], yerr=e_rati
                             color=colors[i+1], linestyle=':')
        eb1[-1][0].set_linestyle(':')
        eb1[-1][1].set_linestyle(':')
    ax[j].set_title(titles[j], size='xx-large')
ax[0].set_ylabel('Ratio', size='x-large')
for axs in ax.flat:
    axs.set_xlabel('Metallicity (RGB)', size='x-large')
    axs.tick_params(axis='y', direction='in')
    axs.tick_params(axis='x', direction='in')
plt.tight_layout(w_pad=0)
ax[0].legend(loc='upper left')
plt.show()
```

In [ ]:

```
L_rrl = r_sag[1+3]/r_sag_p[1+3]
T_rrl = r_sag[1]/r_sag_p[1]

f3_r = (1+r_rrl)/(1+r_pan)
print(f'Leading: {L_rrl:.5}, Trailing: {T_rrl:.5}, Feature 3 ratio: {f3_r:.5}')
print(r_sag)
print(r_sag_p)
```

Period RRL

only have periods for RRab, selected variable is pf=period for fundamental oscillators so makes sense

In [ ]:

```
rrl_p1 = rrl_sag[(rrl_sag['Lambda']<-50)]
rrl_p2 = rrl_sag[(rrl_sag['Lambda']>103)]

plt.hist(rrl_p1['pf'], color=colors[-2], alpha=0.8, label='Trailing arm', density=Tr
plt.hist(rrl_p2['pf'], color=colors[-1], alpha=0.8, label='Leading arm', density=Tru
plt.xlabel('Period (days)', size='x-large')
plt.ylabel('Normalized bin count', size='x-large')
plt.legend()
plt.show()
```

Check if there is a relation between metalicity and period

There seems to be slight correlation between the two, but that is logical as the Li 2022 metallicities are based on the period of RRLs

In [ ]:

```
z, xedge, yedge = np.histogram2d(rrl_sag['bprp0'], rrl_sag['pf'], bins=[150,150])

fig, ax = plt.subplots(1,1, figsize=(9,6))

pcm = ax.pcolormesh(xedge, yedge, z.T, norm='log', cmap='plasma', vmax=20)
ax.set_xlabel('[Fe/H]')
ax.set_ylabel('Period (days)')
ax.set_xlim(-0.2, 1)
fig.colorbar(pcm, ax=ax, label='#points', pad=0)
plt.show()
```

In [ ]:

```
per_r, per_p = pearsonr(rrl_sag['Fe_H'], rrl_sag['pf'])
per_r
```

Check what caused the apparent magnitude peaks

In [ ]:

```
dat = rrl_pan
dat1 = dat[(dat['Gmag']<19.6) & (dat['Gmag']>19)]

fig, ax = plt.subplots(1,2, figsize=(12,6), subplot_kw={'projection': 'polar'})
ax[0].fill_between
ax[0].scatter(np.radians(dat['Lambda']), dat['Gmag'], alpha=0.1, s=1, color=colors[0
# ax[0].scatter(np.radians(dat1['Lambda']), dat1['Gmag'], alpha=0.1, s=1, color=colo
```

```
ax[0].set_rmin(12)
ax[1].scatter(np.radians(dat['Lambda']), dat['Dist'], alpha=0.1, s=1, color=colors[0
ax[1].scatter(np.radians(dat1['Lambda']), dat1['Dist'], alpha=0.1, s=1, color=colors
# ax.set_rmax(80)
plt.grid(True)
plt.show()
```

Making footprint plots of the surveys used

In [ ]:

```
c_rgb = coord.SkyCoord(ra=Ak_sam['ra']*u.degree, dec=Ak_sam['dec']*u.degree, frame='
c_rrl = coord.SkyCoord(ra=Gaia_rrl['ra']*u.degree, dec=Gaia_rrl['dec']*u.degree, fra
c_pan = coord.SkyCoord(ra=rrl_pan['ra']*u.degree, dec=rrl_pan['dec']*u.degree, frame
rgb_gal = c_rgb.galactic
rrl_gal = c_rrl.galactic
pan_gal = c_pan.galactic

fig = plt.figure(1,figsize=(22,12))
ax0 = fig.add_subplot(221, projection='aitoff')
ax1 = fig.add_subplot(222, projection='aitoff')
ax2 = fig.add_subplot(223, projection='aitoff')

ax0.scatter(-rrl_gal.l.wrap_at('180d').radian, rrl_gal.b.radian, s=2, alpha=0.5, col
ax0.set_title('Gaia', size='xx-large')
ax1.scatter(-pan_gal.l.wrap_at('180d').radian, pan_gal.b.radian, s=2, color=colors[-
ax1.set_title('PS1', size='xx-large')
ax2.scatter(-rgb_gal.l.wrap_at('180d').radian, rgb_gal.b.radian, s=2, color=colors[-
ax2.set_title('Pristine', size='xx-large')
plt.tight_layout(w_pad=0, h_pad=0)
plt.show()
```

In [ ]:

```
fig, ax = plt.subplots(figsize=(12,6))
rgb_m, e_1, dist_rgb = run_ave(Ak_sam, 'FeH_Pristine', quan2='Dist', sim=False)
rrl_m, e_2, dist_rrl = run_ave(Gaia_rrl, 'Fe_H', quan2='Dist', sim=False)
ax.scatter(Ak_sam['Dist'], Ak_sam['FeH_Pristine'], s=1, color=colors[2], alpha=0.4)
ax.scatter(Gaia_rrl['Dist'], Gaia_rrl['Fe_H'], s=1, color=colors[-2], alpha=0.4)
ax.errorbar(dist_rgb, rgb_m, yerr=e_1, color=colors[2], label='RGB')
ax.errorbar(dist_rrl, rrl_m, yerr=e_2, color=colors[-1], label='RRL')
ax.set_ylim(-2.5,-0.4)
ax.set_xlim(0,100)
ax.legend()
ax.set_xlabel('Distance (kpc)')
plt.ylabel('[Fe/H]')
plt.show()
```

In [ ]: